공학석사 학위논문

Anisotropy of elastic moduli, P-wave velocities, and thermal conductivities of transversely isotropic rock and its borehole stability

횡등방성 암석의 탄성계수, P파 속도, 열전도도 이방성과 공벽 안정성 해석

2012년 8월

서울대학교 대학원

에너지시스템공학부

김 한 나

Anisotropy of elastic moduli, P-wave velocities, and thermal conductivities of transversely isotropic rock and its borehole stability

지도 교수 민 기 복

이 논문을 공학석사 학위논문으로 제출함
2012년 8월

서울대학교 대학원
에너지시스템공학부
김 한 나

김한나의 석사 학위논문을 인준함
2012년 8월

위 원 장 전 석 원 (인)

부위원장 민 기 복 (인)

위 원 송 재 준 (인)

학위논문 원문제공 서비스에 대한 동의서

본인의 학위논문에 대하여 서울대학교가 아래와 같이 학위논문 제공하는 것에 동의합니다.

1. 동의사항

① 본인의 논문을 보존이나 인터넷 등을 통한 온라인 서비스 목적으로 복제할 경우 저작물의 내용을 변경하지 않는 범위 내에서의 복제를 허용합니다.

② 본인의 논문을 디지털화하여 인터넷 등 정보통신망을 통한 논문의 일부 또는 전부의 복제.배포 및 전송 시 무료로 제공하는 것에 동의합니다.

2. 개인(저작자)의 의무

본 논문의 저작권을 타인에게 양도하거나 또는 출판을 허락하는 등 동의 내용을 변경하고자 할 때는 소속대학(원)에 공개의 유보 또는 해지를 즉시 통보하겠습니다.

3. 서울대학교의 의무

① 서울대학교는 본 논문을 외부에 제공할 경우 저작권 보호장치(DRM)를 사용하여야 합니다.

② 서울대학교는 본 논문에 대한 공개의 유보나 해지 신청 시 즉시 처리해야 합니다.

논문제목 : (Place thesis title here)

학위구분 : **석사 □ · 박사 □**
학 과 : (Department)
학 번 : (Student number)
연 락 처 : (Contact info)
저 작 자 : (Name) 인)

제 출 일 : 200 년 월 일

서울대학교총장 귀하

Agreement of Thesis Disclosure

(Do not include this English form in the thesis copy. Use the Korean form in the previous page.)

I approve the thesis distribution service offered by Seoul National University under the following agreement.

1. Agreement

① I approve the duplication of the thesis for the purpose of archiving or online service via internet as long as the contents of the thesis are not modified.

② I approve free duplication, distribution, and transmission of the entire (or partial) thesis in digital format via internet or similar network.

2. Author Responsibility

When the copyright of the thesis is transferred to others or is allowed to be published for any reason that may invalidate this agreement, I will immediately notify the College to defer or stop distributing the copyrighted contents.

3. University Responsibility

① The University must protect the copyright of the thesis under digital rights management (DRM) when providing the thesis to outside individuals or parties.

② The University must process the request for the deferment or suspension of the thesis distribution immediately.

Thesis Title : (Place Thesis Title Here)

Degree : Master's ☐ Ph.D. ☐
Department:
Student number:
Contact info:
Author name: (Stamp)

Submission date : YYYY 년 MM 월 DD 일

Attn: President of Seoul National University

Abstract

Anisotropy of elastic moduli, P-wave velocities, and thermal conductivities of transversely isotropic rock and its borehole stability

Hanna Kim

Department of Energy Systems Engineering

The Graduate School

Seoul National University

It is required to analyze the state of stresses and displacements around the borehole in important subsurface engineering applications. Rock anisotropy not only causes changes in stress concentration around a borehole but also affects the direction of borehole breakout and fracture initiation. The stress and displacement analysis that do not consider the anisotropic behavior of rock can be erroneous in varying degrees and therefore, it is necessary to consider the anisotropy in borehole stability analysis.

The experimental investigation of the anisotropy of elastic moduli, P-wave velocities, and thermal conductivities for Asan gneiss, Boryeong shale, and Yeoncheon schist in Korea were conducted. Cylindrical core samples with different anisotropy angles were prepared by coring at 15-degree intervals from the transversely isotropic plane using the laboratory directional coring system established for this study. Elastic moduli, P-wave velocities, and thermal conductivities were determined along the sample axis for different

anisotropy angles. The anisotropy ratio is defined as the ratio of the properties parallel to the transversely isotropic plane to those perpendicular to the plane, and the anisotropy ratios for the thermal conductivities (K(90°)/K(0°)) of Asan gneiss, Boryeong shale, and Yeoncheon schist were 1.4, 2.1, and 2.5, respectively. The P-wave velocity anisotropy ratios ($V_P(90°)/V_P(0°)$) for Asan gneiss, Boryeong shale, and Yeoncheon schist were 1.2, 1.5, and 2.3, respectively. The mean prediction errors (MPEs), defined as the average relative differences between measured and predicted values of the seismic velocity, for Asan gneiss, Boryeong shale, and Yeoncheon schist were 3.5%, 4.6%, and 8.9%, respectively. The MPEs of thermal conductivity for Asan gneiss, Boryeong shale, and Yeoncheon schist were 6.1%, 9.3%, and 8.6%, respectively. The application of tensorial transformation evaluations revealed that the three types of rocks chosen for this study can be modeled effectively by a transversely isotropic model.

In order to analyze the borehole stability in transversely isotropic rock both analytical and numerical methods were conducted based on the mechanical experimental results. The finite element method was applied in numerical analysis. The study includes the verification of existing analytical solution, comparison of the results of elastic analysis from numerical model, comparison of the isotropic and anisotropic model, and the range of borehole breakout that is predicted using the anisotropic Mohr-Coulomb failure criterion considering strength anisotropy.

Keywords: anisotropy, transversely isotropic, thermal conductivity, P-wave velocity, borehole breakout, borehole stability, strength anisotropy

Student Number: 2010-23337

Contents

Chapter 1. Introduction 1

1.1. Rock anisotropy and borehole stability 1

1.2. The scope of the study 4

Chapter 2. Theory for anisotropic rock 6

2.1. Elastic constants of transversely isotropic rock 6

2.2. Seismic velocity of transversely isotropic rock 11

2.3. Thermal conductivity of transversely isotropic rock 13

Chapter 3. Laboratory experiments for mechanical, seismic, and thermal anisotropic properties 15

3.1. Sample preparation 15

3.2. Elastic constants 19

3.3. P-wave velocity 20

3.4. Thermal conductivity 21

Chapter 4. Experimental results 23

4.1. Elastic constants 23

4.2. P-wave velocity 26

4.3. Thermal conductivity 28

4.4. Comparison of measured properties and properties predicted theoretically by tensorial transformation 34

4.5. Comparison of anisotropy ratio for mechanical, seismic, and thermal properties 37

Chapter 5. Borehole stability in isotropic rock.....42

5.1. Stress distribution around a borehole – analytic study 42

5.2. Stress distribution around a borehole – numerical study 49

5.3. Borehole breakout.....54

Chapter 6. Borehole stability in transversely isotropic rock……...63

6.1. Stress distribution around a borehole – analytic study 63

6.2. Stress distribution around a borehole – numerical study 88

6.3. Stress distribution around inclined borehole.....98

6.4. Borehole breakout.....102

Chapter 7. Summary and conclusions.....128

List of Tables

Table 4.1. The five elastic constants of Asan gneiss, Boryeong shale, and Yoencheon schist (Cho et al., 2012) 23
Table 4.2 Rock forming minerals for rock type 32
Table 5.1 Parameters used to examine the variation of σθθ, σzz and σrr at the borehole wall in isotropic rock 46
Table 5.2 Parameters used to analyze the stress concentration in isotropic rock 50
Table 6.1 Parameters used to analyze the stress distribution in transversely anisotropic rock 89
Table 6.2 Parameters used to predict borehole breakout 119

List of Figures

Figure 2.1 A transversely isotropic body for which the x, y plane is the plane of isotropy. 9
Figure 3.1 Microphotographs of sample (Pl: plagioclase, Qz: quartz, Bt: biotite, Hb: hornblende, Mu: muscovite, Or: orthoclase, Grt: garnet) 16
Figure 3.2 Directional coring system and sample preparation (Cho et al., 2012) 18
Figure 3.3 Seismic velocity measurement system 21
Figure 3.4 Diagram of the divided-bar method for measuring thermal conductivity (modified from (Beardsmore and Cull, 2001)) 22
Figure 4.1 Variation of apparent Young's modulus (E_θ) and theoretical results from the transversely isotropic solution (Gn: Gneiss; Sh: Shale; Sc: Schist) (Cho et al., 2012) 25
Figure 4.2 Variation of P-wave velocity (V_P) and theoretical predictions (Gn: Gneiss; Sh: Shale; Sc: Schist) 28
Figure 4.3 Variation of thermal conductivity and theoretical prediction (Gn: Gneiss; Sh: Shale; Sc: Schist 30
Figure 4.4 Quartz content with anisotropy angle obtained from XRD 33
Figure 4.5 Mean prediction error of elastic moduli, P-wave velocities, and thermal conductivities 35
Figure 4.6 Correlation between (a) elastic moduli and P-wave velocities, (b) elastic moduli and thermal conductivities, and (c) thermal conductivities and P-wave velocities 39
Figure 5.1 The state of stress around a circular hole in an infinite elastic rock mass with far field stress S_{Hmax} acting in the x direction and far field stress S_{hmin} acting in the y direction 42
Figure 5.2 Variation of tangential stress, $\sigma_{\theta\theta}$ around a vertical well of radius R subject S_{Hmax} acting in an east–west. $\sigma_{\theta\theta}$ varies strongly with both position around the wellbore and distance from the wellbore wall. (Data from (Chang et al., 2010)) 45
Figure 5.3 Stress ratio contour map in southeast of Korea: (a) K_{min} (= S_{hmin} / S_v) (b) K_{max} (= S_{Hmax} / S_v) (Chang et al., 2010) 47
Figure 5.4 Variation of stresses, $\sigma_{\theta\theta}$, σ_{rr} and σ_{zz} at the wall of borehole in isotropic rock 48

Figure 5.5 3D numerical finite element model..... 49
Figure 5.6 Isotropic model and boundary condition 50
Figure 5.7 Variation of tangential and radial stress in isotropic rock (unit: Pa) 52
Figure 5.8 Stress distribution of analytic and numerical results in isotropic rock 53
Figure 5.9 Schematic cross-section of a borehole showing a compressive failure zone known as breakout (Haimson and Chang, 2002) 54
Figure 5.10 (a) Area in which failure is expected for c=12.5MPa (Zoback et al., 1985). (b) The zone of failure around the borehole for the assumed rock strength is indicated by the contour line. 56
Figure 5.11 Theoretical size of the areas in which the compressive shear strength of the rock is exceeded by the concentrated stresses. For the values of the effective compressive principal stress and coefficient of friction shown, the contours in each figure define the size of the initial failure zone for a given value of C and $\Delta P=0$ (Zoback et al., 1985). 58
Figure 5.12 The results of numerical analysis with data used in Figure 5.11 60
Figure 5.13 The effect of excess well bore fluid pressure ΔP on the size of well bore breakouts. Contours define the size of the initial failure zone for C = 10MPa when S_{Hmax} = 22.0M Pa, S_{hmin}= 11.0 MPa, and $\mu = 0.6$. (a) $\Delta P = 0$, (b) $\Delta P = 2.5$, (c) $\Delta P = -2.5$ (Zoback et al., 1985) 61
Figure 6.1 Borehole coordinate system – global coordinate system 64
Figure 6.2 Material coordinate system for transversely isotropic medium with tilted symmetry axis (modified from Gaede et al. (2012))..... 68
Figure 6.3 Diagram of stress concentration for uniaxial stress condition 75
Figure 6.4 stress concentration for uniaxial condition with respect to the degree of anisotropy..... 76
Figure 6.5 Stress concentration around the borehole with respect to degree of anisotropy..... 77
Figure 6.6 Distribution of tangential stress around the borehole in uniform biaxial stress condition..... 78
Figure 6.7 Tangential stress for nonuniform biaxial stress condition around the borehole wall..... 79
Figure 6.8 Normalized tangential stress by internal pressure..... 81
Figure 6.9 Stress distribution around borehole with respect to the Poisson's

ratio (ν/ν') changes 83
Figure 6.10 Stress distribution around borehole with respect to the shear modulus ratio (G/G') 86
Figure 6.11 The boundary condition for vertical borehole and horizontal borehole in transversely isotropic rock 90
Figure 6.12 the variations of the tangential stress ($\sigma_{\theta\theta}$) and radial stress (σ_{rr}) around the vertical and horizontal hole (unit: Pa) 91
Figure 6.13 Stress distribution around the borehole in transversely isotropic rock 93
Figure 6.14 Stress distribution along the x-direction in vertical and horizontal borehole 94
Figure 6.15 Stress distribution along the y-direction in vertical and horizontal borehole 95
Figure 6.16 Stress distribution along the domain with respect to degree of anisotropy 97
Figure 6.17 Boundary condition for inclined borehole in transversely isotropic rock 98
Figure 6.18 Stress distribution around the borehole wall with the change of the inclination, α_D 99
Figure 6.19 Variation of tangential stress around inclined borehole 101
Figure 6.20 Local coordinate system (modified from (Lee and Choi, 2011) 105
Figure 6.21 Spatial variation of cohesion in a transversely isotropic rock (modified from (Lee and Choi, 2011)) 106
Figure 6.22 Geometry of the sample for the simulation of triaxial compression test 107
Figure 6.23 Simulation results of triaxial test for Green River Shale[33] with different inclinations of weak plane (c_0=45MPa, Ω_0^c= 0.12, ϕ_0=20°, Ω_0^ϕ=0.1) 109
Figure 6.24 Normal and shear stresses acting on a plane in local coordinate system 111
Figure 6.25 Boundary condition for borehole breakout in isotropic rock 113
Figure 6.26 Borehole breakout in isotropic rock 114
Figure 6.27 Borehole breakout in isotropic rock using suggested anisotropic criterion 116
Figure 6.28 Boundary conditions for failure analysis in transversely isotropic rock 118

Figure 6.29 Borehole breakout analysis result according to the stress regime 123
Figure 6.30 Mohr-coulomb failure criterion in (a) transversely isotropic rock and (b) isotropic rock 125
Figure 6.31 Shape of borehole breakout 126
Figure 6.32 Anisotropic failure criterion and the increase of maximum principal stress (σ_1) 127

Chapter 1. Introduction

1.1. Rock anisotropy and borehole stability

Many engineering applications of geo-environmental importance, such as CO_2 geo-sequestration, enhanced geothermal systems (EGSs), and geological repositories of radioactive waste, require comprehensive analysis of thermal, hydraulic, mechanical, and chemical processes. Accordingly, the numbers of properties that must be characterized are numerous, and extensive investigations are required to determine the properties of each process. One issue that has to be considered is anisotropy of rock properties. Many rocks have anisotropic characteristics, and their mechanical, thermal, seismic, and hydraulic properties often vary with direction. Anisotropy plays an important role in various rock engineering activities. In civil and mining engineering, rock anisotropy controls the stability of underground excavations and foundations. Rock anisotropy also affects drilling, blasting and rock cutting. In petroleum engineering, rock anisotropy is a critical factor in controlling borehole deviation, stability, deformation and failure. It also impacts fracturing and fracture propagation (Chen et al., 1996). Engineering applications that do not consider the anisotropic behavior of

rock can produce errors of differing magnitudes, depending on the extent of anisotropy of the rock. Therefore, rock anisotropy has long been an issue of serious concern in rock engineering (Amadei, 1996a; Barla, 1974; Pinto, 1969).

While there are numerous studies focusing on the anisotropy of individual mechanical (Chen et al., 1998), seismic (Blackman et al., 2002; Johnston and Christensen, 1995; Owens and Bamford, 1976), and thermal properties (Brigaud and Vasseur, 1989), only a few studies have considered the anisotropy relationship of more than two processes for the same rock (Johnson and Wenk, 1974).

It is required to analyze the stress and displacement state around the borehole in some of important subsurface geotechnical engineering applications such as borehole and underground excavation. For example, the presence of a borehole in a stressed subsurface rock formation alters the local principal stress directions and magnitudes around the borehole. For isotropic elastic homogeneous rocks, borehole stresses are given by the classical elastic solution by Kirsch. This solution is widely used for engineering and research applications.

During drilling process, many boreholes encounter anisotropic formations such as shale. Shale has mechanically anisotropic characteristics.

Rock anisotropy not only causes changes stress concentration around borehole but also affects fracture initiation. The stress and displacement analysis that do not consider the anisotropic behavior of rock can produce errors. Therefore, it is necessary to consider the anisotropic characteristic in analysis.

Many authors have studied the stress distribution in an anisotropic medium. Lekhnitskii (1963) provided a comprehensive solution for the stresses in an anisotropic elastic medium. He suggested the solutions to generalized plane strain and plane problems for a body with rectilinear anisotropy, and related problems for a homogeneous and continuously non-homogeneous body having cylindrical anisotropy, among others. Amadei (1982) followed Lekhnitski's approach and applied them to a wide range of rock mechanics problems. He developed the analytic solution for elastic equilibrium of an anisotropic homogeneous body bounded internally by a cylindrical surface of arbitrary cross-section and the particular solution for an infinite cylinder with a circular cross section. These solutions were obtained by extending Lekhnistski's approach to include the influence of a boundary stress component parallel to the axis.

Aadnoy (1989) applied Amadei's solutions to calculate the stress distribution of horizontal borehole subjected to a non-hydrostatic stress field in a transversely isotropic medium and. Ong (1994) extended Aadnoy's

model to include nonlinear and poroelastic effects.

The final solution of stress distribution around an infinite cylinder with circular cross-section was simplified by Ong to the stress distribution at the borehole wall. This solution will be used in this study to analyze the effect of rock anisotropy in borehole.

1.2. The scope of the study

This study is composed of two parts. The first part is on laboratory determination of mechanical, seismic and thermal properties of three rock types in Korea and the second one is the effect of anisotropy on borehole stability.

The aim of the first part is to determine the anisotropic effects on elastic deformability, seismic velocity, and thermal conductivity properties for transversely isotropic rock in Korea. Applicability of the transversely isotropic model was investigated by comparing the tensorial transformation laws to the directional properties of each rock. The correlations between anisotropic mechanical, seismic, and thermal properties were also examined.

The aim of the second part is to analyze the borehole stability in transversely isotropic rock based on mechanical results of the first part.

Both analytical and numerical methods were conducted in order to analyze the borehole stability in transversely isotropic rock. The finite element method was applied in the numerical analysis. The study includes the verification of existing analytical solution, comparison of the results of elastic analysis from numerical model, comparison of the isotropic and anisotropic model, and the determination of the range of borehole breakout that is expected.

Finally, the importance of considering anisotropy in borehole stability analysis is demonstrated in a wide variety of scenarios with varying degree of anisotropy in transversely isotropic model.

Chapter 2. Theory for anisotropic rock

2.1. Elastic constants of transversely isotropic rock

The constitutive relation in both isotropic and anisotropic rock formation can be found in many textbooks. And it is noted that the major portion of description in this section is from Brady and Brown (2004). A variety of idealized constitutive models have been formulated for various engineering materials, which describe both the time-independent and time-dependent responses of the material to applied load. These models describe responses in terms of elasticity, plasticity, viscosity and creep, and combinations of those modes. For any constitutive model, stress, strain, or some derived quantities, such as stress and strain rates, are related through a set of constitutive equations. Elasticity represents the most common constitutive behavior of engineering materials, including many rocks, and it forms a useful basis for the description of more complex behavior. In formulating constitutive equations, it is useful to construct column vectors from the elements of the stress and strain matrices, i.e. stress and strain vectors are defined by

$$[\sigma]=\begin{bmatrix}\sigma_{xx}\\ \sigma_{yy}\\ \sigma_{zz}\\ \tau_{yz}\\ \tau_{zx}\\ \tau_{xy}\end{bmatrix} \text{ and } \qquad [\varepsilon]=\begin{bmatrix}\varepsilon_{xx}\\ \varepsilon_{yy}\\ \varepsilon_{zz}\\ \gamma_{yz}\\ \gamma_{zx}\\ \gamma_{xy}\end{bmatrix} \tag{2.1}$$

The most general statement of linear elastic constitutive behavior is a generalized form of Hooke's Law, in which any strain component is a linear function of all the stress components,

$$[\varepsilon]=[S][\sigma] \tag{2.2}$$

Or

$$\begin{bmatrix}\varepsilon_{xx}\\ \varepsilon_{yy}\\ \varepsilon_{zz}\\ \gamma_{yz}\\ \gamma_{zx}\\ \gamma_{xy}\end{bmatrix}=\begin{bmatrix}S_{11} & S_{12} & S_{13} & S_{14} & S_{15} & S_{16}\\ S_{21} & S_{22} & S_{23} & S_{24} & S_{25} & S_{26}\\ S_{31} & S_{32} & S_{33} & S_{34} & S_{35} & S_{36}\\ S_{41} & S_{42} & S_{43} & S_{44} & S_{45} & S_{46}\\ S_{51} & S_{52} & S_{53} & S_{54} & S_{55} & S_{56}\\ S_{61} & S_{62} & S_{63} & S_{64} & S_{65} & S_{66}\end{bmatrix}\begin{bmatrix}\sigma_{xx}\\ \sigma_{yy}\\ \sigma_{yy}\\ \tau_{yz}\\ \tau_{zx}\\ \tau_{xy}\end{bmatrix} \tag{2.3}$$

The matrix [S] is a compliance tensor and each element is called a compliance or elastic modulus. Although in compliance tensor there are 36 independent compliances, a reciprocal theorem may be used to demonstrate that the compliance matrix is symmetric. The matrix therefore contains only 21 independent constants. In some cases it is more convenient to apply

equation (2.3) in inverse form, i.e.

$$[\sigma] = [D][\varepsilon] \tag{2.4}$$

The matrix [D] is called the elasticity matrix or the matrix of elastic stiffnesses. For general anisotropic elasticity, there are 21 independent stiffnesses. Equation (2.3) indicates complete coupling between all stress and strain components. The existence of axes of elastic symmetry in a body de-couples some of the stress–strain relations, and reduces the number of independent constants required to define the material elasticity. In the case of isotropic elasticity, any arbitrarily oriented axis in the medium is an axis of elastic symmetry. Equation (2.3) for isotropic elastic materials reduces to the following form.

$$\begin{bmatrix} \varepsilon_{xx} \\ \varepsilon_{yy} \\ \varepsilon_{zz} \\ \gamma_{yz} \\ \gamma_{zx} \\ \gamma_{xy} \end{bmatrix} = \frac{1}{E} \begin{bmatrix} 1 & -\nu & -\nu & 0 & 0 & 0 \\ -\nu & 1 & -\nu & 0 & 0 & 0 \\ -\nu & -\nu & 1 & 0 & 0 & 0 \\ 0 & 0 & 0 & 2(1+\nu) & 0 & 0 \\ 0 & 0 & 0 & 0 & 2(1+\nu) & 0 \\ 0 & 0 & 0 & 0 & 0 & 2(1+\nu) \end{bmatrix} \begin{bmatrix} \sigma_{xx} \\ \sigma_{yy} \\ \sigma_{yy} \\ \tau_{yz} \\ \tau_{zx} \\ \tau_{xy} \end{bmatrix} \tag{2.5}$$

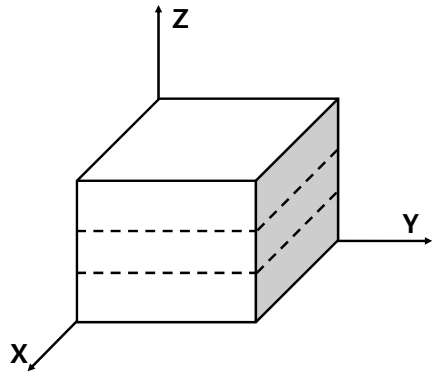

Figure 2.1 A transversely isotropic body for which the x, y plane is the plane of isotropy.

A transversely isotropic material has one axis of elastic symmetry of rotation. If this axis is denoted as z, the other two principal axes, x and y, are parallel to the transversely isotropic plane. In this coordinate system, Hooke's law can be expressed in the form of a compliance matrix, as shown in Eq. (2.6) (Lekhnitskii, 1963):

$$\begin{bmatrix} \varepsilon_x \\ \varepsilon_y \\ \varepsilon_z \\ \gamma_{yz} \\ \gamma_{zx} \\ \gamma_{xy} \end{bmatrix} = \begin{bmatrix} \frac{1}{E} & -\frac{\nu}{E} & -\frac{\nu'}{E'} & 0 & 0 & 0 \\ -\frac{\nu}{E} & \frac{1}{E} & -\frac{\nu'}{E'} & 0 & 0 & 0 \\ -\frac{\nu'}{E'} & -\frac{\nu'}{E'} & \frac{1}{E'} & 0 & 0 & 0 \\ 0 & 0 & 0 & \frac{1}{G'} & 0 & 0 \\ 0 & 0 & 0 & 0 & \frac{1}{G'} & 0 \\ 0 & 0 & 0 & 0 & 0 & \frac{1}{G} \end{bmatrix} \begin{bmatrix} \sigma_x \\ \sigma_y \\ \sigma_z \\ \tau_{yz} \\ \tau_{zx} \\ \tau_{xy} \end{bmatrix} \tag{2.6}$$

where E and E′ are the elastic moduli in the plane of transverse isotropy and in a direction normal to it, respectively. The terms ν and ν′ are Poisson's ratios that characterize the lateral strain response in the plane of transverse isotropy to a stress acting parallel and normal to it, respectively. G and G′ are the shear moduli in the plane parallel and normal to the plane of transverse isotropy, respectively. These relationships can be converted to inverse form, in terms of the stiffness matrix.

$$\begin{bmatrix}\sigma_x\\ \sigma_y\\ \sigma_z\\ \tau_{yz}\\ \tau_{zx}\\ \tau_{xy}\end{bmatrix}=\begin{bmatrix}C_{11} & C_{12} & C_{13} & 0 & 0 & 0\\ C_{12} & C_{11} & C_{13} & 0 & 0 & 0\\ C_{13} & C_{13} & C_{33} & 0 & 0 & 0\\ 0 & 0 & 0 & C_{44} & 0 & 0\\ 0 & 0 & 0 & 0 & C_{44} & 0\\ 0 & 0 & 0 & 0 & 0 & (C_{11}-C_{12})/2\end{bmatrix}\begin{bmatrix}\varepsilon_x\\ \varepsilon_y\\ \varepsilon_z\\ \gamma_{yz}\\ \gamma_{zx}\\ \gamma_{xy}\end{bmatrix} \tag{2.7}$$

where:

$$\begin{aligned}
C_{11} &= E\left(E'-E\nu'^2\right)\Gamma\\
C_{33} &= E'^2\left(1-\nu^2\right)\Gamma\\
C_{12} &= E\left(E'\nu+E\nu'^2\right)\Gamma\\
C_{13} &= EE'\nu'\left(1+\nu\right)\Gamma\\
C_{44} &= G'\\
C_{66} &= G\\
\Gamma &= \frac{1}{\left(1+\nu\right)\left\{\left(1-\nu\right)E'-2\nu'^2E\right\}}
\end{aligned} \tag{2.8}$$

Using these relationships, the stiffness constants from the five elastic moduli of transversely isotropic rock, i.e., E, E′, ν, ν′, G′ can be calculated.

2.2. Seismic velocity of transversely isotropic rock

In general, three types of velocities are measured in anisotropic media: the compressional wave velocity (V_P), the velocity of the shear wave vibrating parallel to bedding (V_{SH}), and the velocity of the shear wave

vibrating in a plane perpendicular to bedding (V_{SV}). When the direction of propagation is perpendicular to the isotropic plane, the velocities of two types of shear waves are same, $V_{SH}(0°) = V_{SV}(0°)$. But except for this case, there are differences between V_{SH} and V_{SV} because of shear wave splitting.

Daley and Hron (1977) expressed the phase velocity as a function of phase angle and stiffness constants in transversely isotropic rocks (Daley and Hron, 1977; Song et al., 2004):

$$\begin{aligned}
\rho V_P^2(\theta) &= \frac{1}{2}\left[C_{33} + C_{44} + (C_{11} - C_{33})\sin^2\theta + D(\theta)\right] \\
\rho V_{SV}^2(\theta) &= \frac{1}{2}\left[C_{33} + C_{44} + (C_{11} - C_{33})\sin^2\theta - D(\theta)\right] \\
\rho V_{SH}^2(\theta) &= \frac{1}{2}(C_{11} - C_{12})\sin^2\theta + C_{44}\cos^2\theta \\
D(\theta) &= \sqrt{\begin{aligned}&(C_{33} - C_{44})^2 + 2\left[2(C_{13} + C_{44})^2 - (C_{33} - C_{44})(C_{11} + C_{33} - 2C_{44})\right]\sin^2\theta \\ &+ \left[(C_{11} + C_{33} - 2C_{44})^2 - 4(C_{13} + C_{44})^2\right]\sin^4\theta\end{aligned}}
\end{aligned} \tag{2.9}$$

where ρ is the density of rock, and the angle θ is the phase angle between the wave vector normal to the wavefront and the symmetry axis along z direction. The angle θ is the same as the anisotropy angle used in this study. The anisotropy angle θ is an angle between an axis of symmetry plane and a direction that measurement is conducted. Using Eq. (2.9), the seismic velocities can be calculated with different directions.

If we use 0°, 45°, and 90° for θ, we can obtain the five stiffness constants as Eq. (2.10) (Lo et al., 1986).

$$
\begin{aligned}
C_{11} &= \rho V_P^{\,2}(90°) \\
C_{12} &= C_{11} - 2\rho V_{SH}^{\,2}(90°) \\
C_{33} &= \rho V_P^{\,2}(0°) \\
C_{44} &= \rho V_{SH}^{\,2}(0°) = \rho V_{SV}^{\,2}(0°) = \rho V_{SV}^{\,2}(90°) \\
C_{13} &= -C_{44} + \sqrt{\begin{aligned}&4\rho^2 V_P^{\,4}(45°) - \left[2\rho V_P^{\,2}(45°) \times (C_{11} + C_{33} + 2C_{44})\right] \\ &+ \left[(C_{11} + C_{44})(C_{33} + C_{44})\right]\end{aligned}}
\end{aligned}
\tag{2.10}
$$

2.3. Thermal conductivity of transversely isotropic rock

Thermal conductivity obeys the rotational transformation rules as a second-order tensor (Jaeger et al., 2007). The tensor of the anisotropic thermal conductivity is formulated as Eq. (2.11) with respect to the rotation of the axes (Carslaw and Jaeger, 1959).

$$
k_{pq}' = \beta_{pi}\beta_{qj}k_{ij} \tag{2.11}
$$

where k_{ij} and k_{pq} are the thermal conductivity tensors in the original and rotated axes, respectively, and β_{pi} and β_{qj} are the direction cosines. If we know two different conductivities that are normal and parallel to the isotropic plane, the thermal conductivity can be obtained by Eq. (2.12).

$$K_{(\theta)} = K_{(0^\circ)} \cos^2 \theta + K_{(90^\circ)} \sin^2 \theta \tag{2.12}$$

where $K_{(0^\circ)}$ and $K_{(90^\circ)}$ are the thermal conductivities normal and parallel to isotropic plane, respectively.

Chapter 3. Laboratory experiments for mechanical, seismic, and thermal anisotropic properties

3.1. Sample preparation

The experiments were conducted on three rock types, i.e., Asan gneiss, Boryeong shale, and Yeoncheon schist. Each rock might show heterogeneity in a microscopic view (i.e. in the mineral scale view point). But, in a macroscopic view, these also showed a clear evidence of transverse isotropy due to the arrangements of some mineral particles as observed in the Fig. 3.1. Asan gneiss is biotite gneiss consisting of plagioclase, hornblende, quartz, and biotite. Flat minerals are arrayed parallel to the foliation plane. Boryeong shale shows flakes of clay minerals and mica that are aligned parallel to the bedding. Yeoncheon schist has schistosity, in which the platy minerals, such as feldspar and mica, are aligned with the schistose plane (Figure 3.1) .

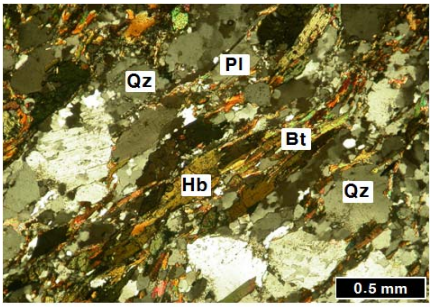

(a) Asan gneiss

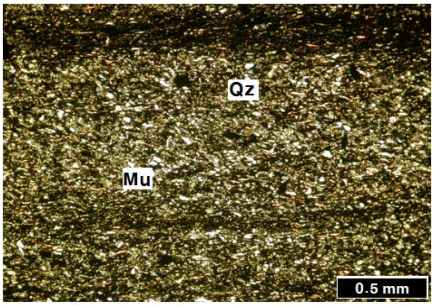

(b) Boryeong shale

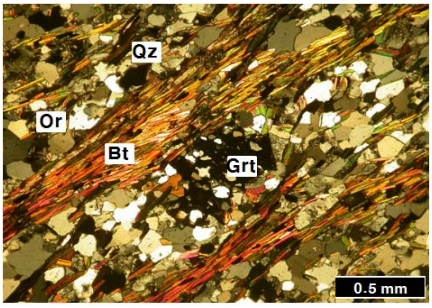

(c) Yeoncheon schist

Figure 3.1 Microphotographs of sample (Pl: plagioclase, Qz: quartz, Bt: biotite, Hb: hornblende, Mu: muscovite, Or: orthoclase, Grt: garnet)

Coring a block with angles of 0, 15, 30, 45, 60, 75, and 90 degrees with respect to the transverse isotropic plane by using our laboratory-scale directional coring system (Figure 3), we obtained two or three sets of cylindrical samples for each type of rock. The mechanical experiments were conducted first on three sets of core samples cored in different directions, and two additional sets of samples were cored to measure the seismic and thermal properties. It is noted that the samples used for testing the mechanical properties were not identical to those used for testing the seismic and thermal properties even though the samples were cored from the same rock block. The ends of the samples obtained to measure seismic properties were cut in order to measure thermal conductivity. To investigate the transversely isotropic characteristics in the macro-scale, we used the samples with enough length (70 mm in length and 38 mm in diameter) in the mechanical and seismic experiments. In order to guarantee the representativeness of the thermal conductivity samples (25.4 mm in length and 7 mm in diameter) which was smaller than the ones for mechanical and seismic experiments, two sets of samples were used in thermal conductivity test and also representativeness of the samples was examined by conducting XRD analysis (Figure 3.2).

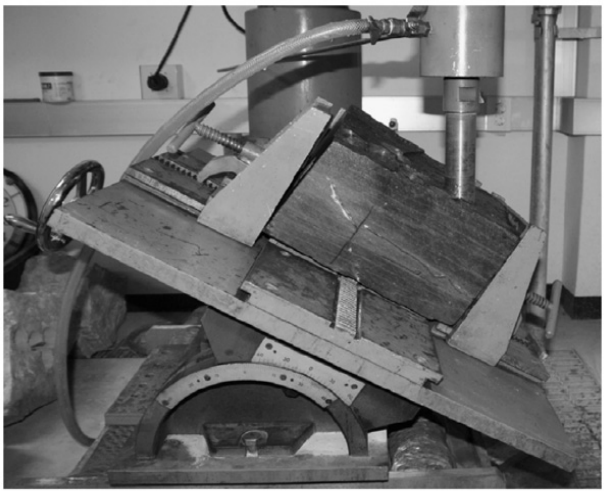

(a) Directional coring system

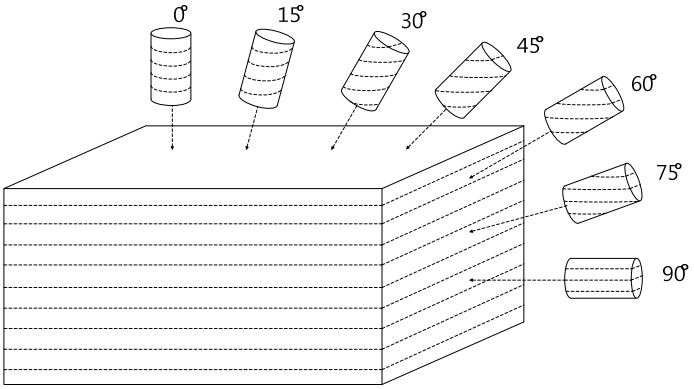

(b) Sample preparation

Figure 3.2 Directional coring system and sample preparation (Cho et al., 2012)

3.2. Elastic constants

For each type of rock, the uniaxial compression test and the Brazilian test were conducted according to ISRM suggested methods (ISRM, 2007). Apparent elastic constants, uniaxial compressive strength, and tensile strength were determined on three sets of each rock type with different foliation angles.

A method to determine the five elastic constants for transversely isotropic rocks were presented in the literature (Amadei, 1996). In this method, three or more specimens (i.e., either cylindrical or prismatic) are generally used in uniaxial compression tests with $\theta = 0°$, $90°$, and an inclined angle θ different from 0 or $90°$, in order to determine the five independent constants. While five independent measurements of strain are sufficient to obtain the five elastic constants, there are more than five strain measurements. In this case, the least square method was used to obtain the best-fit elastic constants. The detailed methodology and results of mechanical anisotropy in terms of both deformation and strength are presented in Cho et al.(2012). Some of the results are presented in this study in order to compare seismic and thermal properties and analyze the borehole stability.

3.3. P-wave velocity

A seismic velocity measurement system was used to measure the seismic velocities (Lee et al., 2010)(Figure 3.3). An acrylic sample was used for calibration. The measurements of seismic velocity of each rock were conducted under confining pressure 0.64 MPa. The measurement precision of the test system was within 0.7% at room temperature and atmospheric pressure.

When entering an anisotropic medium, a shear wave can split into two orthogonally-polarized components, V_{SH} and V_{SV}, which travel along exactly the same propagation path (Daley and Hron, 1977; Song et al., 2004).

In this experiment, as matched transducers polarized along the appropriate directions were not used, the distinction between the V_{SH} and V_{SV} was not made. Therefore, only V_P was considered for this study. But, when the shear wave propagates along the symmetry axis, the vertical and horizontal components of shear wave become same because of Eq. (2.10). To obtain the stiffness constant C_{44}, we measured the shear wave velocity of the sample in which the anisotropy angle was zero.

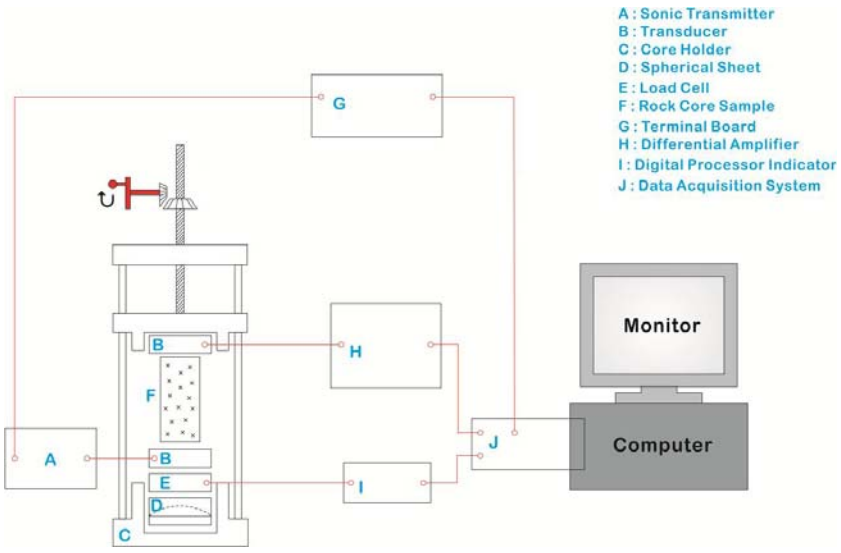

Figure 3.3 Seismic velocity measurement system

3.4. Thermal conductivity

Among several methods available for determining thermal conductivity, the divided-bar method (Figure 3.4) was chosen for this study (Beardsmore and Cull, 2001). This method was recommended for fabric samples that have obvious anisotropy (Pribnow and Sass, 1995). In this study, two sets of each core sample were prepared for the measurements, and each rock sample was cut into discs that were 2.54 cm in diameter and about 7 mm thick. Five discs of fused silica glass and Pyroceram were used to find the contact resistant for calibration. The top and bottom of the device were maintained at

constant temperatures of around 40 °C and 20 °C, respectively. Then, thermal conductivity was measured under a small retaining pressure of 0.5 MPa, which was sufficient to ensure good thermal contact. The relative errors of the measurements were within 5% at room temperature and atmospheric pressure.

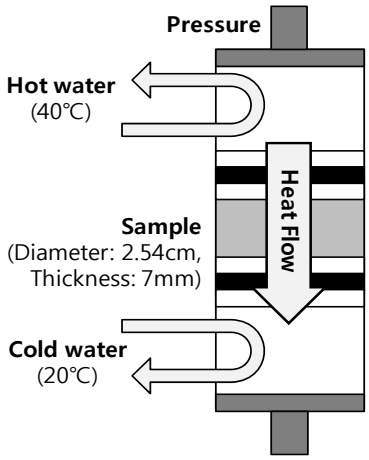

Figure 3.4 Diagram of the divided-bar method for measuring thermal conductivity (modified from (Beardsmore and Cull, 2001))

Chapter 4. Experimental results

4.1. Elastic constants

Some results of Cho et al. (2012) are introduced for completeness of this study. The five elastic constants are listed in Table 4.1. These results were calculated from strain gage readings collected from specimens with different angles of the isotropic plane using the least square method

Table 4.1. The five elastic constants of Asan gneiss, Boryeong shale, and Yoencheon schist (Cho et al., 2012)

Rock type	Set	E (GPa)	E' (GPa)	v	v'	G'(GPa)
Asan gneiss	1	69.9	52.6	0.23	0.26	16.8
	2	62.3	55.1	0.27	0.21	17.0
	3	72.6	55.4	0.26	0.19	17.5
	Mean	68.3	54.4	0.30	0.20	17.1
Boryeong shale	1	45.8	16.5	0.13	0.23	12.0
	2	38.1	20.1	0.23	0.14	6.2
	3	34.0	20.5	0.17	0.22	8.1
	Mean	39.3	19.0	0.18	0.20	8.7
Yeoncheon schist	1	68.4	19.2	0.19	0.13	12.1
	2	74.2	20.6	0.18	0.19	17.5
	3	73.7	23.9	0.37	0.17	11.5
	Mean	72.1	21.2	0.25	0.16	13.7

The apparent Young's moduli measured form the experiment are presented in Figure 4.1 with prediction based on tensorial transformation of the compliance matrix for the transversely isotropic model. The anisotropy ratios of the elastic moduli parallel and perpendicular to the isotropic planes (E/E') were determined to be 1.3, 2.1, and 3.4 for Asan gneiss, Boryeong shale, and Yeoncheon schist, respectively. In general, the measured values from experiments matched reasonably well with the one predicted by the theory. It implies that the transversely isotropic model is a reasonable constitutive model for these specific rock types.

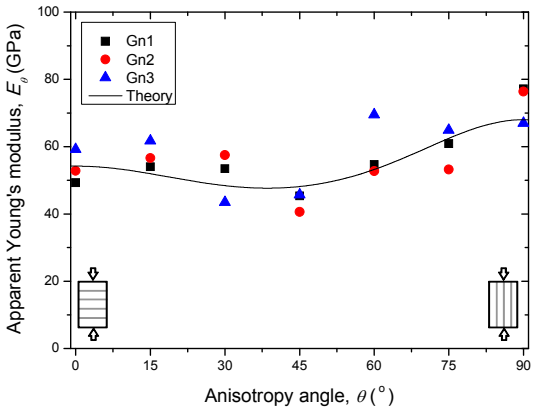

(a) Asan gneiss

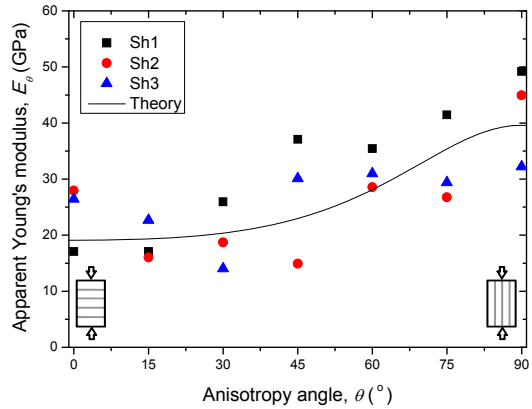

(b) Boryeong shale

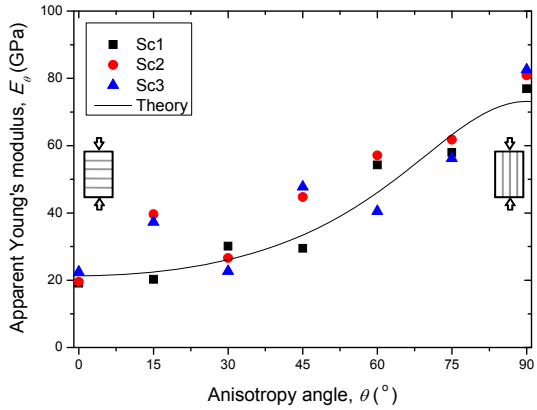

(c) Yeoncheon schist

Figure 4.1 Variation of apparent Young's modulus (E_θ) and theoretical results from the transversely isotropic solution (Gn: Gneiss; Sh: Shale; Sc: Schist) (Cho et al., 2012)

4.2. P-wave velocity

P-wave velocities measured from the seismic experiments are presented in Figure 4.2. In the case of Asan gneiss, the measured P-wave velocities varied from 4360 to 5100 m/s, and the ratio of maximum to minimum P-wave velocities ($V_{P(90°)}/V_{P(0°)}$) was 1.2. P-wave velocities for Boryeong shale varied from 3520 m/s to 5140 m/s, and the anisotropy ratio of P-wave velocity, $V_{P(90°)}/V_{P(0°)}$ was 1.5. Yeoncheon schist showed the most anisotropic behavior in its seismic property. The P-wave velocities varied from 2570 m/s to 5850 m/s, and $V_{P(90°)}/V_{P(0°)}$ was 2.3.

There are misleading and confusion in terms of velocity anisotropy because each researchers use the different definitions for velocity anisotropy. For accurate comparison of P-wave velocity anisotropy, coefficient in terms of velocity anisotropy was used. Velocity anisotropy is the percentage measure of the maximum variation in velocities usually specified as $\left(V_{P\max} - V_{P\min}\right)/V_{P\max} \times 100$, where $V_{P\max}$ and $V_{P\min}$ are the maximum and minimum P-wave velocities, respectively (Crampin, 1989). From this definition, the velocity anisotropy coefficients were 14%, 31% and 51% for Asan gneiss, Boryeong shale and Yeoncheon schist. These values were similar with results of previous researches, which showed P-wave velocity anisotropy of the range of 20% to 25% for gneiss (Birch, 1960), 20% to 35%

for shale (Johnston and Christensen, 1995) and 8% to 70% for Yeoncheon schist(Johnson and Wenk, 1974).

Also shown in Figure 4.2 is the prediction of P-wave velocity using Eq. (2.9) based on the stiffness constants of Eq. (2.10)

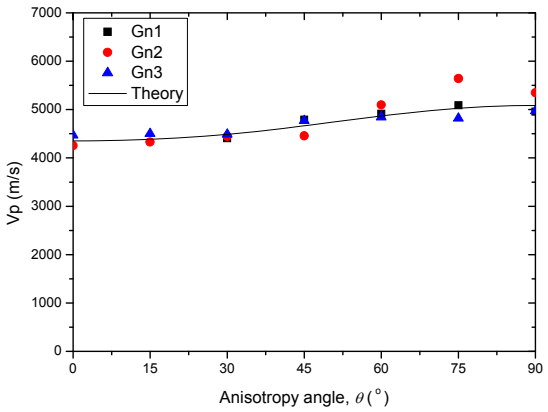

(a) Asan gneiss

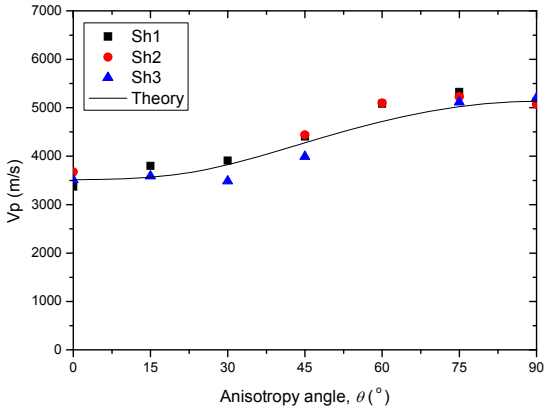

(b) Boryeong shale

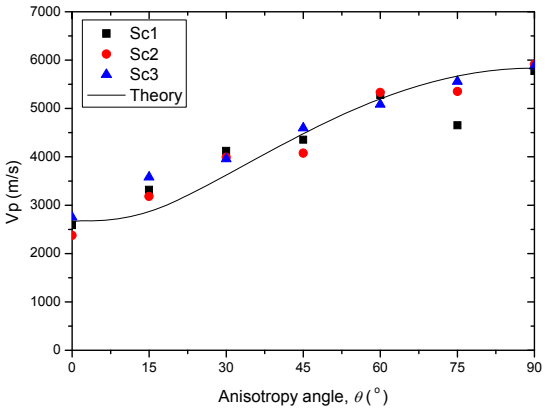

(c) Yeoncheon schist

Figure 4.2 Variation of P-wave velocity (V_P) and theoretical predictions (Gn: Gneiss; Sh: Shale; Sc: Schist)

4.3. Thermal conductivity

The results of the thermal conductivity tests are presented in Figure 4.3. The thermal conductivities of Asan gneiss varied from 1.67 to 2.88 W/mK, and the ratio of maximum to minimum thermal conductivity, $K_{(90°)}/K_{(0°)}$ was 1.4. The thermal conductivity for Boryeong shale varied from 1.51 to 3.5 W/mK, and the anisotropy ratio $K_{(90°)}/K_{(0°)}$ was 2.1. Similar to the result of the elastic constant and P-wave velocity, the most anisotropic behavior was observed in Yeoncheon schist. The thermal conductivities of Yeoncheon schist varied from 1.33 to 4.0 W/mK, and $K_{(90°)}/K_{(0°)}$ was 2.5. The anisotropy

ratios of each rock type ($K_{(90°)}/K_{(0°)}$) were comparable with the results of previous research, which showed anisotropy ratios of 1.44 for gneiss (Birch and Clark, 1940) and 2.12 for shale (Davis et al., 2007).

Figure 4.3 shows the prediction of thermal conductivity based on a second-order tensor transformation by using Eq. (2.11). Even though there are some deviations between the measured values and predicted values due to heterogeneity, the measured values are matched well with predicted ones.

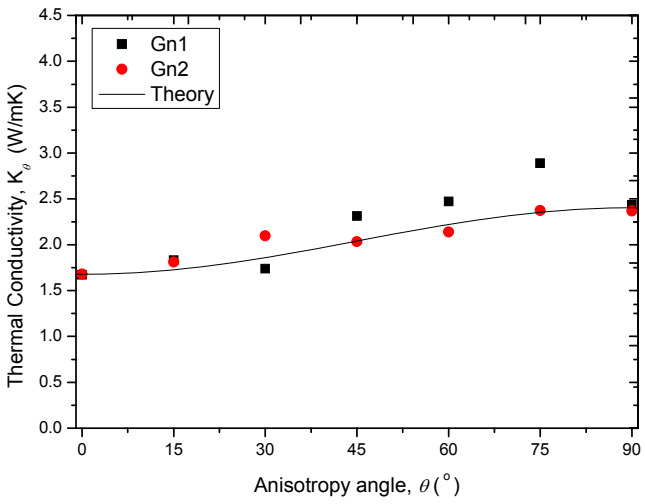

(a) Asan gneiss

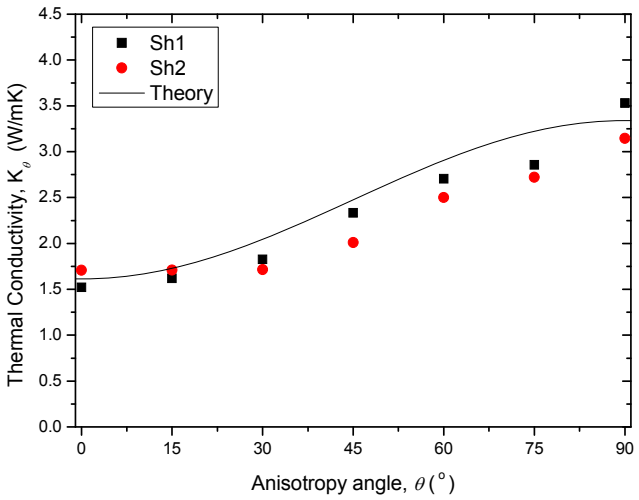

(b) Boryeong shale

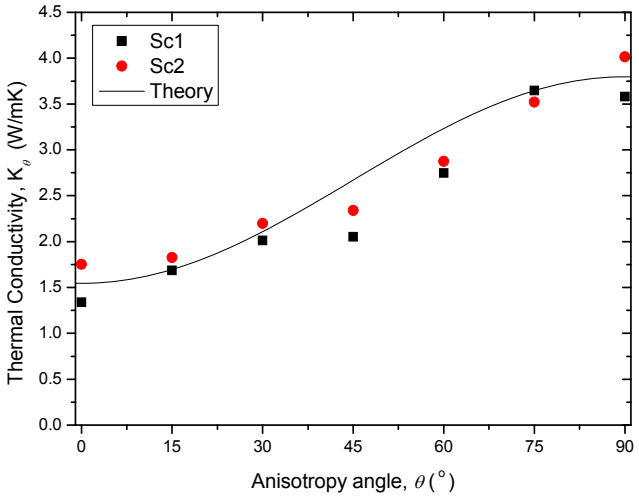

(c) Yoencheon schist

Figure 4.3 Variation of thermal conductivity and theoretical prediction (Gn: Gneiss; Sh: Shale; Sc: Schist

The thermal conductivities obtained from gneiss and schist were more dispersed than that of shale, which implied that these types of rocks are more heterogeneous than shale. Since the thicknesses of the samples were 7 mm, which was rather small, we examined the representativeness of the samples used in the study by conducting X-Ray Diffraction (XRD) analysis to measure the rock-forming minerals for each sample. Each thermal conductivity sample was grinded and the powder form was prepared to be used for XRD analysis.

Table 4.2 shows the rock forming minerals for each rock type. All three types of rock include quartz, which has a high thermal conductivity. While the thermal conductivities of most minerals are 2 to 4 W/mK, the thermal conductivity of quartz is 7.7 W/mK (Horai, 1971). Since the influence of quartz is the most significant among the minerals that form the rocks, quartz contents in samples with different anisotropy angle were analyzed (Figure 4.4).

Table 4.2 Rock forming minerals for rock type

Rock type	Rock forming minerals
Asan gneiss	Quartz, Albite, Biotite, Microcline, Chlorite, hornblende
Boryeong shale	Muscovite, Quartz, Chlorite
Yeoncheon schist	Quartz, Biotite, Albite, Muscovite, Chlorite

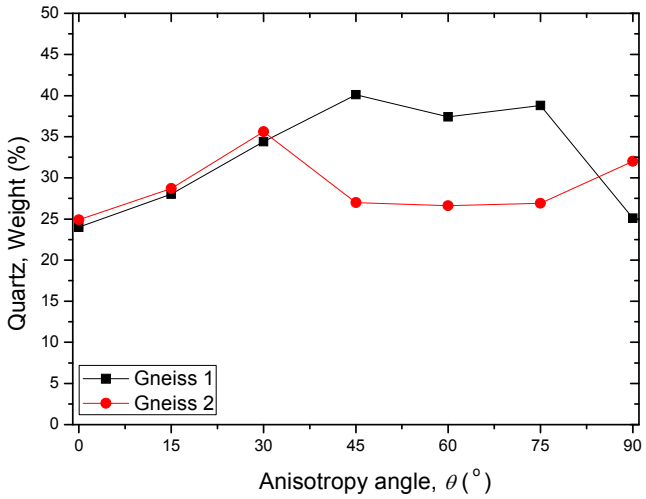

(a) Asan gneiss

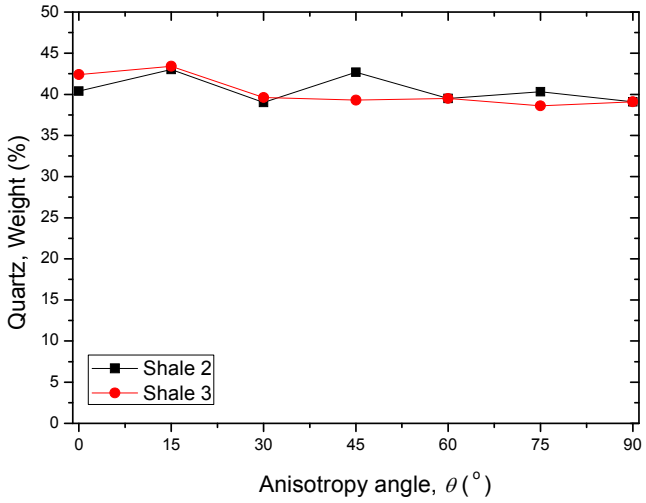

(b) Boryeong shale

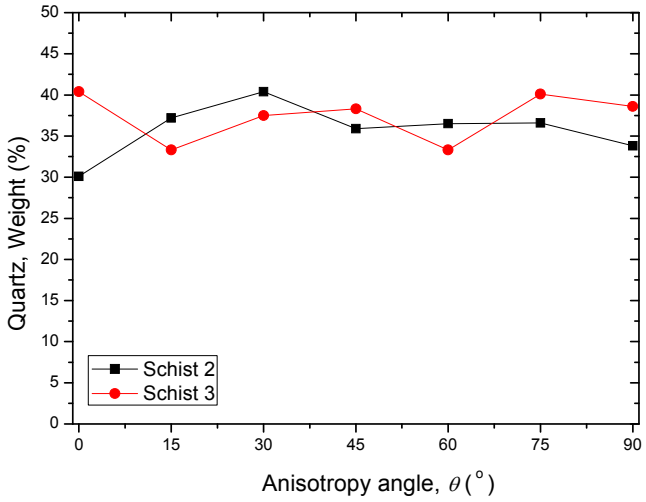

(c) Yeoncheon schist

Figure 4.4 Quartz content with anisotropy angle obtained from XRD

Overall, the quartz content of the rocks is spread fairly evenly throughout the rocks, irrespective of anisotropy angle. The lack of a definite variation of quartz content with anisotropy angle corroborates the anisotropy results of thermal properties obtained in this study. The isotropic distribution of quartz was observed more clearly in shale, which is composed of finer minerals, such as muscovite. The biggest variation in quartz content was observed in gneiss, and these variations in two sets appeared to be correlated to some extent with the thermal conductivity measurements.

4.4. Comparison of measured properties and properties predicted theoretically by tensorial transformation

In order to quantify the applicability of the tensorial properties, a comparison between measured and predicted values was obtained using a parameter called 'mean prediction error (*MPE*)', which was defined by Cho et al. (2012) as:

$$MPE = \frac{1}{N}\sum_{i=0}^{90}\left|\frac{y_{\theta(ex)} - y_{\theta(th)}}{y_{\theta(th)}}\right| \tag{4.1}$$

where $y_{\theta(ex)}$ is the experimental result, $y_{\theta(th)}$ is the theoretically-predicted

value, and N is the number of prediction points.

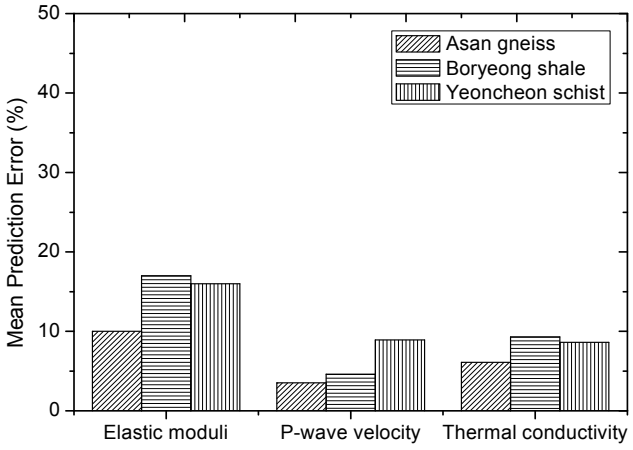

Figure 4.5 Mean prediction error of elastic moduli, P-wave velocities, and thermal conductivities

Figure 4.5 shows the mean prediction error of elastic moduli, P-wave velocities, and thermal conductivities for the three types of rock in which the experimental results were compared with the predictions based on tensorial transformation. The calculated mean prediction errors of the P-wave velocities for Asan gneiss, Boryeong shale, and Yeoncheon schist were 3.5%, 4.6%, and 8.9%, respectively. These values are considered to be relatively small, and this implies that the transversely isotropic model is a reasonable constitutive model for the specific rocks tested in this study. The discrepancy observed in this comparison may be due to heterogeneity or the possible

existence of a second anisotropic structure that may require an alternative anisotropic model, such as an orthotropic or a monoclinic model. With more microscopic investigation and directional coring in the three dimensions, we might have found some other anisotropic texture, such as an independently-oriented set of lineations, microcracks, or mineral elongations (Song et al., 2004)

Our prediction of thermal conductivity was based on a second-order tensor transformation using Eq. (2.12). The prediction line was constructed based on the measurement of two sets of samples with anisotropy angles of 90° and 0°. Even though there are some deviations between the measured and predicted values due to heterogeneity, the *MPE*s of the thermal conductivities of the Asan gneiss, Boryeong shale, and Yeoncheon schist were 6.1%, 9.3%, and 8.6%, respectively. These results show that thermal conductivity can be treated as a second-order tensor with less than 10% error for the rock types used in this study.

In all three properties, *MPE*s were generally smaller than 17%. Especially *MPE*s of thermal and seismic properties were less than 10%, these results showed that these properties can be modeled effectively as second-order tensors or approximated by equations for the types of rocks assessed in this study. This *MPE* can be a useful parameter as a criterion to

determine whether the selected rock follows the transversely isotropy model. Importantly, the discrepancies between the theoretical constitutive relationships and experimental observations were quantified in this study. The reason that there were greater errors in the prediction of elastic moduli may be explained by the strain measurement method. In the mechanical test, strain was determined by strain gauges that covered a small area relative to the whole surface of sample. Thus this method could be less representative of actual conditions than the responses that passed through the entire sample for measuring the properties of P-wave velocity and thermal conductivity.

4.5. Comparison of anisotropy ratio for mechanical, s eismic, and thermal properties

The anisotropic behaviours of elastic moduli, P-wave velocities, and thermal conductivities are compared in Figure 4.6 based on the measurements from samples with all anisotropy angles. In general, the correlation of elastic moduli and P-wave velocities and that of elastic moduli and thermal conductivities are less than that of thermal conductivities and P-wave velocities. It is noted that the samples used for testing the mechanical properties were not identical to those used for testing the seismic and thermal properties even though the samples were cored from the same rock

block and this could have affected the results. Asan gneiss showed the poorest correlation among three rock types and this can be explained by the heterogeneous rock samples caused by the existence of quartz veins.

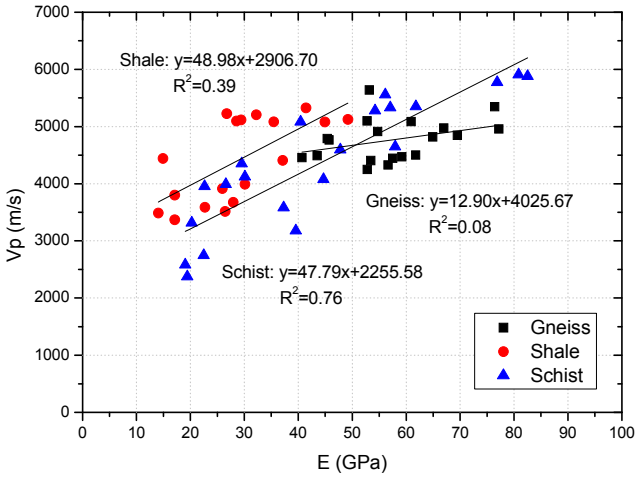

(a) Elastic moduli and P-wave velocities

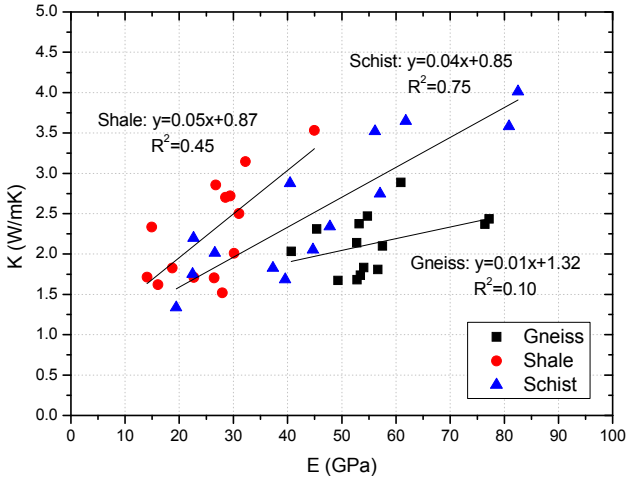

(b) Elastic moduli and thermal conductivities

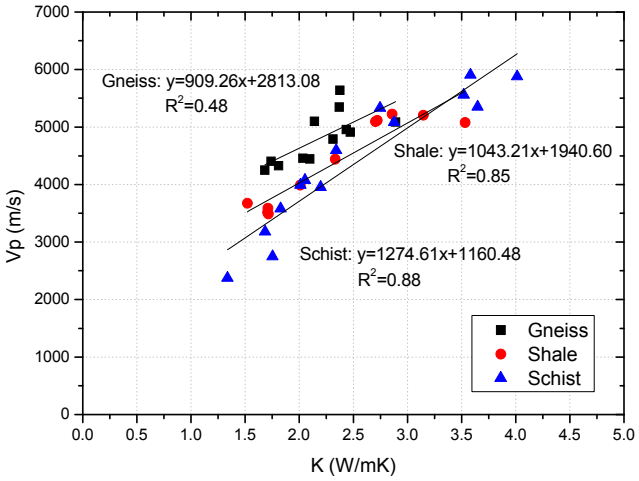

(c) Thermal conductivities and P-wave velocities

Figure 4.6 Correlation between (a) elastic moduli and P-wave velocities, (b) elastic moduli and thermal conductivities, and (c) thermal conductivities and P-wave velocities

The best correlations are observed among other comparisons between thermal conductivities and P-wave velocities. Theoretically, thermal conductivity varies with specific heat, density, the propagation velocity of phonons, and seismic velocity. Seismic velocities of minerals, which compose rocks, generally increase with thermal conductivity (Kukkonen and Peltoniemi, 1998). Previous researchers conducted regression analyses between thermal conductivity and P-wave velocity (Hartmann et al., 2005; Ozkahraman et al., 2004). Also, Johnson and Wenk (1974) investigated the relationship between the anisotropies of thermal diffusivity and elastic

velocity and found that the degree of anisotropy associated with thermal diffusivity was approximately proportional to the degree of anisotropy associated with elastic velocity. Although the relationships established in previous studies cannot be applied directly in the current study, the results of our study basically confirmed the findings of the previous studies. These results are useful in that they can be used to estimate the anisotropy of a property when the anisotropy of a correlated property is known.

Clearly, additional work needs to be conducted to answer the question concerning whether anisotropy observed in this study, can be representative of anisotropy that would be observed with the application of confining pressure. Several researchers have reported that the anisotropy in sedimentary rock actually changed as the confining pressure was changed (Johnston and Christensen, 1995; Park, 2011; Song et al., 2004). This observation may be more applicable for sedimentary rock in which microstructures are more vulnerable to changes in stress. It is known that microcracks play a more significant role at low pressure levels, whereas microstructural orientation mainly governs the anisotropy at higher pressures (Kern, 1993).

For further research, it will be possible to simultaneously measure additional physical properties, such as permeability, electrical conductivity,

and magnetic properties on the same rock sample, which will enable us to have a more complete picture of the correlation between various physical properties.

Chapter 5. Borehole stability in isotropic rock

5.1. Stress distribution around a borehole – analytic study

The stress concentration around a vertical well drilled parallel to the vertical principal stress, S_v, in an isotropic, elastic medium is described by the Kirsch equations (Zoback, 2007).

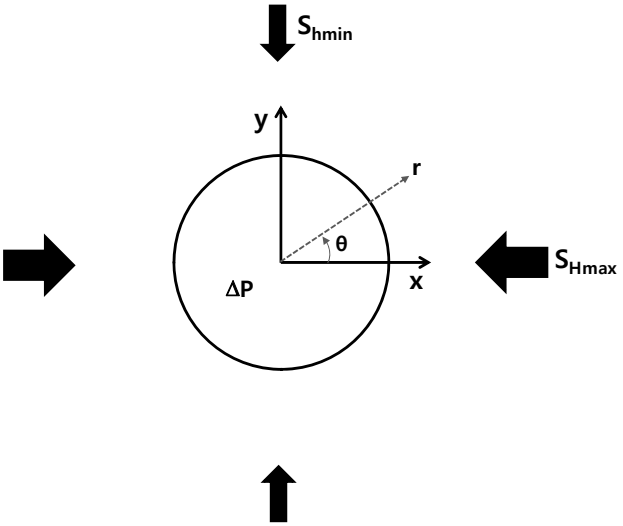

Figure 5.1 The state of stress around a circular hole in an infinite elastic rock mass with far field stress S_{Hmax} acting in the x direction and far field stress S_{hmin} acting in the y direction

As illustrated in Figure 5.1 the stresses around the borehole under plane strain condition can be mathematically described as follows.

$$\sigma_{rr} = \frac{1}{2}\left(S_{H\max} + S_{h\min}\right)\left\{1 - \left(\frac{R}{r}\right)^2\right\} + \frac{1}{2}\left(S_{H\max} - S_{h\min}\right)$$
$$\times\left\{1 - 4\left(\frac{R}{r}\right)^2 + 3\left(\frac{R}{r}\right)^4\right\}\cos 2\theta + \Delta P\left(\frac{R}{r}\right)^2$$
$$\sigma_{\theta\theta} = \frac{1}{2}\left(S_{H\max} + S_{h\min}\right)\left\{1 + \left(\frac{R}{r}\right)^2\right\} - \frac{1}{2}\left(S_{H\max} - S_{h\min}\right) \qquad (5.1)$$
$$\times\left\{1 + 3\left(\frac{R}{r}\right)^4\right\}\cos 2\theta - \Delta P\left(\frac{R}{r}\right)^2$$
$$\tau_{r\theta} = -\frac{1}{2}\left(S_{H\max} - S_{h\min}\right)\left\{1 + 2\left(\frac{R}{r}\right)^2 - 3\left(\frac{R}{r}\right)^4\right\}\sin 2\theta$$
$$\sigma_{zz} = S_v - 2\nu\left(S_{H\max} - S_{h\min}\right)\left(\frac{R}{r}\right)^2\cos 2\theta$$

Where each stress denotes the radial stress (σ_{rr}), the tangential (hoop or circumferential) stress ($\sigma_{\theta\theta}$), the tangential shear stress ($\tau_{r\theta}$), and axial stress (σ_{zz}) in a cylindrical coordinate system. S_{Hmax} and S_{hmin} are far field and it means the maximum and the minimum horizontal stress actually. The angle θ is measured from the azimuth of S_{Hmax}, r is the radial distance from the center of the well, and ΔP is the difference between the fluid pressure in the borehole and that in the rock formation. As it is conventional to assume that $S_{Hmax} \geq S_{hmin}$, in the above equations, it is implicit that the x-axis is aligned with the direction of the maximum principal stress.

At the surface of the hole, the tangential stress $\sigma_{\theta\theta}$ varies with θ according to

$$\sigma_{\theta\theta} = \left(\mathrm{S}_{\mathrm{Hmax}} + \mathrm{S}_{h\min}\right) - 2\left(\mathrm{S}_{\mathrm{Hmax}} - \mathrm{S}_{h\min}\right)\cos 2\theta \qquad (5.2)$$

Therefore the tangential stress varies from a minimum value of $3S_{Hmax}$ - S_{hmin} when $\theta = 0$ or π, to a maximum value of 3 S_{hmin} - S_{Hmax} when $\theta = \pi/2$ or $3\pi/2$ (Zoback, 2007). At the point far from the borehole (R/r =0), the tangential stress $\sigma_{\theta\theta}$ and radial stress σ_{rr} varies as follows.

$$\frac{1}{2}\left(S_{H\max} + S_{h\min}\right) - \frac{1}{2}\left(S_{H\max} - S_{h\min}\right)\cos 2\theta$$

$$\frac{1}{2}\left(S_{H\max} + S_{h\min}\right) + \frac{1}{2}\left(S_{H\max} - S_{h\min}\right)\cos 2\theta \qquad (5.3)$$

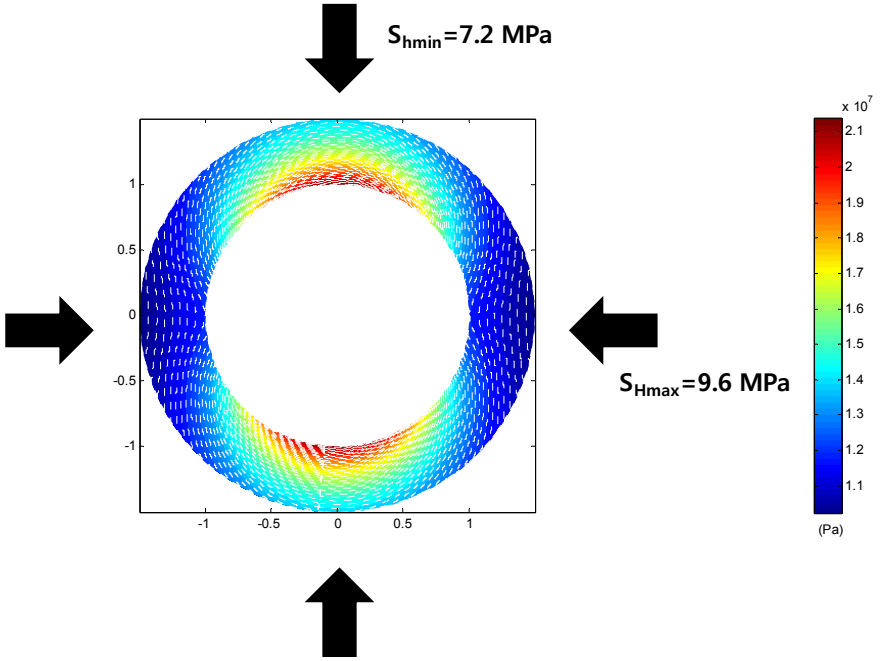

Figure 5.2 Variation of tangential stress, $\sigma_{\theta\theta}$ around a vertical well of radius R subject S_{Hmax} acting in an east–west. $\sigma_{\theta\theta}$ varies strongly with both position around the wellbore and distance from the wellbore wall. (Data from (Chang et al., 2010))

There are several important points about Kirsch equations. The stress concentration varies strongly as a function of position around the borehole (θ) and distance from the borehole wall (r). Also, the stress concentration is symmetric with respect to the direction of the horizontal principal stresses.

The tangential stress, $\sigma_{\theta\theta}$, is strongly compressive to 90◦ from the direction of S_{Hmax}. Figure 5.4 shows the variation of $\sigma_{\theta\theta}$, σ_{zz} and σ_{rr} at the borehole wall for the same far field stresses used following parameters in Table 5.1. Those

are from specific location, Pohang, in 300m depth (Chang et al., 2010). The vertical stress (S_v) is calculated from the weight of the overburden (a unit-weight of 26.5 kN/m^3 assumed, which is equivalent to an average rock density of 2.65 g/cm^3). Each horizontal stress (S_{Hmax} and S_{hmin}) is calculated based on stress ratio of Pohang in stress ratio contour map (Figure 5.3). In this study, it is assumed that K_{min} (= S_{hmin} / S_v) is 0.9 and K_{max} (= S_{Hmax} / S_v) is 1.2.

Table 5.1 Parameters used to examine the variation of $\sigma_{\theta\theta}$, σ_{zz} and σ_{rr} at the borehole wall in isotropic rock

S_{Hmax}	9.6 MPa
S_{hmin}	7.2 MPa
S_v	8 MPa (depth 300m)
ΔP	0 MPa

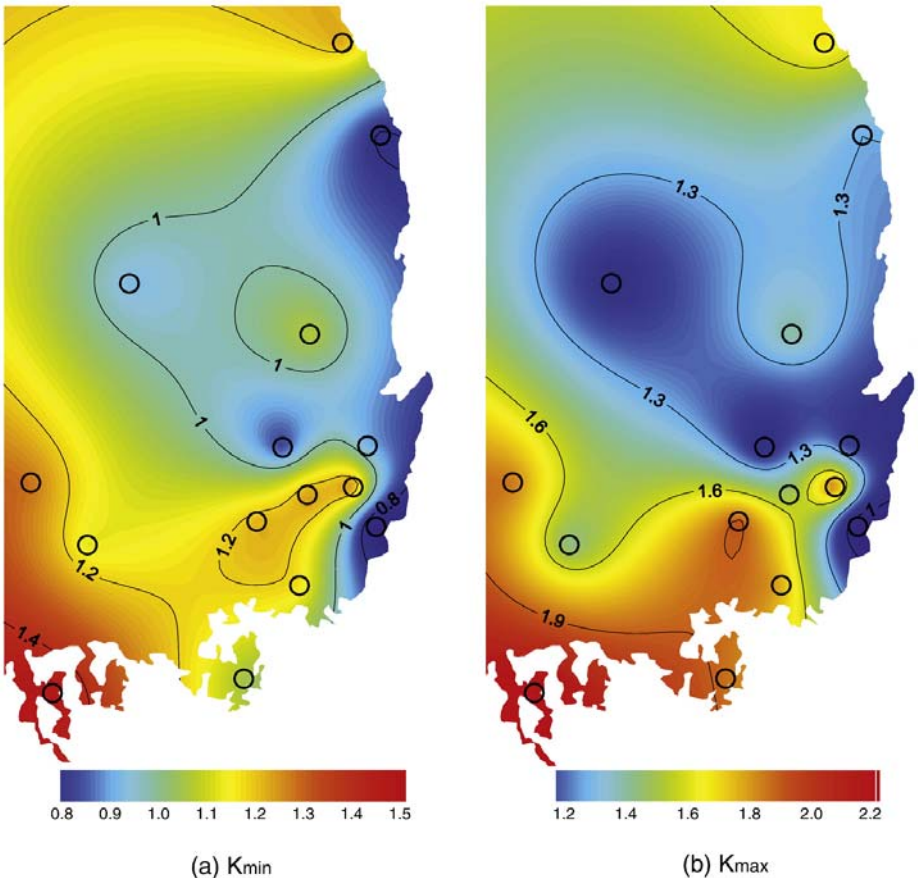

Figure 5.3 Stress ratio contour map in southeast of Korea: (a) K_{min} (= S_{hmin} / S_v) (b) K_{max} (= S_{Hmax} / S_v) (Chang et al., 2010)

The large variation in $\sigma_{\theta\theta}$ is observed with position around the well. σ_{zz} varies in a similar manner but the variation is more moderated. And σ_{rr} is zero at the wall.

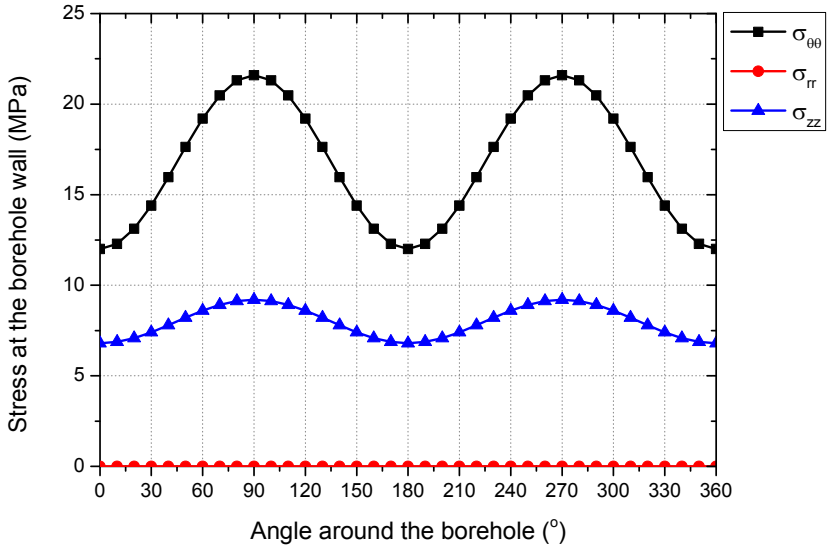

Figure 5.4 Variation of stresses, $\sigma_{\theta\theta}$, σ_{rr} and σ_{zz} at the wall of borehole in isotropic rock

In Figure 5.2 and Figure 5.4 it is obvious that compressive failure of the wellbore wall is most likely to occur in the area of maximum compressive tangential stress, at the direction of S_{hmin}, if the compressive stress exceeds the rock compressive strength. Further discussion will be described in Section 5.3.

5.2. Stress distribution around a borehole – numerical study

A general finite element simulator, COMSOL Multiphysics 4.2a, was used to analyze the stress concentration in isotropic rock and to simulate the Kirsch equations.

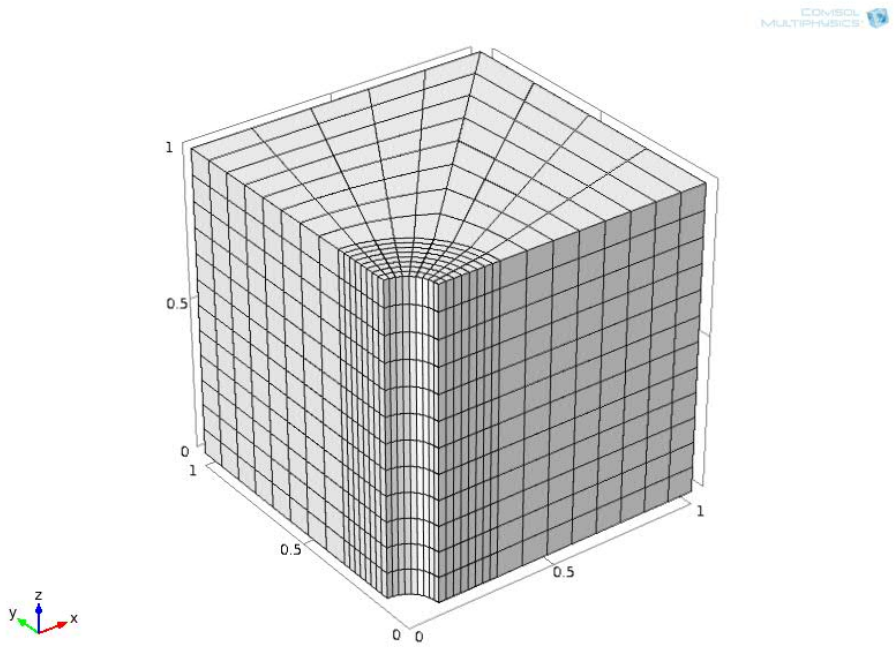

Figure 5.5 3D numerical finite element model

The 3D finite element model is shown in Figure 5.5. The radius of hole is 0.1 m and the far boundaries in x- and z-directions are situated ten-hole-diameters away from the axis of the hole, and the side length of the domain

is 1m and thickness is 1m. For the convenience of calculation the quarter symmetry model was analyzed in this study. Parameters used in the numerical study are from average value of elastic parameters from Boryeong shale (Table 4.1 in Section 4.1).

Table 5.2 Parameters used to analyze the stress concentration in isotropic rock

E	39.3 GPa
ν	0.18
$G = \frac{E}{2(1+\nu)}$	16.65GPa

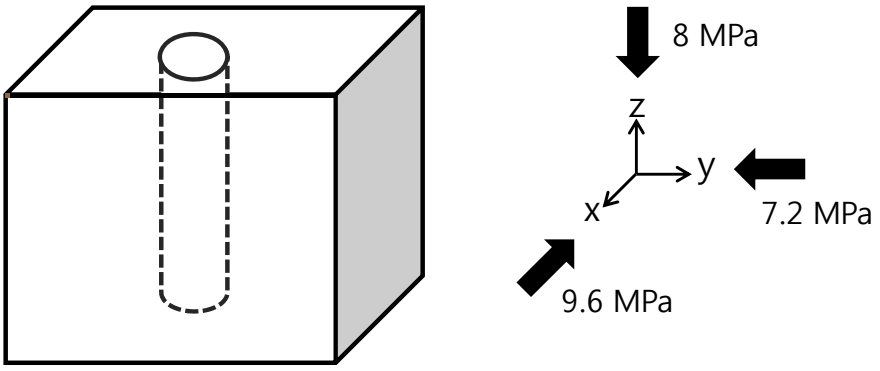

Figure 5.6 Isotropic model and boundary condition

The same boundary condition in Table 5.1 was applied in numerical study (Figure 5.6). Figure 5.7 show the variations of the tangential stress ($\sigma_{\theta\theta}$) and radial stress (σ_{rr}) in isotropic rock domain. The contours of tangential stress ($\sigma_{\theta\theta}$) and radial stress (σ_{rr}) vary across x-y domain. The analytic and numerical results were compared in Figure. 5.8 and they show good agreements.

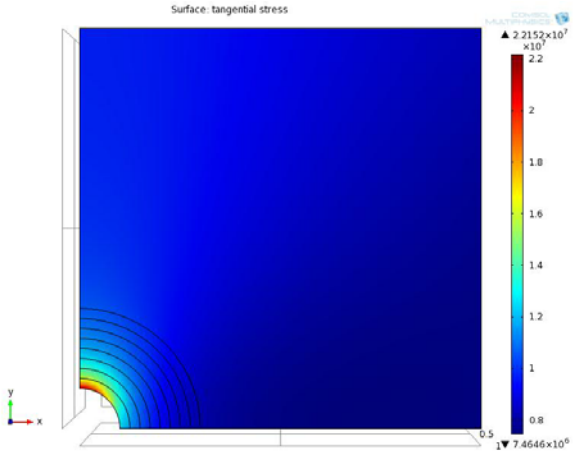

(a) Variation of tangential stress in isotropic rock

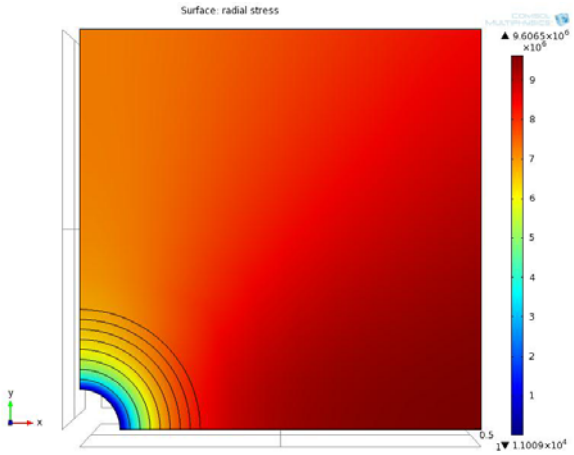

(b)Variation of radial stress in isotropic rock

Figure 5.7 Variation of tangential and radial stress in isotropic rock (unit: Pa)

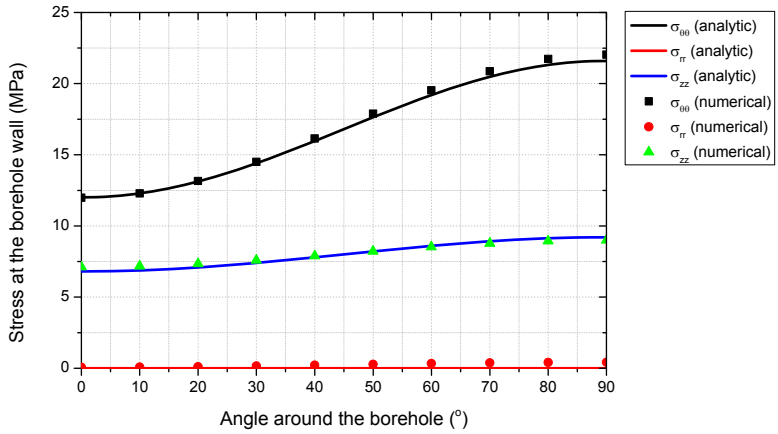

(a) Stress concentration around the borehole wall in isotropic rock

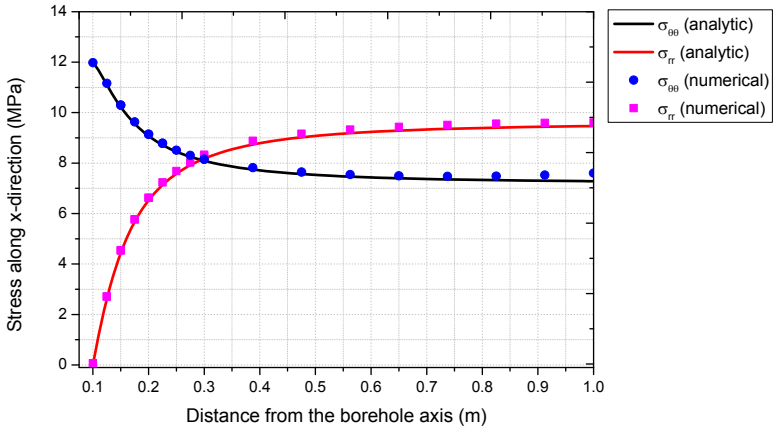

(b) Stress distribution along x direction in isotropic rock

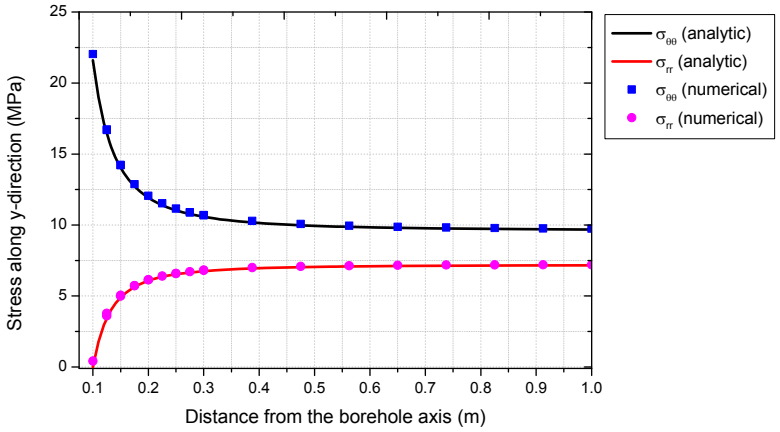

(c) Stress distribution along y direction in isotropic rock

Figure 5.8 Stress distribution of analytic and numerical results in isotropic rock

5.3. Borehole breakout

According to the Kirsch equations, the stress components at any point (r, θ) in the horizontal plane around the hole can be expressed as the radial stress (σ_{rr}), the tangential stress ($\sigma_{\theta\theta}$), and the shear stress ($\tau_{r\theta}$). Due to stress concentration, shear failure occurs along conjugate surfaces intersecting in the directions of the minimum horizontal principal stress.

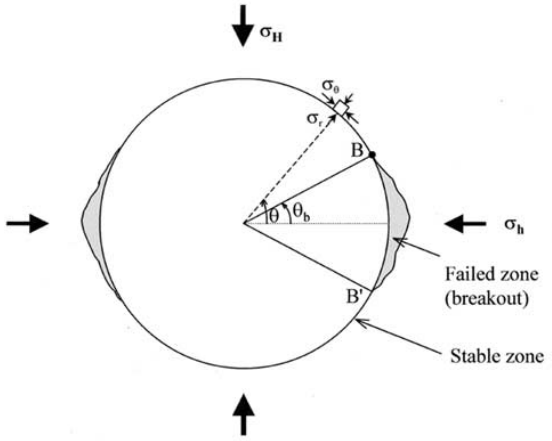

Figure 5.9 Schematic cross-section of a borehole showing a compressive failure zone known as breakout (Haimson and Chang, 2002)

It is important to note that the magnitude of the shear and normal stresses along these potential failure surfaces varies as a function of r and the angle θ.

It is assumed that failure of the rock near the borehole wall occurs in accordance with the Mohr-Coulomb criterion. At each point (r, θ), it is assumed that the maximum and minimum principal stresses are in the horizontal plane and the failure surfaces are parallel to the borehole vertical axis. The rock is assumed to have a coefficient of internal friction μ=tan φ (where φ is an internal friction angle) and cohesion C. According to the Mohr-Coulomb criterion, the shear stress τ and the effective normal stress σ on the failure surfaces are related as follows.

$$\tau = C + \mu\sigma \tag{5.4}$$

Rearrangement of Eq.(5.4) gives the following expression for the cohesion at failure in terms of μ and the stress components σ_{rr}, $\sigma_{\theta\theta}$ and $\tau_{r\theta}$,

$$C = \sqrt{1+\mu^2}\sqrt{\left(\frac{\sigma_{\theta\theta}-\sigma_{rr}}{2}\right)^2 + {\tau_{r\theta}}^2} - \mu\left(\frac{\sigma_{\theta\theta}+\sigma_{rr}}{2}\right) \tag{5.5}$$

Substituting Eq.(5.1) into Eq.(5.5) , the cohesion can be expressed in terms of r, θ and the horizontal principal stresses, S_{Hmax} and S_{hmin} (Zoback et al., 1985). Conversely, for given values of stresses S_{Hmax} and S_{hmin}, the cohesion C and the coefficient of internal friction μ, the extent of the breakout zone

where shear failure occurs can be determined (Amadei and Stephansson, 1997).

As an example, consider the case where S_{Hmax} =45MPa, S_{hmin} =30MPa, μ=1.0, C=12.5MPa and ΔP=0 (Zoback et al., 1985). (ΔP is the difference between the fluid pressure in the borehole and that in the formation. Positive indicates excess pressure in the borehole).

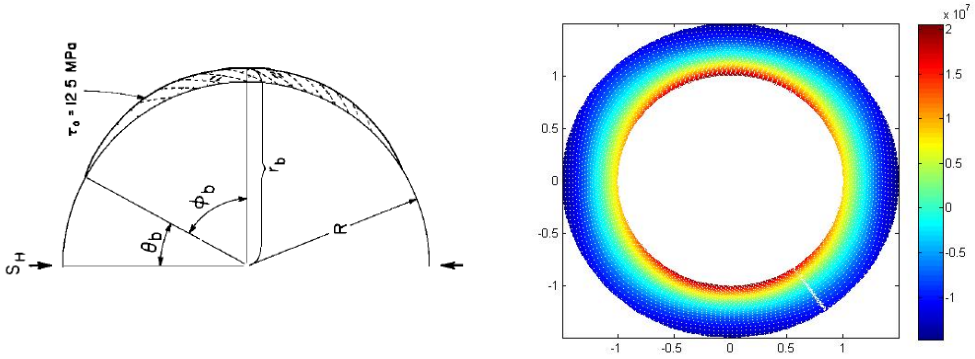

(a) (b)

Figure 5.10 (a) Area in which failure is expected for c=12.5MPa (Zoback et al., 1985). (b) The zone of failure around the borehole for the assumed rock strength is indicated by the contour line.

The size of the region in which the rock shear strength is actually mobilized is shown in Figure 5.10 (a). The zone of compressive failure around the borehole for the assumed rock strength is indicated by the contour line in Figure 5.10(b). In this case, red-orange contour line represents the borehole

breakout region with c = 12.5 MPa. The breakout region has a finite width, the span of failed rock around the wellbore wall on one side, and initial depth, both of which depend on rock strength for a given stress state (Zoback, 2007). The scale indicates the magnitude of rock strength required to inhibit failure. Hence, hot colors means it takes high strength to prevent failure because the stress concentration is high. Whereas cold colors mean even a low-strength rock will not fail because the stress concentration is low.

Figure 5.11 shows several other examples conducted by Zoback et al. (1985) for different stress values and coefficients of friction. The contours shown in this figure are envelopes enclosing the region in which the ratio of shear to normal stress is large enough to cause failure for the given value of C and $\Delta P = 0$. Figure 5.11 illustrates that the breakout shapes are generally broad and flat-bottomed. For given values of stresses and μ, the lower the cohesive strength of the rock, the deeper and wider the breakout region. For example, in the case where S_{hmin}= 10 MPa, S_{Hmax} = 15 MPa, and $\mu = 0.5$, no breakout would be observed in a borehole drilled in rock with a cohesive strength higher than 10 MPa. However, if the cohesive strength were much lower than 6 MPa, the breakouts would be so large as to extend nearly around the borehole. It can be also seen in this figure that the effect of increasing the ratio of the horizontal principal stresses is to make the

breakouts much larger for a given value of μ and C. Similarly, for a given stress ratio and C, much smaller breakouts result for larger values of μ, especially for the larger stress ratios. One interesting feature in the case of the 3:1 stress ratio is the change in shape of large breakouts (Zoback et al., 1985).

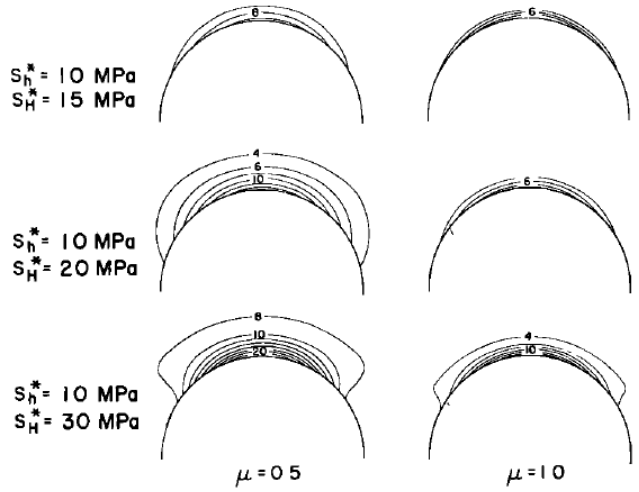

Figure 5.11 Theoretical size of the areas in which the compressive shear strength of the rock is exceeded by the concentrated stresses. For the values of the effective compressive principal stress and coefficient of friction shown, the contours in each figure define the size of the initial failure zone for a given value of C and ΔP=0 (Zoback et al., 1985).

To verify these results, the same procedure was conducted using the data of Figure 5.11 and the results are shown as Fig.5.11. As mentioned

above, it was revealed that for given values of μ, C and ΔP=0 increasing the stress ratio S_{Hmax}/S_{hmin} up to a value of 3 makes the breakouts much larger with steeper edges. Similarly, for given values of the stress ratios and C, much smaller breakouts occur for larger values of μ. And for given values of the stress ratio and μ, the breakouts become deeper and wider with the lower C value. In the case of the 3:1 stress ratio the shape of breakout changes. In general, the edges of the breakouts steepen as the stress ratio increases (Zoback et al., 1985).

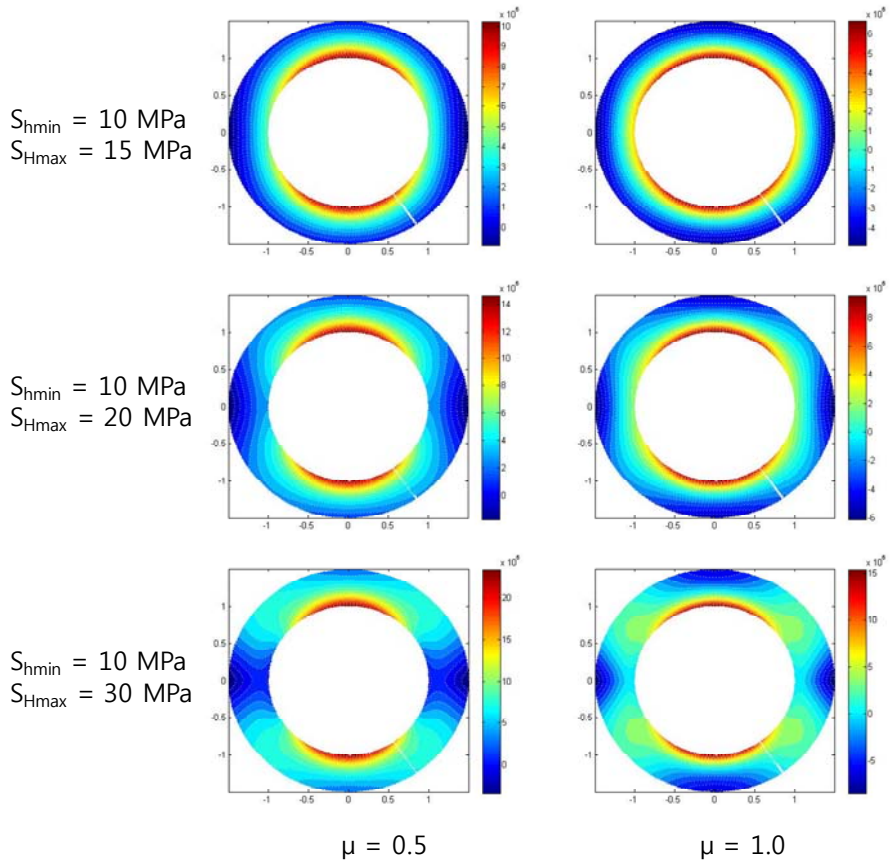

Figure 5.12 The results of numerical analysis with data used in Figure 5.11

The theory mentioned above for the initial formation of breakouts can explain the broad, flat-bottomed breakouts observed in many boreholes, but cannot explain the deeper breakouts. In the analysis above, it was assumed that ΔP=0. ΔP is the difference between the fluid pressure in the borehole and that in the formation. Positive indicates excess pressure in the borehole. Zoback et al (1985) revealed that the strong influence of ΔP on the size and

shape of breakout is due to the change in normal stress on potential failure planes near the borehole. Positive ΔP inhibits failure and negative ΔP promotes failure.

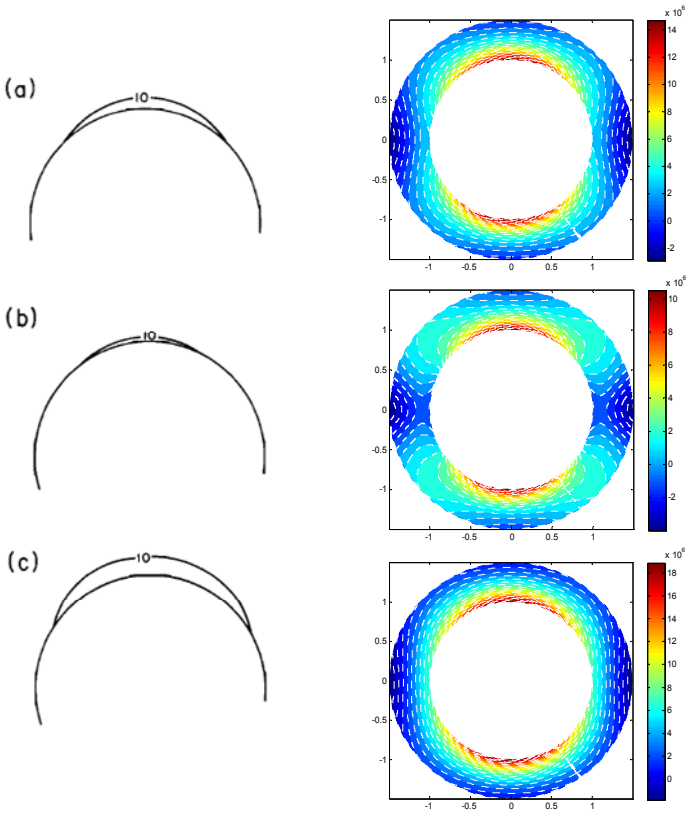

Figure 5.13 The effect of excess well bore fluid pressure ΔP on the size of well bore breakouts. Contours define the size of the initial failure zone for C = 10MPa when S_{Hmax} = 22.0M Pa, S_{hmin}= 11.0 MPa, and μ = 0.6. (a) ΔP = 0, (b) ΔP = 2.5, (c) ΔP = -2.5 (Zoback et al., 1985)

The theory and examples presented above are intended to explain the initial

size and shape of borehole breakouts. Further, the calculations indicate that as the breakouts deepen, they do not become wider. This explains why breakouts with markedly different depths have approximately the same width (Zoback et al. 1985). This theory suggests obviously simple failure model, but it does not consider the inelastic behavior occurring as the rock around the borehole fails and the corresponding stress redistribution (Amadei and Stephansson, 1997).

Chapter 6. Borehole stability in transversely isotropic rock

6.1. Stress distribution around a borehole – analytic study

6.1.1. Analytic solution for anisotropic rock

Understanding the stress components around the borehole is greatly important to analyze the borehole stability. Almost all rocks are anisotropic to some extent and the assumption of isotropy can result in erroneous results. The objective of this section is to give a brief conceptual overview on how the equations for stresses around a borehole in anisotropic rock are derived. The formulation introduced in this thesis is based on Lekhnitskii (1963) and Amadei (1982).

6.1.2. Geometry and coordinate system transformation

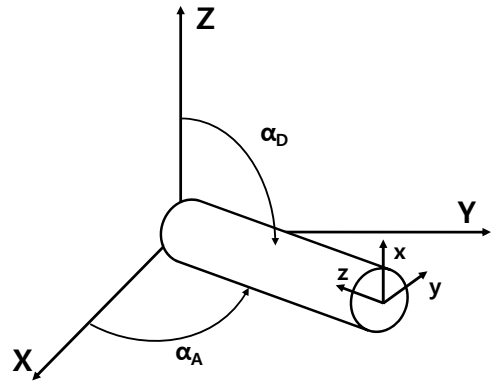

Figure 6.1 Borehole coordinate system – global coordinate system

Consider the elastic equilibrium of an anisotropic, homogeneous, continuous body that possesses rectilinear anisotropy of a general form. It is bounded internally by a cylindrical surface of circular cross-section. The medium is of infinite extent; the body is under the influence of a stress tensor at infinity and a wellbore pressure uniformly distributed along its internal surface.

In the far-field an in-situ stress field is applied where the principal stress tensor takes the following form:

$$\sigma = \begin{pmatrix} \sigma_H & 0 & 0 \\ 0 & \sigma_h & 0 \\ 0 & 0 & \sigma_v \end{pmatrix} \tag{6.1}$$

where σ_H and σ_h are the maximum and minimum horizontal stresses respectively and σ_v is the vertical stress. It is assumed that (X,Y, Z) is a fixed global coordinate system (Figure 6.1) where the X, Y and Z axes are parallel to the maximum (σ_H), minimum (σ_h) and vertical (σ_v) stresses, respectively. For the computation of the borehole stress concentration it is convenient to rotate the stress field in the global XYZ coordinate frame into the top-of-hole (TOH) borehole coordinate system. The coordinate transform of XYZ stress tensor σ_{TOH} is

$$\sigma_{TOH} = T_t(\alpha_D, \alpha_A)\,\sigma_{XYZ}\; T_t(\alpha_D, \alpha_A)^T \tag{6.2}$$

where α_D and α_A are the borehole deviation and azimuth respectively (Figure 6.1). α_A is the angle between the well axis and the orientation of the maximum principal stress (σ_H) measured anticlockwise from the X-axis. α_D is the angle between the orientation of the vertical stress and the well axis, measured clockwise from the Z-axis. The rotation matrix T_t which rotates the XYZ stress tensor into the TOH stress tensor is defined as

$$T_t(\alpha_D,\alpha_A)=\begin{pmatrix} l_x & m_x & n_x \\ l_y & m_y & n_y \\ l_z & m_z & n_z \end{pmatrix} \tag{6.3}$$

where the direction cosines are defined as

$$l_x=\cos(\alpha_D)\cos(\alpha_A),\ \ m_x=\cos(\alpha_D)\sin(\alpha_A),\ \ n_x=-\sin(\alpha_D)$$
$$l_y=-\sin(\alpha_A),\ \ m_y=\cos(\alpha_A),\ \ n_y=0$$
$$l_z=\sin(\alpha_D)\cos(\alpha_A),\ \ m_z=\sin(\alpha_D)\sin(\alpha_A),\ \ n_z=\cos(\alpha_D)$$

The solution of the stress concentration is obtained in the TOH frame in the Cartesian coordinates. Due to geometry of the borehole problem it is natural to transform the borehole stress components into cylindrical coordinates. The transformed stress components in the borehole cylindrical coordinates are:

$$\begin{bmatrix} \sigma_{rr} \\ \sigma_{\theta\theta} \\ \sigma_{zr} \\ \tau_{\theta z} \\ \tau_{rz} \\ \tau_{r\theta} \end{bmatrix} = \begin{bmatrix} \cos^2\theta & \sin^2\theta & 0 & 0 & 0 & \sin 2\theta \\ \sin^2\theta & \cos^2\theta & 0 & 0 & 0 & -\sin 2\theta \\ 0 & 0 & 1 & 0 & 0 & 0 \\ 0 & 0 & 0 & \cos\theta & -\sin\theta & 0 \\ 0 & 0 & 0 & \sin 2\theta & \cos 2\theta & 0 \\ -\frac{1}{2}\sin 2\theta & -\frac{1}{2}\sin 2\theta & 0 & 0 & 0 & \cos 2\theta \end{bmatrix} \begin{bmatrix} \sigma_{xx} \\ \sigma_{yy} \\ \sigma_{zz} \\ \tau_{yz} \\ \tau_{xz} \\ \tau_{xy} \end{bmatrix} \tag{6.4}$$

6.1.3. Governing equations

The stress, strain and displacement components must satisfy the constitutive

relations, the equations of equilibrium, the equations of compatibility for strains and the strain-displacement relations. As all measurements are obtained in the borehole, it is convenient to rotate the compliance tensor into the TOH frame. This is done by applying two Bond transformations to the 6×6 Voigt notation compliance matrix s_{ij} giving a_{ij}.

$$a_{ij} = T_\varepsilon T_\sigma{}^T s_{ij} T_\sigma T_\varepsilon{}^T \tag{6.5}$$

where the definitions of the Bond transformation matrices T_ε and T_σ are given as follows. T_ε takes into account the orientation of the borehole which is defined as

$$T_\varepsilon = \begin{pmatrix} l_x^2 & m_x^2 & n_x^2 & m_x n_x & n_x l_x & l_x m_x \\ l_y^2 & m_y^2 & n_y^2 & m_y n_y & n_y l_y & l_y m_y \\ l_z^2 & m_z^2 & n_z^2 & m_z n_z & n_z l_z & l_z m_z \\ 2l_y l_z & 2m_y m_z & 2n_y n_z & m_y n_z + m_z n_y & n_y l_z + n_z l_y & l_y m_z + l_z m_y \\ 2l_z l_x & 2m_z m_x & 2n_z n_x & m_x n_z + m_z n_x & n_x l_z + n_z l_x & l_x m_z + l_z m_x \\ 2l_x l_y & 2m_x m_y & 2n_x n_y & m_x n_y + m_y n_x & n_x l_y + n_y l_x & l_x m_y + l_y m_x \end{pmatrix} \tag{6.6}$$

where

$$l_x = \cos(\alpha_D)\cos(\alpha_A),\ \ m_x = \cos(\alpha_D)\sin(\alpha_A),\ \ n_x = -\sin(\alpha_D)$$
$$l_y = -\sin(\alpha_A),\ \ m_y = \cos(\alpha_A),\ \ n_y = 0$$
$$l_z = \sin(\alpha_D)\cos(\alpha_A),\ \ m_z = \sin(\alpha_D)\sin(\alpha_A),\ \ n_z = \cos(\alpha_D)$$

The orientation of the borehole is defined by the deviation angle a_D and

the azimuth angle a_A. T_σ takes into account the orientation of the material frame which has the form

$$T_\sigma = \begin{pmatrix} l_s^2 & m_s^2 & n_s^2 & 2m_s n_s & 2n_s l_s & 2l_s m_s \\ l_t^2 & m_t^2 & n_t^2 & 2m_t n_t & 2n_t l_t & 2l_t m_t \\ l_n^2 & m_n^2 & n_n^2 & 2m_n n_n & 2n_n l_n & 2l_n m_n \\ l_t l_n & m_t m_n & n_t n_n & m_t n_n + m_n n_t & n_t l_n + n_n l_t & l_t m_n + l_n m_t \\ l_n l_s & m_n m_s & n_n n_s & m_s n_n + m_n n_s & n_s l_n + n_n l_s & l_s m_n + l_n m_s \\ l_s l_t & m_s m_t & n_s n_t & m_s n_t + m_t n_s & n_s l_t + n_t l_s & l_s m_t + l_t m_s \end{pmatrix} \tag{6.7}$$

$$l_s = \cos(\beta_D)\cos(\beta_A),\ \ m_s = \cos(\beta_D)\sin(\beta_A),\ \ n_s = -\sin(\beta_D)$$
$$l_t = -\sin(\beta_A),\ \ m_t = \cos(\beta_A),\ \ n_t = 0$$
$$l_n = \sin(\beta_D)\cos(\beta_A),\ \ m_n = \sin(\beta_D)\sin(\beta_A),\ \ n_n = \cos(\beta_D)$$

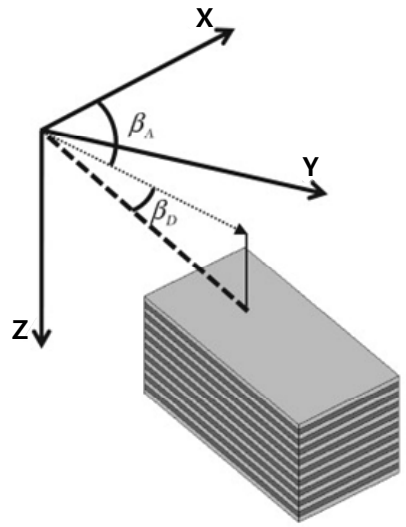

Figure 6.2 Material coordinate system for transversely isotropic medium with tilted symmetry axis (modified from Gaede et al. (2012))

The orientation of transverse isotropy with tilted axis of symmetry material is defined by the dip angle β_D and the azimuth β_A. (Figure 6.2)

In this study, only transversely isotropy with a vertical axis of symmetry, i.e. β_D=0 is considered.

At any position around the borehole, the strain is related to the stress in Cartesian coordinates via the constitutive relation. The only assumption made at this point is that $\varepsilon_{zz} = 0$ by plane strain condition.

6.1.4. General analytic solution for anisotropic medium

A general solution for the stresses around a borehole in an anisotropic medium can be found by using the concept of Airy stress functions. The general expressions for the borehole-induced stresses $\sigma_{induced}$ which can be superimposed onto the corresponding components of the far field in-situ stress tensor in the TOH frame σ_{TOH} to get the borehole stress tensor $\sigma_{borehole}$ are:

$$
\begin{aligned}
\sigma_{xx,borehole} &= \sigma_{xx,TOH} + \sigma_{xx,induced} \\
&= \sigma_{xx,TOH} + 2\,\mathrm{Re}\left[\mu_1^{\,2}\phi'_1(z_1) + \mu_2^{\,2}\phi'_2(z_2) + \lambda_3\mu_3^{\,2}\phi'_3(z_3)\right] \\
\sigma_{yy,borehole} &= \sigma_{yy,TOH} + \sigma_{yy,induced} \\
&= \sigma_{yy,TOH} + 2\,\mathrm{Re}\left[\phi'_1(z_1) + \phi'_2(z_2) + \lambda_3\phi'_3(z_3)\right] \\
\tau_{xy,borehole} &= \tau_{xy,TOH} + \tau_{xy,induced} \\
&= \tau_{xy,TOH} - 2\,\mathrm{Re}\left[\mu_1\phi'_1(z_1) + \mu_2\phi'_2(z_2) + \lambda_3\mu_3\phi'_3(z_3)\right] \\
\tau_{xz,borehole} &= \tau_{xz,TOH} + \tau_{xz,induced} \\
&= \tau_{xz,TOH} + 2\,\mathrm{Re}\left[\lambda_1\mu_1\phi'_1(z_1) + \lambda_2\mu_2\phi'_2(z_2) + \mu_3\phi'_3(z_3)\right] \\
\tau_{yz,borehole} &= \tau_{yz,TOH} + \tau_{yz,induced} \\
&= \tau_{yz,TOH} - 2\,\mathrm{Re}\left[\lambda_1\phi'_1(z_1) + \lambda_2\phi'_2(z_2) + \phi'_3(z_3)\right] \\
\sigma_{zz,borehole} &= \sigma_{zz,TOH} + \sigma_{zz,induced} \\
&= \sigma_{zz,TOH} - \frac{1}{a_{33}}\begin{pmatrix} a_{31}\sigma_{xx,induced} + a_{32}\sigma_{yy,induced} + a_{34}\tau_{yz,induced} \\ +a_{35}\tau_{xz,induced} + a_{36}\tau_{xy,induced} \end{pmatrix}
\end{aligned}
\tag{6.8}
$$

where $\phi'_i(z_i)$ are the spatial derivatives of three analytic functions which are defined as

$$
\begin{aligned}
\phi'_1(z_1) &= \gamma_1\begin{bmatrix} (\mu_3\lambda_2\lambda_3 - \mu_2)(\sigma_{yy,original} - i\tau_{xy,original} - P_w) + (\lambda_2\lambda_3 - 1)(\tau_{xy,original} - i\sigma_{xx,original} + iP_w) \\ +\lambda_3(\mu_3 - \mu_2)(\tau_{yz,original} - i\tau_{xz,original}) \end{bmatrix} \\
\phi'_2(z_2) &= \gamma_2\begin{bmatrix} -(\mu_3\lambda_1\lambda_3 - \mu_1)(\sigma_{yy,original} - i\tau_{xy,original} - P_w) + (1 - \lambda_1\lambda_3)(\tau_{xy,original} - i\sigma_{xx,original} + iP_w) \\ +\lambda_3(\mu_1 - \mu_3)(\tau_{yz,original} - i\tau_{xz,original}) \end{bmatrix} \\
\phi'_3(z_3) &= \gamma_3\begin{bmatrix} (\mu_2\lambda_1 - \mu_1\lambda_2)(\sigma_{yy,original} - i\tau_{xy,original} - P_w) + (\lambda_1 - \lambda_2)(\tau_{xy,original} - i\sigma_{x,original} + iP_w) \\ +(\mu_2 - \mu_1)(\tau_{yz,original} - i\tau_{xz,original}) \end{bmatrix}
\end{aligned}
$$

(6.9)

where

$$\gamma_j = \frac{1}{-2\Delta p_j \sqrt{\left(\frac{z_j}{a}\right)^2 - 1 - \mu_j^{\,2}}}, \quad \text{j=1, 2, 3}$$

and

$$p_j = \frac{\frac{z_j}{a} + \sqrt{\left(\frac{z_j}{a}\right)^2 - 1 - \mu_j^{\,2}}}{1 - i\mu_j}, \quad \text{j=1, 2, 3}$$

and

$$\Delta = \mu_2 - \mu_1 + \lambda_2\lambda_3\left(\mu_1 - \mu_3\right) + \lambda_1\lambda_3\left(\mu_3 - \mu_2\right)$$

μ_1, μ_2 and μ_3 are the positive roots of the characteristic equation $f(\mu)$.

$$f(\mu) = l_4(\mu)l_2(\mu) - l_3(\mu)l_3(\mu) = 0$$

$$\left.\begin{aligned} l_2(\mu) &= \beta_{55}\mu^2 - 2\beta_{45}\mu + \beta_{44} \\ l_3(\mu) &= \beta_{15}\mu^3 - \left(\beta_{14} + \beta_{56}\right)\mu^2 - \left(\beta_{25} + \beta_{46}\right)\mu - \beta_{24} \\ l_4(\mu) &= \beta_{11}\mu^4 - 2\beta_{16}\mu^3 + 2\left(\beta_{12} + \beta_{66}\right)\mu^2 - 2\beta_{26}\mu - \beta_{22} \end{aligned}\right\} \qquad (6.10)$$

where β_{ij} is the reduced strain coefficient

$$\beta_{ij} = a_{ij} - \frac{a_{i3}a_{j3}}{a_{33}} \quad \text{(i, j = 1, 2…, 6)} \qquad (6.11)$$

The coefficients λ_1, λ_2 and λ_3 are obtained from

$$\lambda_1 = -\frac{l_3(\mu_1)}{l_2(\mu_1)}$$
$$\lambda_2 = -\frac{l_3(\mu_2)}{l_2(\mu_2)} \qquad (6.12)$$
$$\lambda_3 = -\frac{l_3(\mu_3)}{l_4(\mu_3)}$$

Various plane strain problem can be fully solved by finding solutions to the analytic functions $\phi'_i(z_i)$ by applying the correct boundary conditions in the far-field as well as on the borehole wall (Amadei, 1982; Ong, 1994).

6.1.5. Special case of anisotropy

There are several cases to consider where a degeneration of the general solution happens (Amadei, 1982): (i) orthorhombic medium with one plane of elastic symmetry perpendicular to the hole axis (the two other planes being parallel to it), (ii) transverse isotropic medium with the plane of isotropy striking parallel to the hole axis, (iii) transverse isotropic medium with the plane of isotropy perpendicular to the hole axis and (iv) isotropic medium. It has been stated by Ong(Ong, 1994) that a solution for this problem can only be found for the above cases (i) and (ii), and that for cases (iii) and (iv), no solution can be found due to coincident roots which result in

singularities. Recently, Gaede et al. (Gaede et al., 2012) showed that this is not the case, and the solution actually works for any symmetry.

6.1.6. Degrees of rock anisotropy for transversely isotropic rock

In general, intact rocks are not too strongly anisotropic compared to other engineering materials such as wood or composites. Typical values of the five elastic constants of transversely isotropic rocks can be found in the literature. The elastic constants were mostly determined from the results of static or dynamic laboratory tests and assuming linear elastic theory. Amadei analyzed 98 measurements of elastic properties. They found that for most intact transversely isotropic rocks, the ratio E/E' varies between 1 and 4. Several cases of rocks with E/E' less than unity were found but did not fall below 0.7. The ratio G/G' was found to vary between 1 and 3, the Poisson's ratio, ν, between 0.1 and 0.35 and ν'E/E' between 0.1 and 0.7 (Amadei, 1996b).

6.1.7. Stress concentration for uniaxial stress condition

In order to investigate the stress concentration around the borehole depending on the anisotropy ratio (E/E'), the elastic constants of Boryeong

shale were used for analytic study. It is assumed that elastic modulus (E') vary with anisotropy ratio and shear modulus (G') vary with Saint-Venant empirical relationship.

In isotropic rock, the tangential stress ($\sigma_{\theta\theta}$) at the borehole wall with uniaxial stress P acting in the x-direction (Figure 6.3 (a)) varies with angle θ according to $\sigma_{\theta\theta} = P\left(1 - 2\cos 2\theta\right)$.

Therefore it varies from -P (i.e., tensile) when θ=0 or π, to compressive stress of 3P when θ= π/2 or 3π/2. If uniaxial stress P is acting in the y-direction, the result is opposite (Figure 6.3 (b)). But both cases show the same pattern with different loading direction.

In transversely isotropic rock, there are clear differences in two cases in stress concentration for uniaxial stress condition. First one is the case with uniaxial stress P acting in perpendicular to the isotropic plane (Figure 6.3 (a)) and the other is with uniaxial stress P acting in parallel to the isotropic plane (Figure 6.3 (b)).

Figure 6.4 shows the stress concentration for uniaxial condition with respect to the degree of anisotropy. Figure 6.4 (a) corresponds to boundary condition of Figure 6.3 (a) and Figure 6.4 (b) corresponds to Figure 6.3 (b).

The value of 3 indicates the maximum compressive tangential stress in isotropic rock. When the anisotropy ratio (E/E') is 2 and 3, the maximum

compressive tangential stress varies from 2.7 (Figure 6.4 (a)) to 3.3 (Figure 6.4 (b)), and from 2.6 (Figure 6.4 (a)) to 3.6 (Figure 6.4 (b)), respectively.. The value of -1 indicates the maximum tensile tangential stress in isotropic rock. When the anisotropy ratio (E/E') is 2 and 3, the maximum tensile tangential stress varies from -0.7 (Figure 6.4 (b)) to -1.3 (Figure 6.4 (a)) and from 0.6 (Figure 6.4 (b)) to-1.6 (Figure 6.4 (a)), respectively..

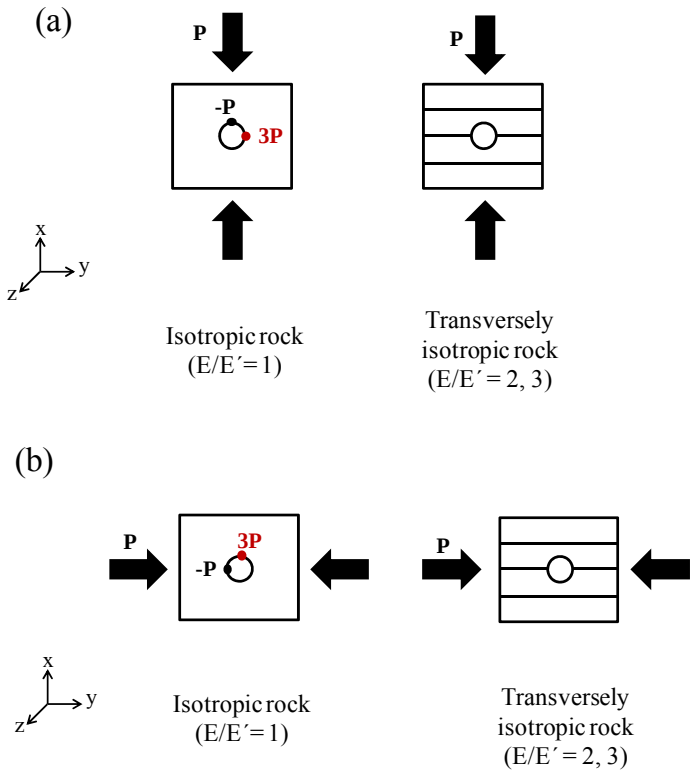

Figure 6.3 Diagram of stress concentration for uniaxial stress condition

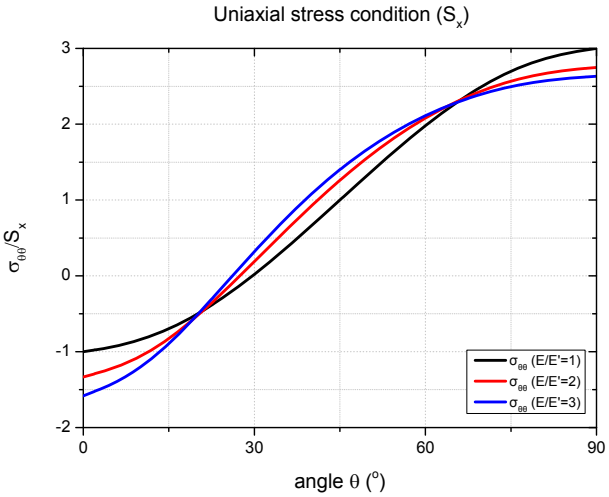

(a) Stress concentration for uniaxial condition, Sx

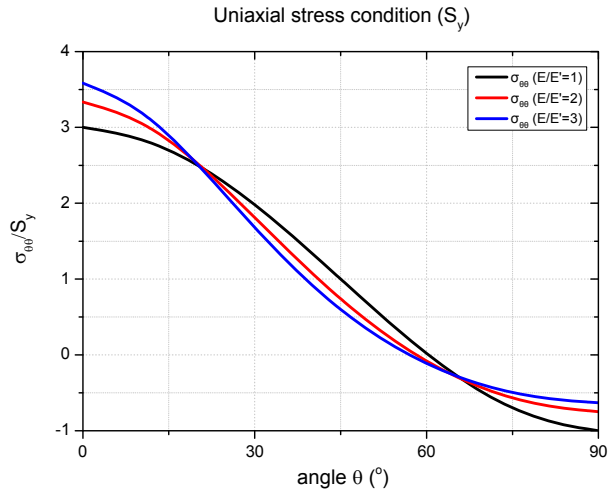

(b) Stress concentration for uniaxial condition, Sy

Figure 6.4 stress concentration for uniaxial condition with respect to the degree of anisotropy

6.1.8. Stress concentration for biaxial stress condition

Stress concentration around the borehole wall for biaxial stress condition can be calculated easily using superposition of uniaxial case (Figure 6.5). It is noted that each value in transversely isotropic case is approximated value.

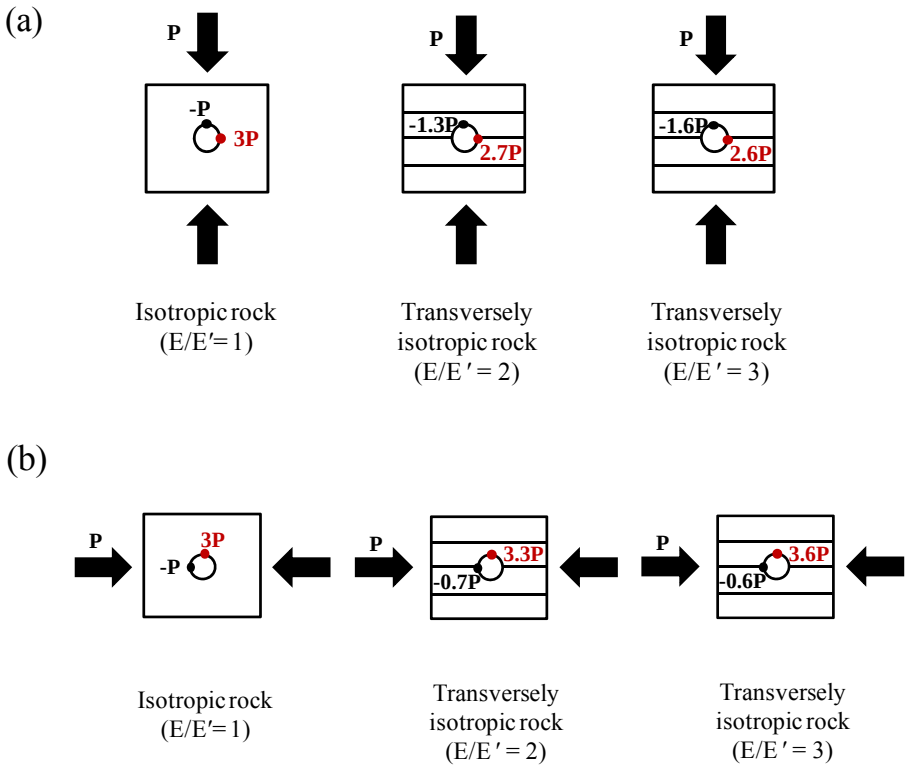

Figure 6.5 Stress concentration around the borehole with respect to degree of anisotropy

Figure 6.6 shows distribution of tangential stress around the borehole in

uniform biaxial stress condition. In this case, each stress of x and y-direction is offset by effect of superposition and there is no big difference between isotropic and anisotropic case in the normalized tangential stress.

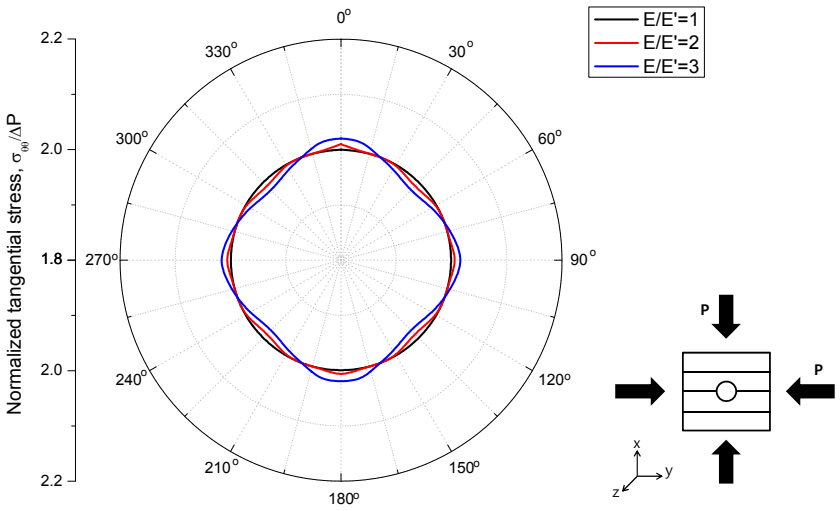

Figure 6.6 Distribution of tangential stress around the borehole in uniform biaxial stress condition

Figure 6.7 shows the stress concentration for nonuniform biaxial stress condition around the borehole wall. Although the stress concentration is different with respect to the boundary condition, it can be expected using simple superposition of Figure 6.5.

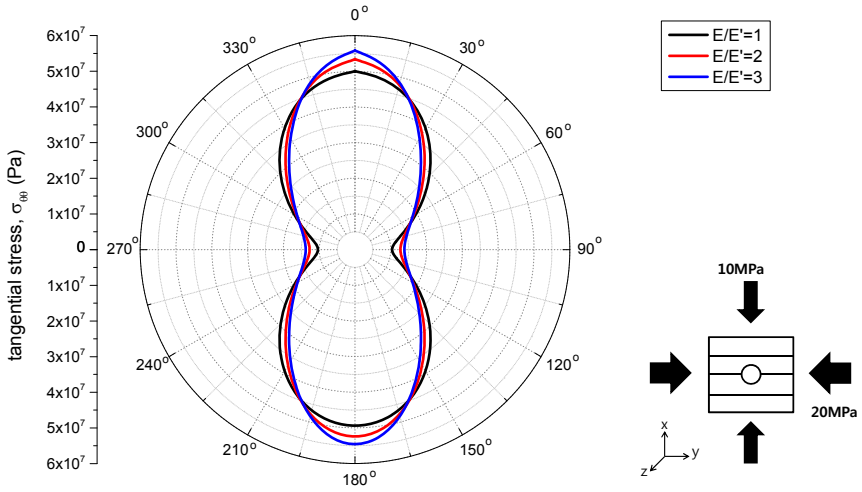

(a) Maximum stress direction is parallel to the isotropic plane

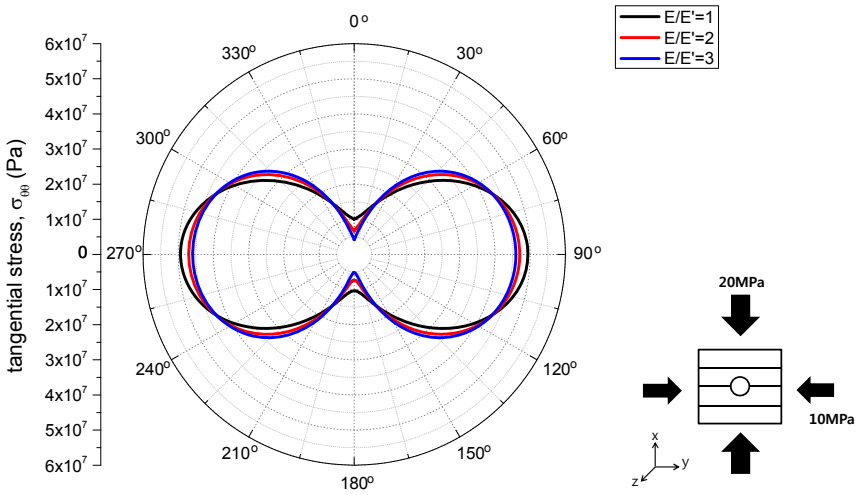

(b) Maximum stress direction is perpendicular to the isotropic plane

Figure 6.7 Tangential stress for nonuniform biaxial stress condition around the borehole wall

The stress concentration of transversely isotropic rock has large difference in the loading direction compared with isotropic case. When the maximum stress direction is parallel to the isotropic plane (Figure 6.7 (a)), the stress concentration in the loading direction increased with respect to the degree of anisotropy. When the maximum stress direction is perpendicular to the isotropic plane (Figure 6.7 (b)), the stress concentration in the loading direction decreased with respect to the degree of anisotropy.

Based on above observations, there seems to be no significant difference between E/E´=1 and E/E´=2 and the degree of anisotropy below 2 does not substantially affect the stress concentration at the borehole wall.

6.1.9. Stress concentration by internal pressure

At the borehole wall (R=r) in isotropic rock, the effect of internal pressure (ΔP) is constant regardless of angle (θ) according to Kirsch equations.

$$\sigma_{\theta\theta} = \left(S_{H\max} + S_{h\min}\right) - 2\left(S_{H\max} - S_{h\min}\right)\cos 2\theta - \Delta P$$

Figure 6.8 shows the normalized tangential stress by internal pressure with respect to the angle around the borehole wall in transversely isotropic rock.

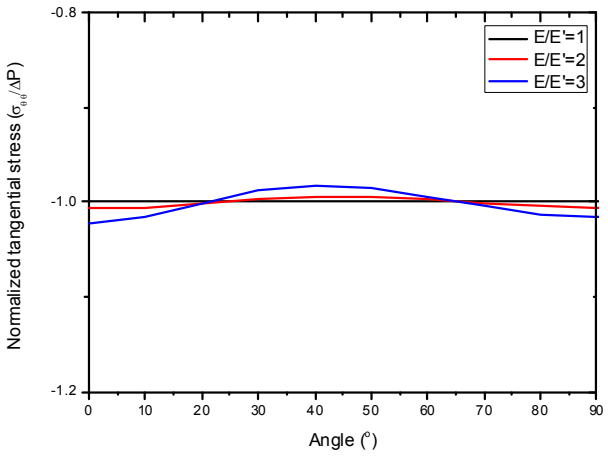

Figure 6.8 Normalized tangential stress by internal pressure

6.1.10. Effect of Poisson's ratio

The effect of Poisson's ratio (ν/ν') was studied by varying between 0.5 and 5 (Figure 6.9). One can conclude that the Poisson's ratio (ν/ν') does not have a great effect in the calculation of stress distribution around the borehole wall as shown in Fig.6.9.

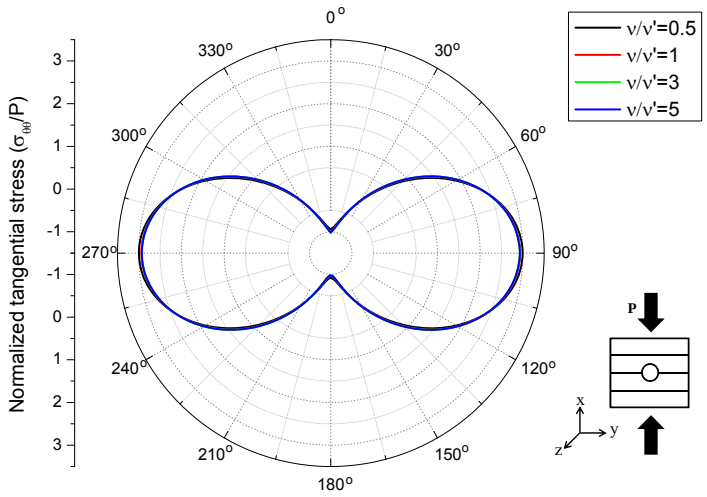

(a) Stress concentration for uniaxial condition (x-direction)

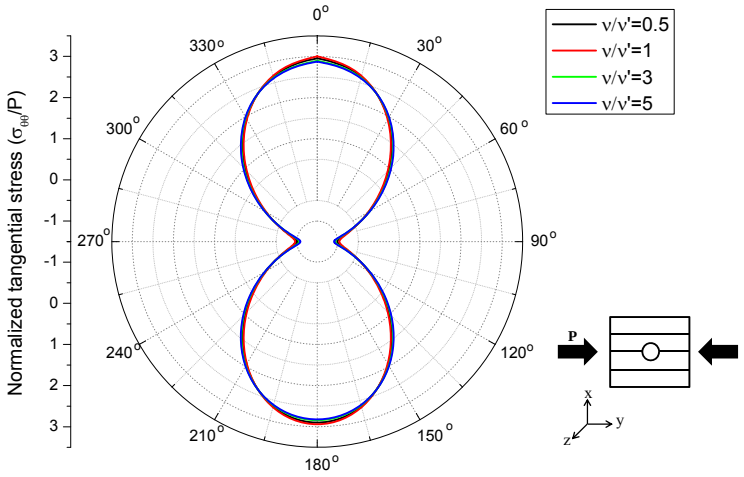

(b) Stress concentration for uniaxial condition (y-direction)

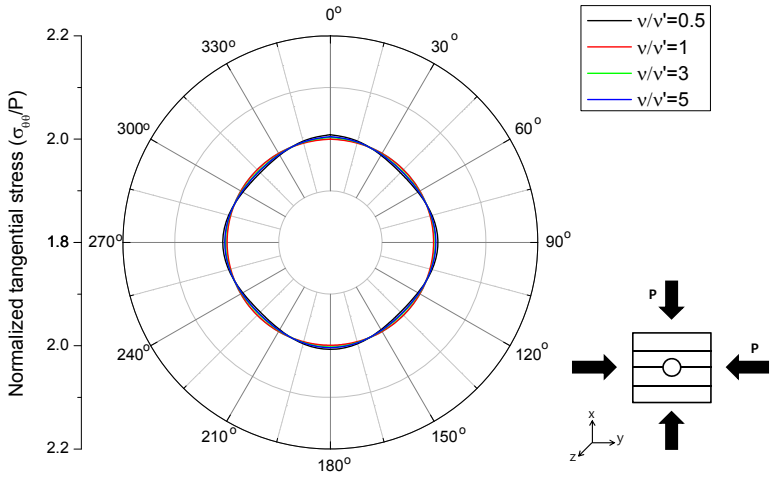

(c) Stress distribution around the borehole in uniform biaxial stress condition

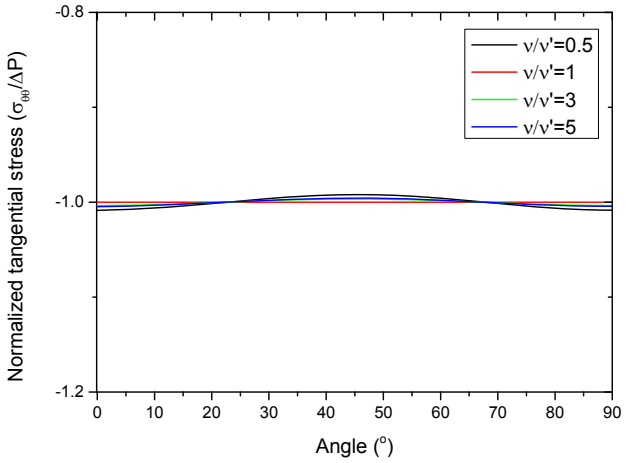

(d) Stress concentration by internal pressure

Figure 6.9 Stress distribution around borehole with respect to the Poisson's ratio (ν/ν') changes

6.1.11. Effect of shear modulus ratio

Several cases were run in order to evaluate the impact of the difference between G and G'. The anisotropy ratio (E/E') and Poisson's ratio (ν/ν') were kept equal to unity, the shear modulus G was computed from the relationship based on E and ν . The effect of shear modulus ratio was studied by varying the value of G'.

It has been stated in the literature that the shear modulus G' is not related to the another constants and it is most difficult to determine experimentally (Batugin and Nirenburg, 1972). Figure 6.10 shows the considerable differences of stress distribution around the borehole with respect to the shear modulus ratio (G/G'). The shear modulus ratio can be critical factor in borehole stability analysis.

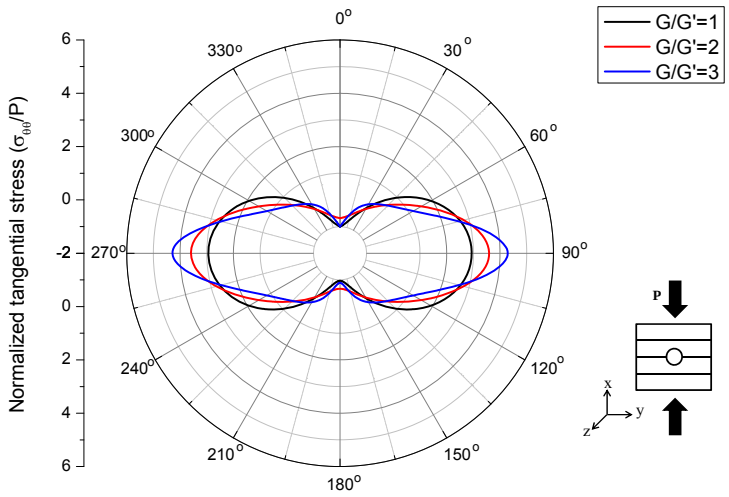

(a) Stress concentration for uniaxial condition (x-direction)

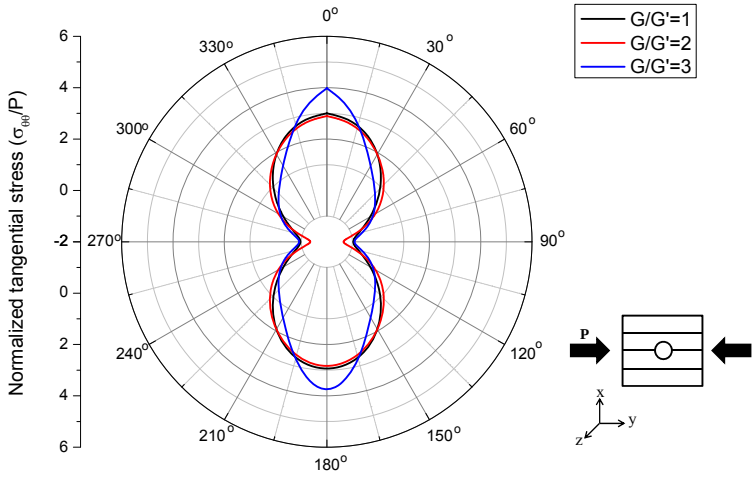

(b) Stress concentration for uniaxial condition (y-direction)

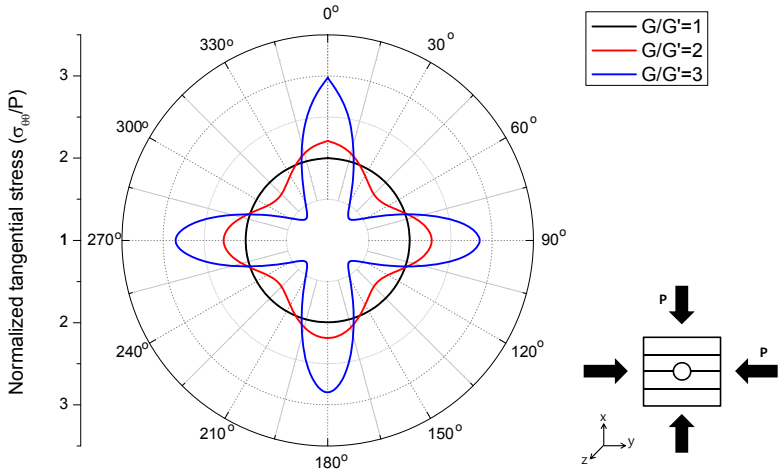

(c) Stress distribution around the borehole in uniform biaxial stress condition

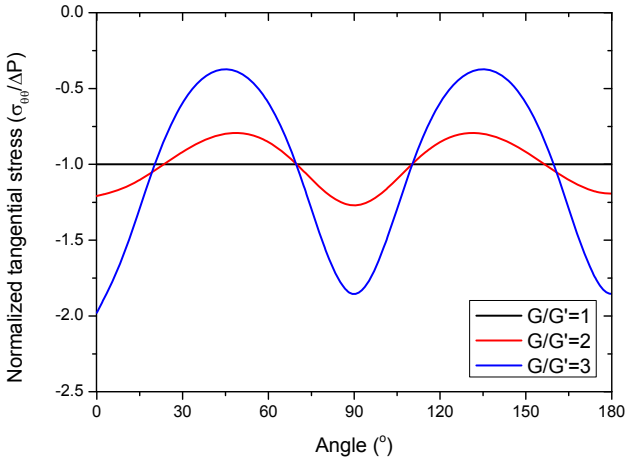

(d) Stress concentration by internal pressure

Figure 6.10 Stress distribution around borehole with respect to the shear modulus ratio (G/G')

6.1.12. Plane strain and plane stress problem

Until last section, the solution of the problem is based on the plane strain problem. This is possible when the dimension of the anisotropic body is very large in the longitudinal direction of the hole, approximately infinite. Usually the distance equal to two or three times the hole diameter seems reasonable. Plane strain formulations are frequently used in rock mechanics when dealing with underground structures or stress measurements in boreholes (Amadei, 1982).

When the dimensions of the anisotropic body are large in two direction only, this is referred to as plane stress problem. In the usual plane stress formulation, the body is assumed to be analogous to a thin plate. Plans stress problem is similar with plane strain problem, the only difference being that all the coefficients β_{ij} in Eq. (6.10) are replaced by the coefficients a_{ij}. The generalized plane stress formulation was extended by Lekhnitskii (1963) to anisotropic plates with one plane of elastic symmetry parallel to their middle plane. No solution exists for any inclined anisotropy (Amadei, 1982).

6.2. Stress distribution around a borehole – numerical study

Previous studies (Amadei, 1982; Lekhnitskii, 1963) analyzed the stress concentration and suggested the analytic solution (section 6.1) around the borehole wall.

In isotropic rock, it is easy and simple to explain the stress distribution at any point within the elastic domain as well as at the borehole wall using Kirsch equations. But the analytic solution for anisotropic rock is much more complex and most of borehole stability analyses in anisotropic rock focus on the failure of the borehole wall. Therefore there is little study to analyze the stress distribution across the domain.

The object of this study is not only to analyze the borehole stability but also to compare the stress distribution in anisotropic rock with that in isotropic rock. For this purpose, numerical study using COMSOL Multiphysics was adopted to analyze the stress distribution along the domain in transversely isotropic rock.

The same model in section 5.2 was used for comparative analysis with isotropic case and in order to mimic the borehole deviation by applying appropriate stress boundary conditions on the surface of the block. This can

be achieved by computing the components of the rotated stress tensor(Gaede et al., 2012).

Parameters used in numerical study are from the value of Boryeong shale (Table 4.1 in Section 4.1).

Table 6.1 Parameters used to analyze the stress distribution in transversely anisotropic rock

E	39.3 GPa
E′	19 GPa
ν	0.18
ν′	0.2
G′	8.7 GPa

The boundary condition for vertical borehole and horizontal borehole in transversely isotropic rock was given in Figure 6.11. Those are extrapolated value at 3000 m depth based on data at Pohang (Chang et al., 2010).

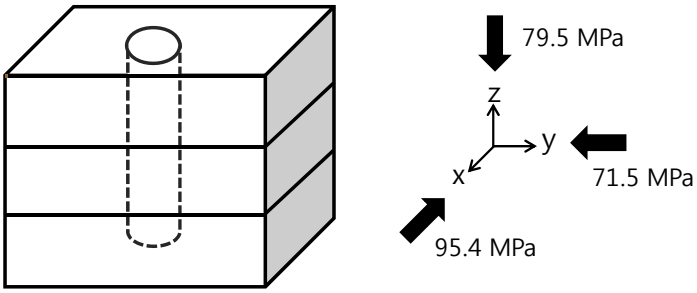

(a) Vertical hole in transversely isotropic rock

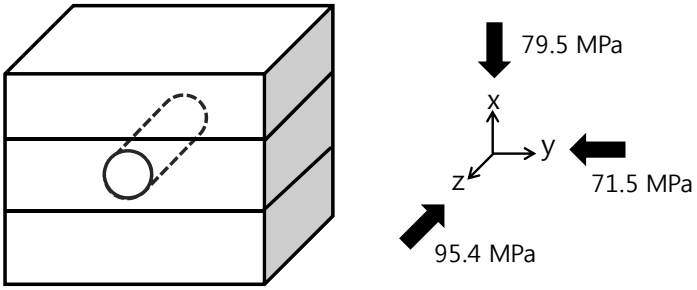

(b) Horizontal hole in transversely isotropic rock

Figure 6.11 The boundary condition for vertical borehole and horizontal borehole in transversely isotropic rock

Figure 6.12 shows the variations of the tangential stress ($\sigma_{\theta\theta}$) and radial stress (σ_{rr}) around the vertical and horizontal holes. The contours of tangential stress ($\sigma_{\theta\theta}$) and radial stress (σ_{rr}) vary across x-y domain.

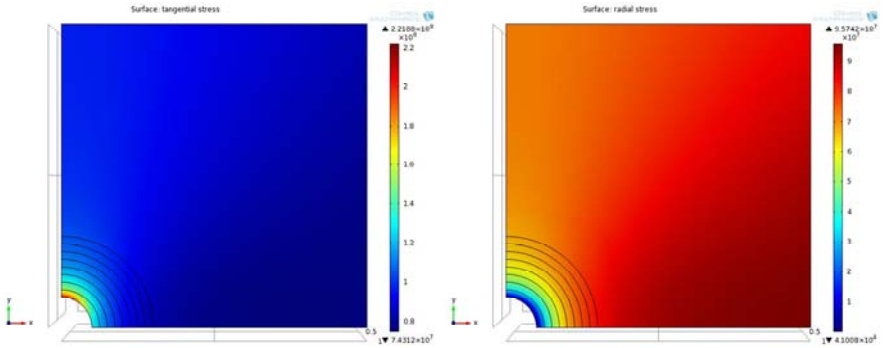

(a) Vertical borehole

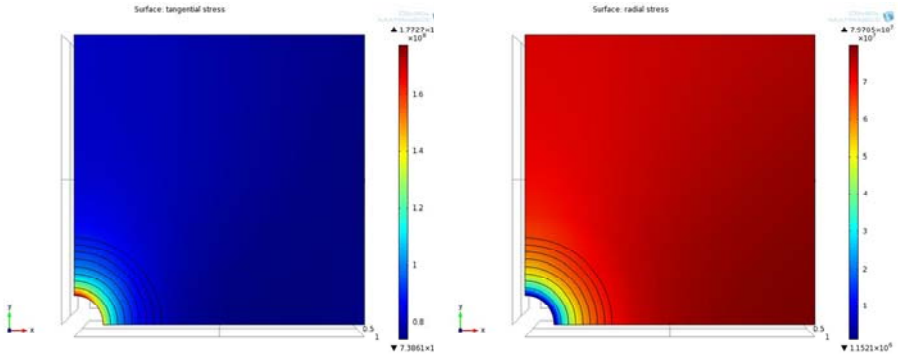

(b) Horizontal borehole

Figure 6.12 the variations of the tangential stress ($\sigma_{\theta\theta}$) and radial stress (σ_{rr}) around the vertical and horizontal hole (unit: Pa)

Figure 6.13 shows the comparison between numerical and analytical solutions for the stress distribution around the borehole in transversely isotropic rock. It has been stated by Ong that for transversely isotropic

medium with the plane of isotropy perpendicular to the hole axis, no solution can be found (Ong, 1994). But recently, Gaede(2012) showed that analytic solution of Lekhnitskii and Amadei actually works for any symmetry. Actually the degeneration of analytic solution was not observed as described by Ong. The numerical result and analytic solution match well. Also, there is no significant difference between anisotropic case (Figure 6.13) and isotropic case except 0° and 90°. The degree of anisotropy of Boryeong Shale is about 2. As was mentioned previously, the degree of anisotropy below 2 does not substantial affect the overall stress concentration except loading direction.

The stress distribution along the x and y direction is shown in Figure 6.14 and Figure 6.15 and these results are compared with the isotropic case. The general trend of stress distribution is similar. But starting point of tangential stress ($\sigma_{\theta\theta}$) is different because of stress concentration at the borehole wall. Radial stress is identical since there is no internal pressure.

Stress distribution of vertical borehole is more similar with isotropic case. It is considered that the location around the vertical hole is less affected by anisotropy.

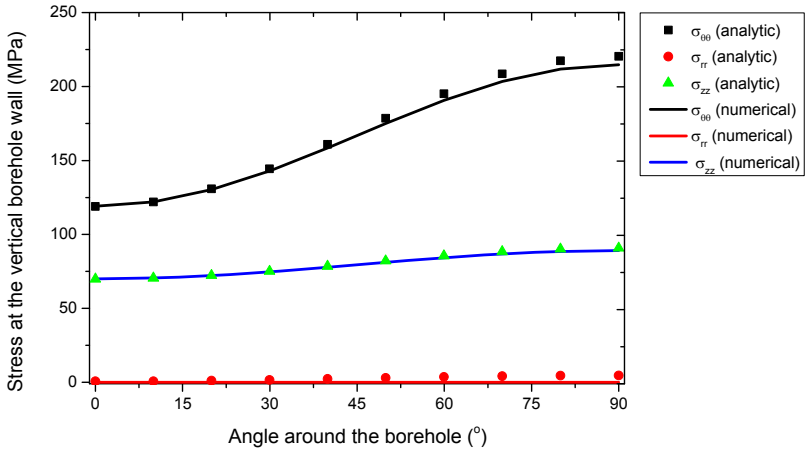

(a) Vertical borehole

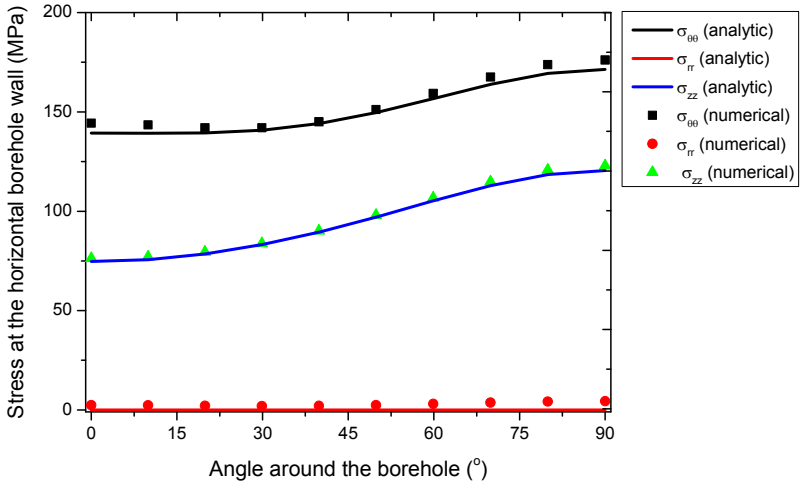

(b) Horizontal borehole

Figure 6.13 Stress distribution around the borehole in transversely isotropic rock

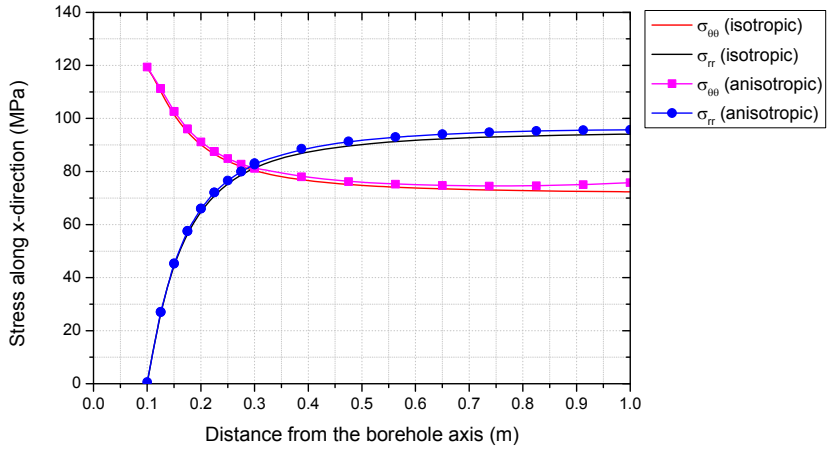

(a) Vertical borehole

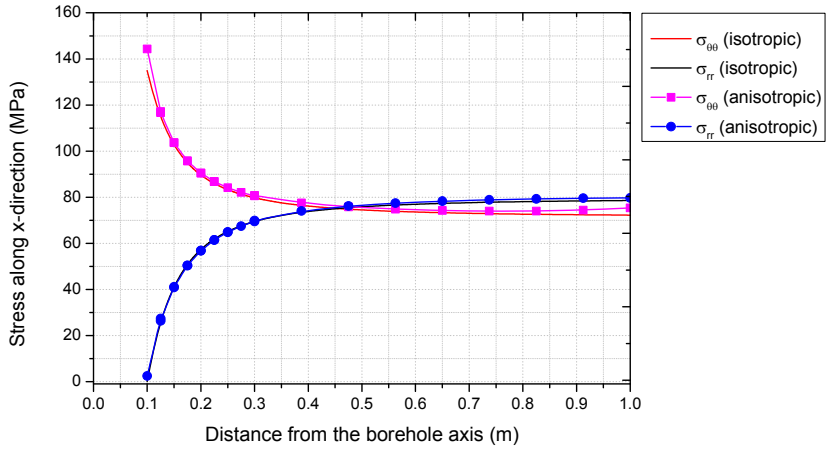

(b) Horizontal borehole

Figure 6.14 Stress distribution along the x-direction in vertical and horizontal borehole

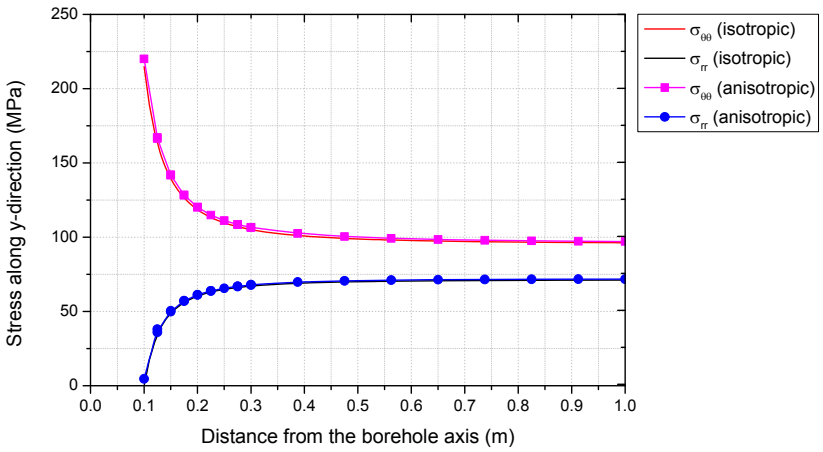

(a) Vertical borehole

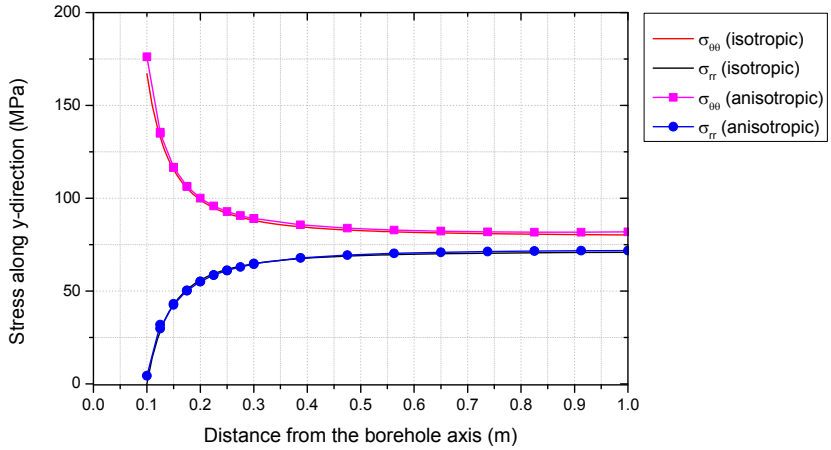

(b) Horizontal borehole

Figure 6.15 Stress distribution along the y-direction in vertical and horizontal borehole

The degree of anisotropy of Boryeong Shale is about 2. This value is not large enough to show the significant effect of anisotropy on the stress distribution along the domain. In order to analyze the effect of anisotropy, several cases of horizontal borehole were compared. Figure 6.16 shows the clear difference with respect to the degree of anisotropy. There is a significant difference of tangential stress ($\sigma_{\theta\theta}$) at the borehole wall because of stress concentration depending on the degree of anisotropy. As the distance is far from the borehole axis, both tangential stress and radial stress are converged to the values equal to boundary condition.

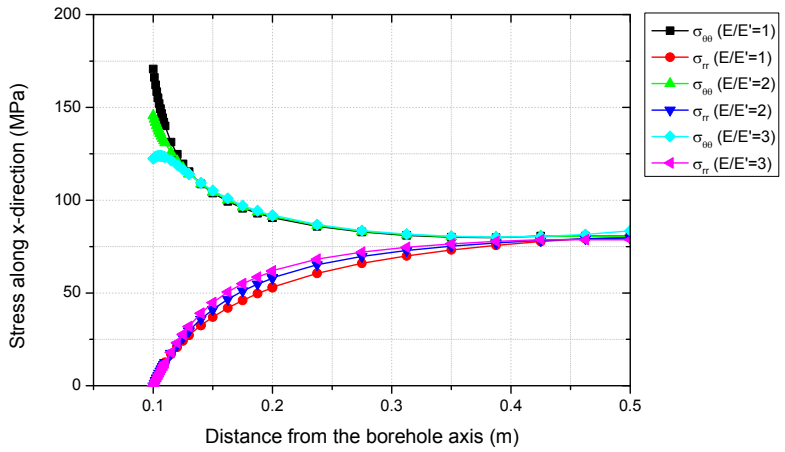

(a) Comparison of stress distribution along x-direction

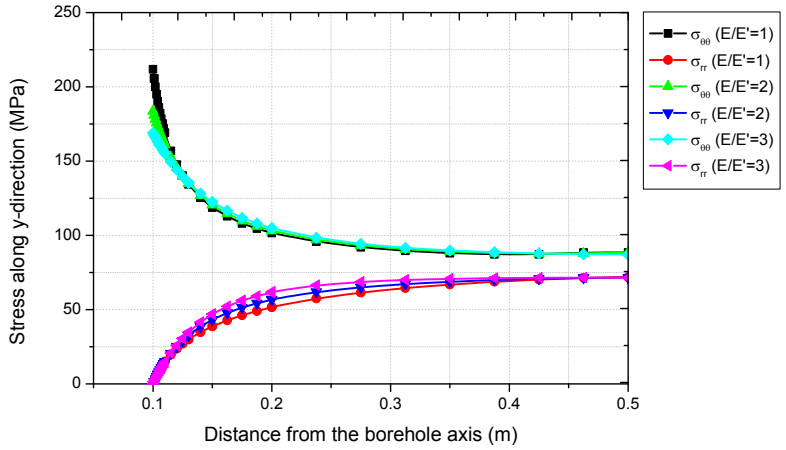

(b) Comparison of stress distribution along y-direction

Figure 6.16 Stress distribution along the domain with respect to degree of anisotropy

6.3. Stress distribution around inclined borehole

In section 6.1 and 6.2, only the case of vertical borehole and horizontal borehole were considered. But, in general, inclined borehole has been widely drilled and the borehole instability can become a major concern. Instability problems have been reported more frequently when the inclinations increase (Ong and Roegiers, 1993).

The analytic approach of Lekhnitskii (1963) and Amadei (1982) was applied to analyze the stress distribution around the inclined borehole with respect to the inclination. In this study, the inclination angle indicates α_D in Figure 6.1 and the angle α_A is fixed as zero. Parameters are from the value of Boryeong shale (Table 4.1 in Section 4.1) and the boundary condition is identical to the previous section 6.2, in 3000m depth of Pohang (Figure 6.17).

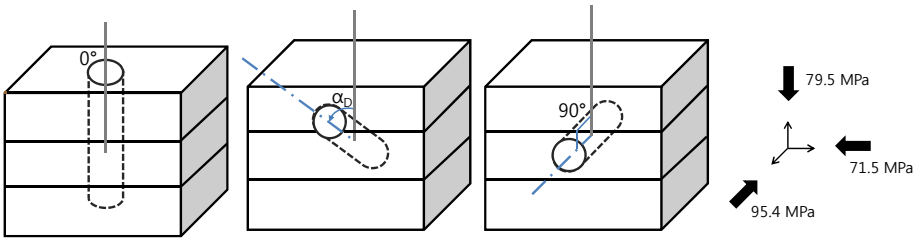

(a) Vertical borehole (α_D = 0°) (b) Inclined borehole (0° < α_D < 90°) (c) Horizontal borehole (α_D = 90°)

Figure 6.17 Boundary condition for inclined borehole in transversely isotropic rock

Figure 6.18 shows the stress distribution around the borehole for increasing the inclination, α_D. When the borehole is rotated from a vertical borehole (α_D = 0°) to a horizontal position (α_D = 90°), the analysis shows that the stress distribution is quite different from vertical position one. It is considered that the changed stress boundary condition by rotating axis affects the stress distribution. Also, the stress distribution can be affected by anisotropy ratio (E/E′) as well as stress boundary condition.

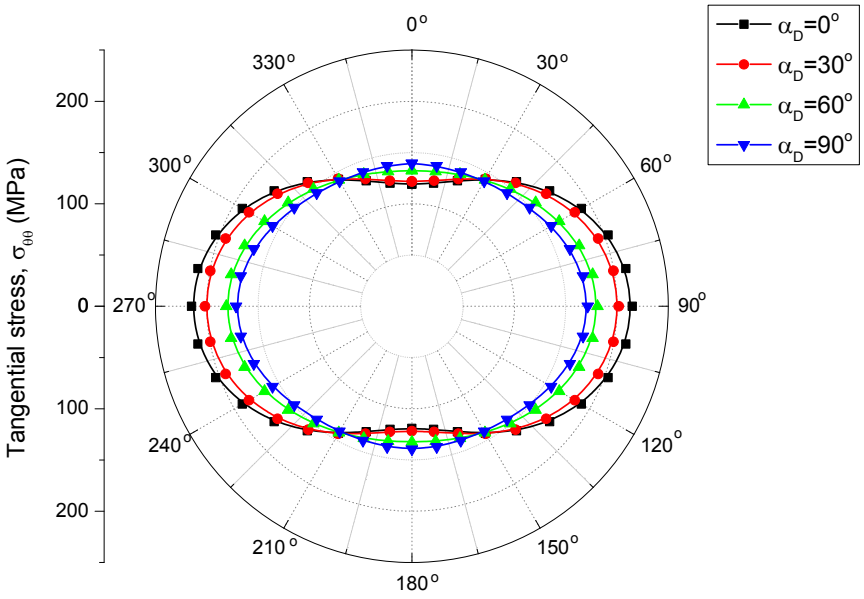

Figure 6.18 Stress distribution around the borehole wall with the change of the inclination, α_D

The case of low inclination angle (α_D = 30°) is similar with isotropic case.

But for the quite highly inclined borehole ($\alpha_D = 60°$), the stress distribution is distinguished from isotropic case (E/E′) (Figure 6.19). This result is identical with the results by Ong (1993), which reported that the influence of anisotropy on the stability of the borehole becomes critical when the inclination of the borehole are high.

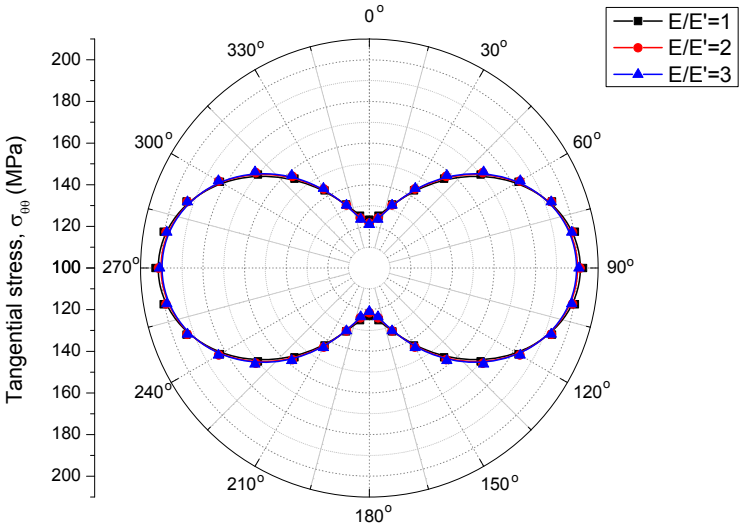

(a) $\alpha_D = 30°$ inclination borehole

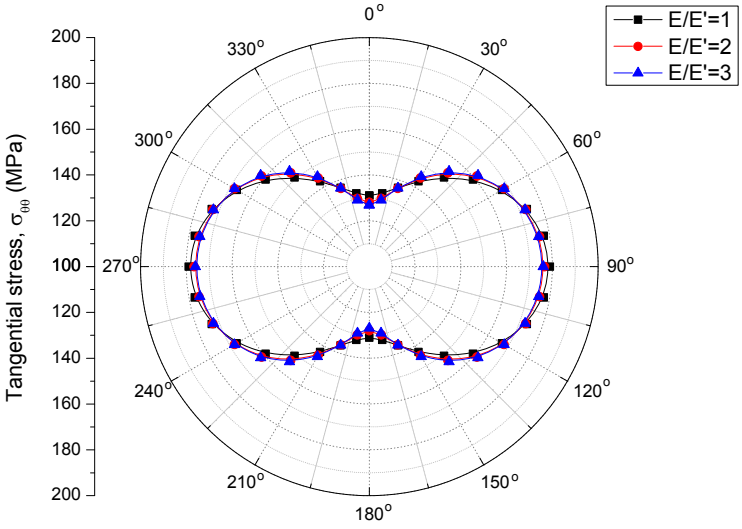

(b) $\alpha_D = 60°$ inclination borehole

Figure 6.19 Variation of tangential stress around inclined borehole

6.4. Borehole breakout

6.4.1. Strength anisotropy in transversely isotropic rock

Many experimental results show that most sedimentary and metamorphic rocks display a strong anisotropy of strength (Donath, 1961; McLamore and Gray, 1967; Ramamurthy, 1993). In this study, three types of rock showed clear strength anisotropy in uniaxial compressive strength and tensile strength test (Section 3.2). These types of rocks usually exhibit some preferred orientation of fabric or possess distinct bedding planes, which results in transversely isotropic behavior on the macro-scale (Lee and Pietruszczak, 2008).

Although many attempts have been made to describe the strength anisotropy of transversely isotropic rocks, no general methodology has emerged yet. Jaeger(1960) suggested the single weakness plane theory with two strength model, but this provided an oversimplified representation of strength variation in anisotropic rocks (Brady and Brown, 2004). And it is suitable for cases in which a single well defined discontinuity is present in a rock sample, and this does not adequately describe the behavior of naturally occurring anisotropic rocks (Hoek and Brown, 1990). McLamore and Gray (1967) also

proposed some equations but these were empirical ones. Hoek and Brown assumed that the strength parameters m and s in their well-known failure criterion are not constant but variable depending on the direction of weakness plane. However, although the values of m and s are selected based on the orientation of joints, it should be noted that the formulation still remain isotropic, so that it is doubtful whether the orientation of failure plane predicted by this approach is realistic (Lee and Pietruszczak, 2008).

In order to describe the strength characteristics of geological materials critical plane approach has been proposed (Pietruszczak and Mroz, 2001). This method searches for a direction of failure plane that the value of failure function reaches maximum. some study analyze anisotropic behavior or sedimentary rocks (Pietruszczak et al., 2002), structural masonry (Ushaksaraei and Pietruszczak, 2002), and transversely isotropic rock mass (Lee and Pietruszczak, 2008) using this methodology.

6.4.2. Mohr-Coulomb anisotropic failure criterion for transversely isotropic rock

The critical plane approach is applied to describe the anisotropic Mohr-Coulomb failure criterion in this study. A detailed methodology about the critical plane approach for anisotropic Mohr-Coulomb failure criterion is

presented in Pietruszcsak (Pietruszczak and Mroz, 2001) and Lee (Lee and Pietruszczak, 2008).

According to Lee and Pietruszczak (2008), a concept of fabric tensor is adopted to define the cohesion and friction angle in transversely isotropic rock. It is assumed that the parameters c (cohesion) and ϕ (friction angle) can be defined in terms of the following distribution functions on a plane having the unit normal n (Lee and Choi, 2011) ,

$$c = c_0\left(1+\Omega_{ij}^{c} n_j n_i\right)$$
$$\phi = \phi_0\left(1+\Omega_{ij}^{\phi} n_j n_i\right) \tag{6.13}$$

where c_0 and ϕ_0 is the orientation average of cohesion and friction angle, and Ω_{ij} is a traceless symmetric tensor describing the bias in the spatial distribution of c and ϕ with respect to the mean value.

It should be noted that for an isotropic material the Ω_{ij} vanish, so that c and ϕ become constant.

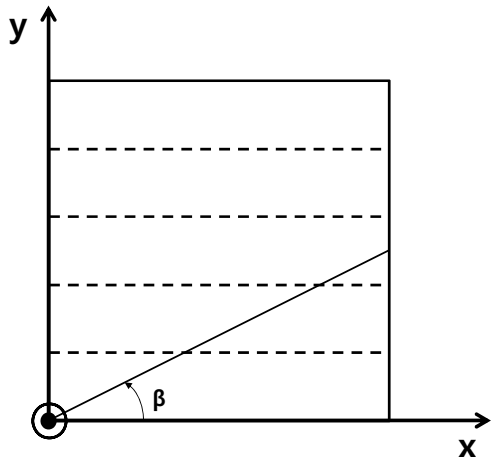

Figure 6.20 Local coordinate system (modified from (Lee and Choi, 2011)

In the case of transversely isotropic rock, the fabric tensor Ω_{ij} in local coordinate system (Figure 6.20) can be represented as following (Lee and Choi, 2011):

$$\Omega_{ij} = \begin{bmatrix} \Omega_0 & 0 & 0 \\ 0 & -2\Omega_0 & 0 \\ 0 & 0 & \Omega_0 \end{bmatrix}$$

So it simplifies to

$$\begin{aligned} c &= c_0 \left(1 + \Omega_0{}^{c} \left(1 - 3\cos^2 \beta\right)\right) \\ \phi &= \phi_0 \left(1 + \Omega_0{}^{\phi} \left(1 - 3\cos^2 \beta\right)\right) \end{aligned} \tag{6.14}$$

Eq. (6.14) indicates the cohesion and internal friction angle on a plane that makes an angle β with the x-direction.

Figure 6.21 shows the spatial variation of cohesion in a transversely

isotropic rock depending on the Ω_0^c when c_0=30MPa. As Ω_0^c increases, the anisotropy of cohesion also increases. On a plane parallel to the weakness plane, i.e., β=0° the cohesion has minimum value and the cohesion is maximum in the opposite case (β=90°).

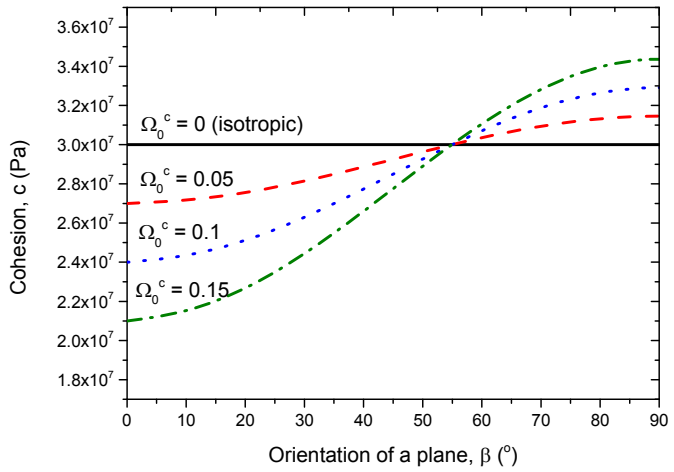

Figure 6.21 Spatial variation of cohesion in a transversely isotropic rock (modified from (Lee and Choi, 2011))

The internal friction angle has similar trend according to the orientation of a plane, β.

The anisotropy in these two strength parameters, c and ϕ, can be calculated considering the relative rotation between the principal stress coordinate and the principal material triad through the numerical triaxial test(Lee and Pietruszczak, 2008; Pietruszczak and Mroz, 2001).

6.4.3. Numerical simulation of triaxial test

Because the triaxial compressive test for transversely isotropic rock was not conducted in this study, the triaxial compressive test data of Green River Shale from McLamore(1967) was applied to suggest an anisotropic Mohr-Coulomb failure criterion considering strength anisotropy. The parameters c_0, ϕ_0, Ω_0^c, Ω_0^ϕ of the proposed failure criterion was determined through the simulation of conventional triaxial compression test and the numerical results were compared with actual experimental results (McLamore and Gray, 1967).

The numerical simulations were depicted in Figure 6.22. The angle γ denotes the angle between the bedding plane and σ_1 direction.

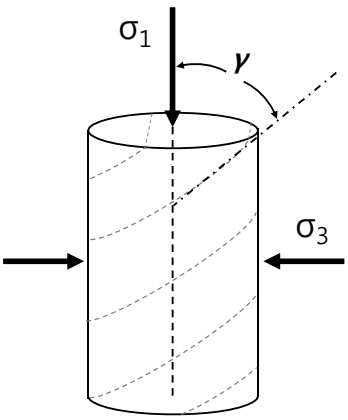

Figure 6.22 Geometry of the sample for the simulation of triaxial compression test

The cohesion (c) and internal friction angle (ϕ) were calculated considering the relative rotation between the principal stress coordinate and the principal material triad.

In principal coordinate system, the normal and shear stresses on a plane whose outward unit normal vector is rotated by φ from the first principal stress (σ_1) direction (Jaeger et al., 2007):

$$\sigma = \frac{(\sigma_1 + \sigma_3)}{2} + \frac{(\sigma_1 - \sigma_3)}{2}\cos 2\varphi$$
$$\tau = -\frac{(\sigma_1 - \sigma_3)}{2}\sin 2\varphi \qquad (6.15)$$

Substituting the parameters, c, ϕ, σ and τ into Mohr-Coulomb failure function, $F_{MC} = \tau - (\tan\phi)\sigma - c$, is checked to find the critical plane.

Five cases were considered corresponding to different confining pressures (σ_1), i.e., 7, 35, 70, 100 and 170MPa, and the results were compared with those reported by McLamore (McLamore and Gray, 1967). For each confining pressure, σ_1 was increased by small increments step to find the orientation of critical plane on which the failure criterion and failure function was maximized at each step to find the orientation of critical plane on which the failure criterion was subsequently checked. The value of major principal stress σ_1 at failure was examined as a function of γ, while $\sigma_2 = \sigma_3$ remained constant(Lee and Pietruszczak, 2008).

In Figure 6.23 solid lines indicate the actual triaxial experimental result and dotted lines indicate the numerical ones using anisotropic Mohr-Coulomb failure criterion used in this study.

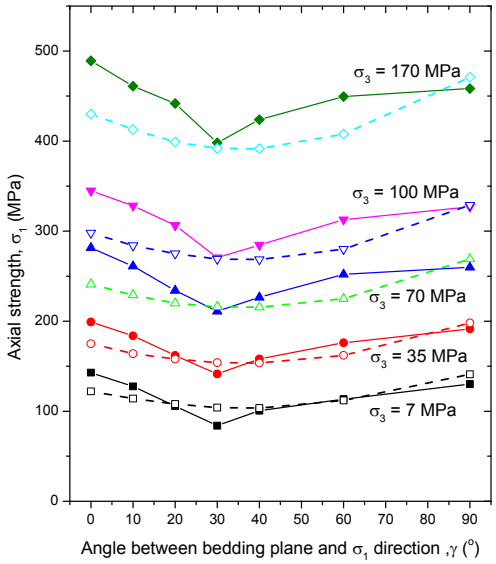

Figure 6.23 Simulation results of triaxial test for Green River Shale[33] with different inclinations of weak plane (c_0=45MPa, Ω_0^c= 0.12, ϕ_0=20°, Ω_0^ϕ=0.1)

This results of numerical simulations corresponds to c_0=45MPa, Ω_0^c= 0.12, ϕ_0=20°, Ω_0^ϕ=0.1. It shows the variation of axial strength with inclination of bedding plane for different confining pressure. For the strength prediction, the agreement between experimental and numerical values is acceptable, particularly within the range of $30° \leq \gamma \leq 90°$. The lowest strength is

obtained at $\gamma = 30°$. But there is a big discrepancy between the experimental and numerical results at $\gamma = 0°$. Especially, the value of $\gamma = 90°$ is smaller than $\gamma = 0°$ in experimental data, while the opposite trend is shown in numerical result. This experimental example of McLamore was introduced as a less frequent case by Lee (2008). Most frequently, rocks show the highest compressive strength in the direction perpendicular to weakness planes as pointed out (Kwasniewski, 1993; Lee and Pietruszczak, 2008). Although the trend of numerical result is not fitted very well to experimental one, the results reported by some study show the same trend(Lee and Pietruszczak, 2008). Thus, proposed anisotropic parameters are reasonable.

6.4.4. Application of anisotropic Mohr-Coulomb failure criterion to borehole stability

To demonstrate the performance of the anisotropic Mohr-Coulomb failure criterion, conventional triaxial tests on the samples having various inclinations of weakness plane were simulated and the resulting triaxial strength and dip angle of failure plane were discussed by Pietruszczak and Lee(Lee and Pietruszczak, 2008; Pietruszczak and Mroz, 2001). There is little research to apply the anisotropic Mohr-Coulomb failure criterion to borehole stability analysis.

In order to analyze the borehole stability considering strength anisotropy in transversely isotropic rock, two strength parameters in Mohr-Coulmb failure criterion, i.e., c and ϕ are calculated with consideration of the relative angle in local coordinate system.

In local coordinate system (Figure 6.24) normal and shear stresses acting on a plane whose outward unit normal vector is rotated counterclockwise from the x-direction by an angle θ (Jaeger et al., 2007):

$$\sigma = \frac{1}{2}\left(\sigma_{xx} + \sigma_{yy}\right) + \frac{1}{2}\left(\sigma_{xx} - \sigma_{yy}\right)\cos 2\theta + \tau_{xy}\sin 2\theta$$
$$\tau = -\frac{1}{2}\left(\sigma_{xx} - \sigma_{yy}\right)\sin 2\theta + \tau_{xy}\cos 2\theta \qquad (6.16)$$

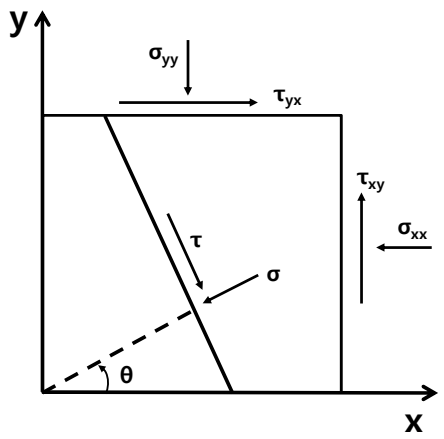

Figure 6.24 Normal and shear stresses acting on a plane in local coordinate system

In this local coordinate, because the angles θ (Figure 6.24) and β (Figure 6.20) have relationship of $\theta \pm 90° = \beta$, the anisotropic parameters c and ϕ in Eq. (6.14) can be transformed to

$$\begin{aligned} c &= c_0 \left(1 + \Omega_0{}^{c} \left(1 - 3\sin^2 \theta\right)\right) \\ \phi &= \phi_0 \left(1 + \Omega_0{}^{\phi} \left(1 - 3\sin^2 \theta\right)\right) \end{aligned} \tag{6.17}$$

(6.16) and (6.17) are substituted into following Mohr-Coulomb failure function in transversely isotropic rock:

$$F_{MC} = \tau - \left(\tan\phi\right)\sigma - c$$

A positive value of F_{MC} indicates that the failure occurs.

The possibility of failure for each point on borehole domain can be determined using this method.

6.4.5. Prediction of borehole breakout in transversely isotropic rock

There are some studies (Gupta and Zaman, 1999; Ong, 1994) to analyze the borehole stability in transversely isotropic rock concerning anisotropic behavior of the rock with more complex criterion. The Mohr-Coulomb

criterion has been widely applied to the problem of borehole shear failure. It is generally considered only applicable to materials which do not exhibit directional properties (Ong and Roegiers, 1993). But anisotropic Mohr-Coulomb criterion associated with critical plane approach in this study can be applied to predict the borehole failure in transversely isotropic rock.

First, a result of borehole breakout in isotropic rock using suggested anisotropic criterion was compared with the result of analytic method mentioned section 5.3. For isotropic rock, c and ϕ are independent of orientation, so that Ω_0^c and Ω_0^ϕ in Eq.(6.17) vanishes.

Each case of the vertical and horizontal hole is considered in this study and the boundary condition is identical with previous section.

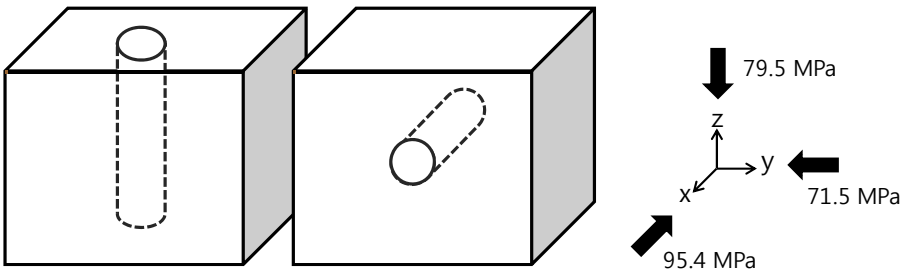

Figure 6.25 Boundary condition for borehole breakout in isotropic rock

First, the vertical borehole case with S_{Hmax} = 95.4 MPa, S_{hmin} = 71.5 MPa, c = 45MPa, ϕ = 30° and ΔP=0 is analyzed.

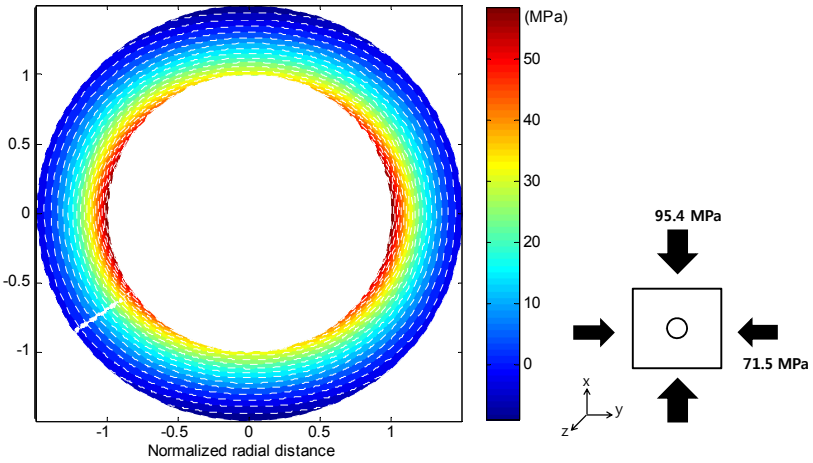

(a) Vertical borehole

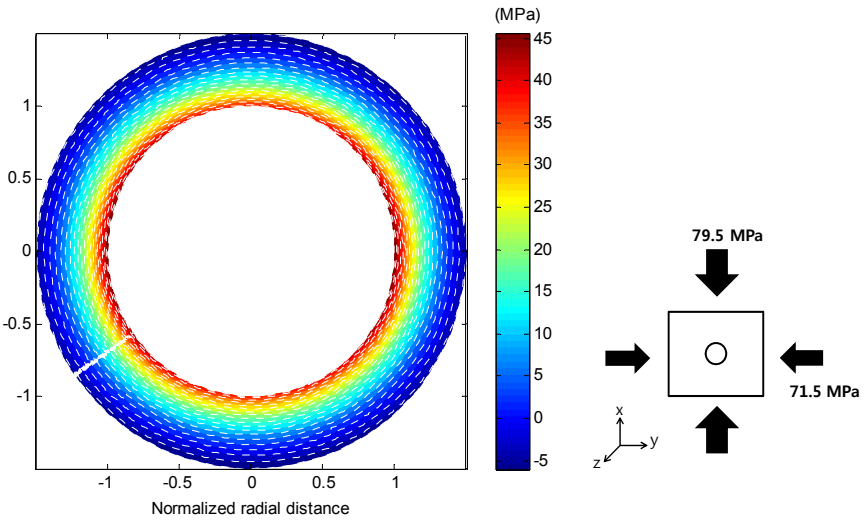

(b) Horizontal borehole

Figure 6.26 Borehole breakout in isotropic rock

Figure 6.26 shows the result of analytic method using Eq. (5.5). The colors in figure indicate the value of rock strength required to prevent failure. Thus, in vertical borehole the failure is expected within red-orange region (over 45 MPa) and the expected horizontal borehole breakout region is within red region (over 45 MPa). Both regions require the cohesive strength over 45 MPa to prevent the failure but each range is different. In isotropic case, the borehole breakout region is fully influenced by boundary condition.

The result of borehole breakout using suggested anisotropic criterion is given in Figure 6.27. For isotropic rock, this anisotropic criterion is independent of orientation and Mohr-Coulomb criterion with constant c and ϕ is used for the analysis. Both results are same although the former (Figure 6.26) is denser than the latter (Figure 6.27). As more data is used in calculation, the result is appeared more similar.

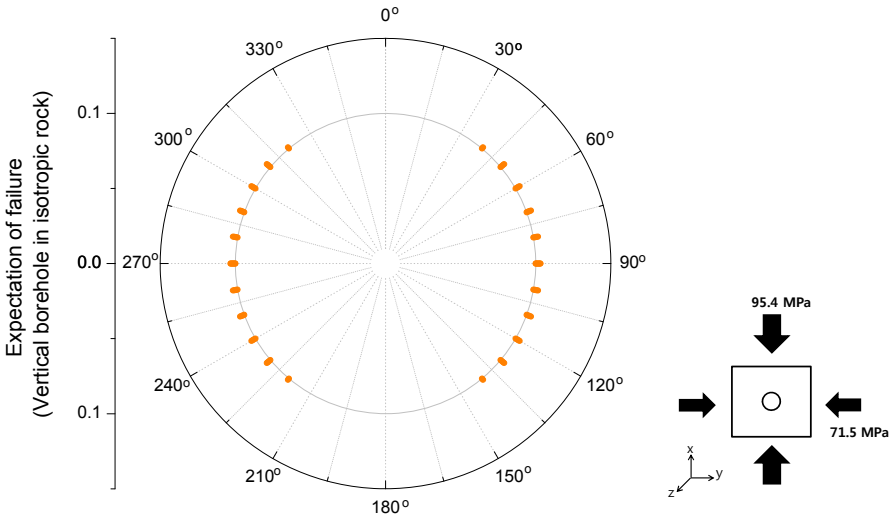

(a) Vertical borehole

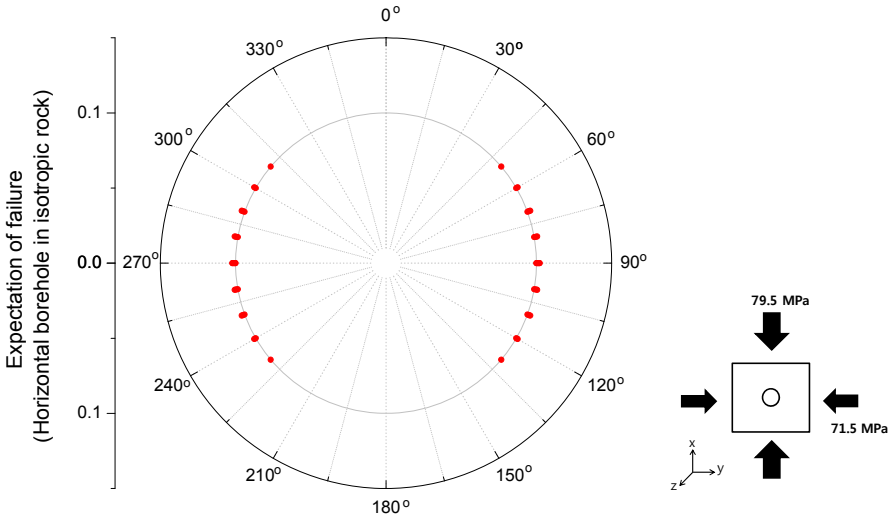

(b) Horizontal borehole

Figure 6.27 Borehole breakout in isotropic rock using suggested anisotropic criterion

The applied boundary conditions are restricted to strike-slip stress regime ($S_{Hmax} > S_v > S_{hmin}$) of 3000m depth of Pohang region. And there is no significant difference in each boundary stress. In order to examine the difference of borehole breakout range with respect to the boundary condition, failure analysis in transversely isotropic rock was carried out in various cases with new boundary conditions (Figure 6.28). Those boundary condition are calculated values based on Pohang and the ratio of S_{Hmax} to S_{hmin} is 4:3 (Chang et al., 2010). The range of stress ratio (K), which is a ratio of the horizontal principal stress to the vertical principal stress, is assumed to vary from 0.5 to 2. The vertical stress component is regarded as overburden weight.

The case of K=0.5 represents the normal stress regime ($S_V > S_{Hmax} > S_{hmin}$), the case of K=1 is the strike-slip stress regime ($S_{Hmax} > S_v > S_{hmin}$) and the case of K=2 is thrust stress regime ($S_{Hmax} > S_{hmin} > S_V$).

Elastic constants of Boryeong Shale (Cho et al., 2012) and anisotropic parameters of Green River Shale (McLamore and Gray, 1967) were used (Table 6.2). And numerical study using COMSOL was conducted in order to determine the stress states around a borehole domain as well as at borehole wall. Figure 6.32 is the borehole breakout analysis result according to the stress regime.

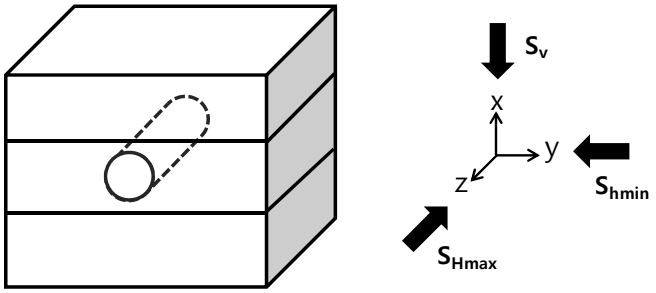

Depth	S_v (MPa)	K=0.5		K=1		K=2	
		S_{Hmax} (MPa)	S_{hmin} (MPa)	S_{Hmax} (MPa)	S_{hmin} (MPa)	S_{Hmax} (MPa)	S_{hmin} (MPa)
1000m	26.5	Case 1		Case 2		Case 3	
		11	16	23	30	46	60
3000m	79.5	Case 4		Case 5		Case 6	
		34	45.5	68	91	136	182
5000m	132.5	Case 7		Case 8		Case 9	
		57	75.5	114	151	227	303

Figure 6.28 Boundary conditions for failure analysis in transversely isotropic rock

Table 6.2 Parameters used to predict borehole breakout

E	39.3 GPa	Boryeong Shale (Cho et al., 2012)
E′	19 GPa	
ν	0.18	
ν′	0.2	
G′	8.7 GPa	
c_0	45MPa	Green River Shale (McLamore and Gray, 1967)
ϕ_0	20°	
Ω_0^c	0.12	
Ω_0^ϕ	0.1	

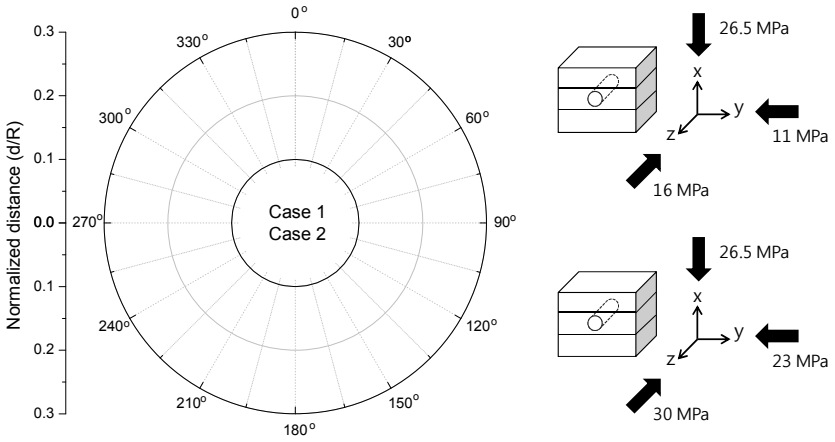

(a) Case 1 (1000m depth, K=0.5) and Case 2 (1000m depth, K=1) : No breakout

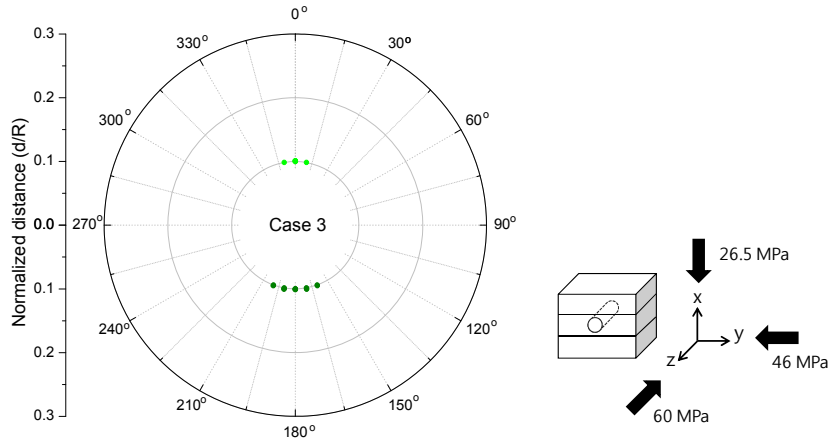

(b) Case 3 (1000m depth, K=2) : Borehole breakout without considering strength anisotropy(top) and with considering strength anisotropy (bottom)

Figure 6.29 Borehole breakout analysis result according to the stress regime (Continued)

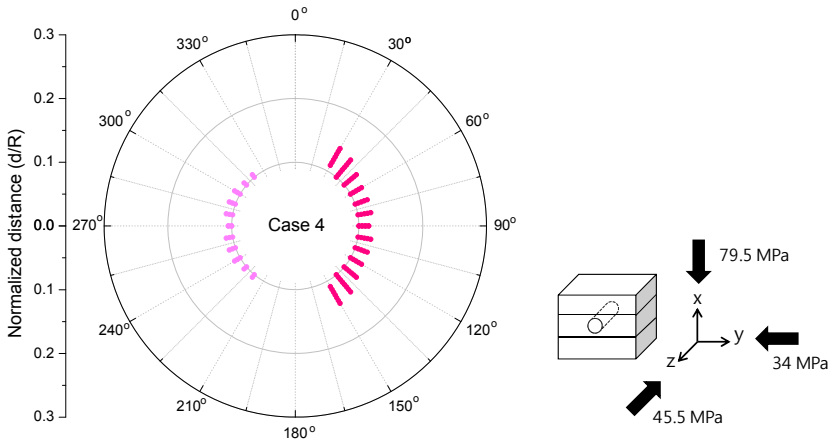

(c) Case 4 (3000m depth, K=0.5) : Borehole breakout without considering strength anisotropy(left) and with considering strength anisotropy (right)

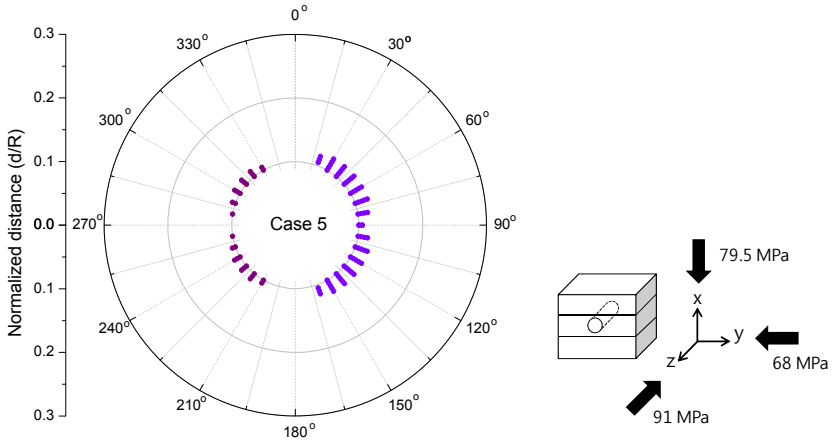

(d) Case 5 (3000m depth, K=1) : Borehole breakout without considering strength anisotropy(left) and with considering strength anisotropy (right)

Figure 6.30 Borehole breakout analysis result according to the stress regime (Continued)

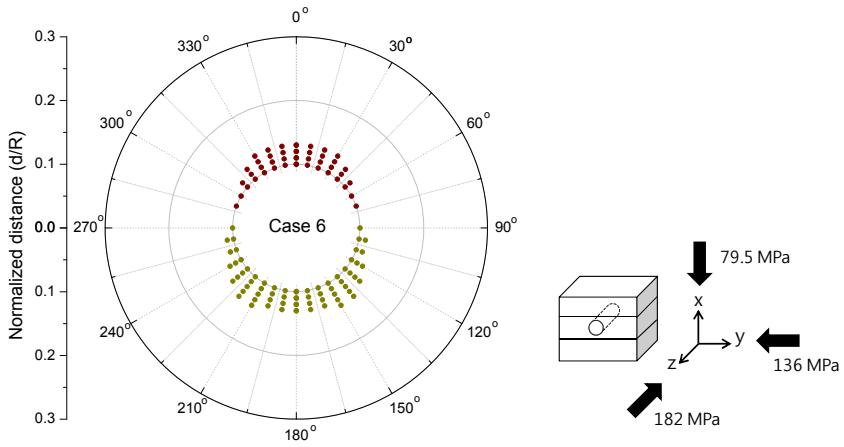

(e) Case 6 (3000m depth, K=2) : Borehole breakout without considering strength anisotropy(top) and with considering strength anisotropy (bottom)

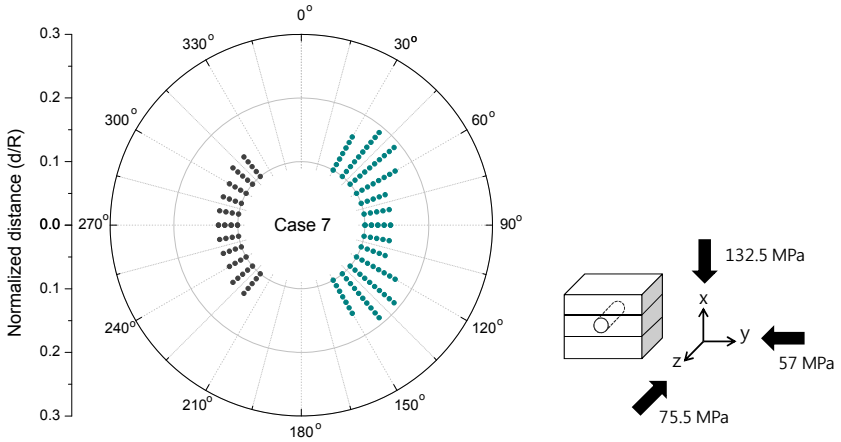

(f) Case 7 (5000m depth, K=0.5) : Borehole breakout without considering strength anisotropy(left) and with considering strength anisotropy (right)

Figure 6.31 Borehole breakout analysis result according to the stress regime (Continued)

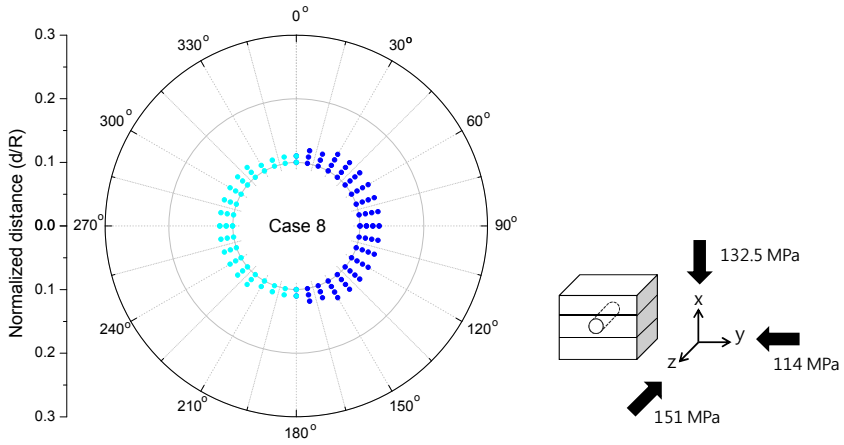

(g) Case 8 (5000m depth, K=1) : Borehole breakout without considering strength anisotropy(left) and with considering strength anisotropy (right)

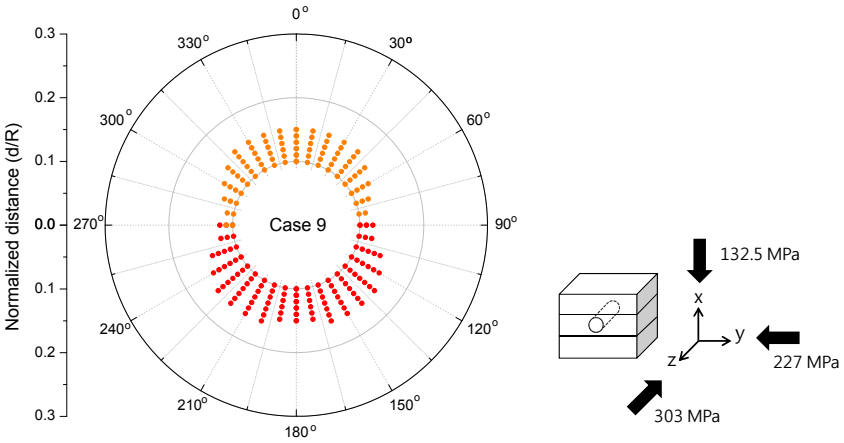

(h) Case 9 (5000m depth, K=2) : Borehole breakout without considering strength anisotropy(top) and with considering strength anisotropy (bottom)

Figure 6.32 Borehole breakout analysis result according to the stress regime

Figure 6.32 shows the region that borehole breakout is expected when the suggested anisotropic criterion considering strength anisotropy is applied (top or left) and strength anisotropy is not considered (bottom or right), i.e., isotropic failure criteria is applied (Ω_0^c and Ω_0^ϕ are zero).

In 1000m depth, when the normal (Case 1) and strike-slip stress regime (Case 2) is applied, there is no borehole breakout Figure 6.32 (a). But in the thrust stress regime (Case 3) boundary condition, the narrow borehole breakout region appears. It seems that the borehole breakout is difficult to occur. under the given condition

In 3000m and 5000m depth, the borehole breakout appears in all of the stress regime cases (Figure 6.32 (c), (d), (e), (f), (g), (h)). But the shape of breakout is different case by case. The broad and flat breakout appears around the borehole wall in strike-slip (Case 5, 8) and thrust stress regime (Case 6, 9). But the shape of breakout changes in the normal stress regime (Case 4, 7). These breakout models have steeper edge in flank, the difference of boundary condition can be a reason for that. The ratio of applied boundary condition around the borehole, i.e., the ratio of x-direction stress and y-direction stress is different. In normal (Case 1, 4, 7), strike-slip (Case 2, 5, 8) and thrust stress regime (Case 3, 6, 9) each ratio is 2.3, 1.2, and 0.6. when the maximum stress direction is perpendicular to the isotropic plane and the

ratio is bigger, the change of borehole breakout shape appears.

Generally, the range of breakout considering the strength anisotropy is wider and thicker than that without considering.

The main reason is the difference of failure criteria. When the anisotropic failure criterion considering strength anisotropy is applied, the possibility of failure increases. There are a lot of failure line depending on cohesion and internal friction angle in transversely isotropic case (Figure 6.30 (a)). It depends on the orientation of weakness plane. But in isotropic case there is one medium-valued failure line (Figure 6.30 (b)). The cohesion and internal friction angle of this single failure line coincides with the values on a plane that makes an angle about 55° with the x-direction in transversely isotropic case; at β=55° in Figure 6.21.

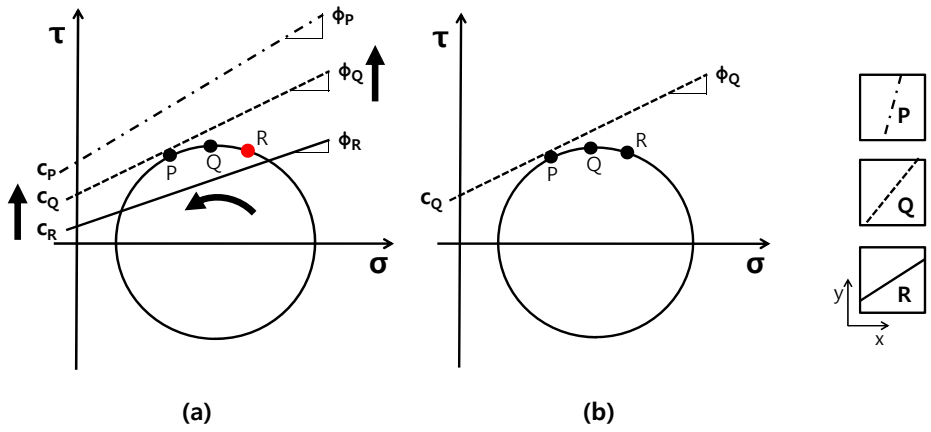

Figure 6.33 Mohr-coulomb failure criterion in (a) transversely isotropic rock and (b) isotropic rock

As shown in Figure 6.30, the fact that whether the failure occurs or not depends on the failure criterion. While one failure line is applied to all points of Mohr circle in isotropic case, each failure line is applied to each point of Mohr circle in anisotropic case to determine the failure. For this reason, in the point of R of Figure 6.30, the failure can occur when the anisotropic failure criterion is applied.

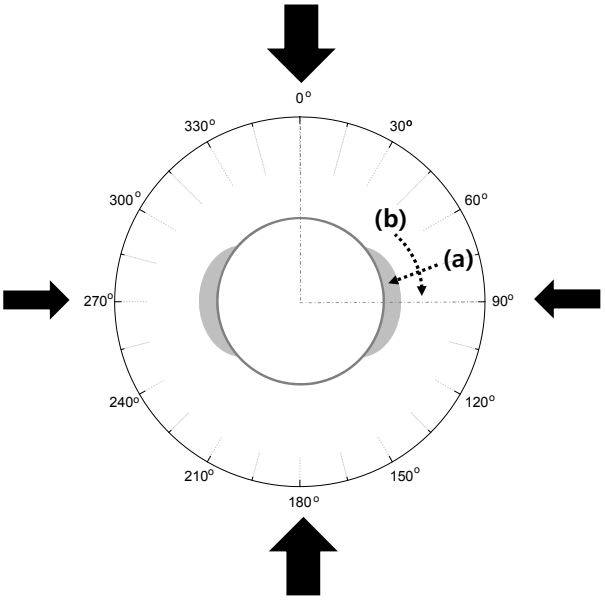

Figure 6.34 Shape of borehole breakout

Although the size of borehole breakout in isotropic rock and transversely isotropic rock is different, the shape of breakout is similar.

The failure region becomes wider as the distance from borehole wall

decreases (Figure 6.34). The location of the borehole breakout is affected by the magnitude of the maximum principal stress (σ_1). As σ_1 goes up and corresponding Mohr circle is bigger, the possibility of failure increases. As the maximum principal stress increases from σ_1 to σ_1* (Figure 6.35 (a)), the failure occurs in the point over the failure line (Figure 6.35 (b)). Also the borehole breakout region becomes thicker as the location is closer to the minimum pressure direction (Figure 6.34(b)) for the same reason.

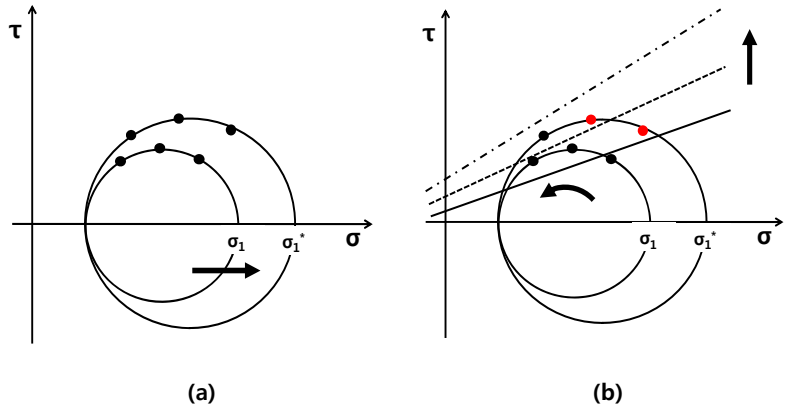

Figure 6.35 Anisotropic failure criterion and the increase of maximum principal stress (σ_1)

The size and shape of breakout zone in transversely isotropic rock depends on the failure criterion and the boundary stress.

The prediction of borehole breakout that do not consider the anisotropic behavior of rock can mislead to erroneous results therefore, it is necessary to consider the anisotropy in borehole stability analysis.

Chapter 7. Summary and conclusions

This study addresses the mechanical, seismic and thermal anisotropy and the mechanical stability of borehole in transversely isotropic rock. The experimental investigation of the anisotropy of elastic moduli, P-wave velocities, and thermal conductivities for Asan gneiss, Boryeong shale, and Yeoncheon schist in Korea were conducted. In order to analyze the borehole stability in transversely isotropic rock, both analytical and numerical methods were conducted. The data were based on laboratory experimental result of Boyeong shale. Several cases were analyzed in order to investigate the effect of elastic properties of transversely isotropic rock on the stress distribution across the domain as well as around the borehole wall. The anisotropic Mohr-Coulomb failure criterion considering strength anisotropy was applied to predict the borehole breakout in transversely isotropic rock.

1. Anisotropy ratios of elastic moduli, E/E', were determined to be 1.3, 2.1, and 3.4 for Asan gneiss, Boryeong shale, and Yeoncheon schist, respectively. The P-wave velocity anisotropy ratio ($V_P(90°)$ / $V_P(0°)$) was 1.2 for Asan gneiss, 1.5 for Boryeong shale, and 2.3 for Yeoncheon schist. The anisotropy ratios of thermal conductivity

parallel to and perpendicular to isotropic planes, (K(90°) / K(0°)), were 1.4 for Asan gneiss, 2.1 for Boryeong shale, and 2.5 for Yeoncheon schist. The variations of measured properties with anisotropy angle were similar to those of the elastic moduli. The extent of anisotropy observed in this study was significant and had the possibility of producing errors in engineering applications when anisotropy is not considered.

2. The mean prediction errors (MPEs), defined as the average relative differences between measured and predicted values of the seismic velocity, for Asan gneiss, Boryeong shale, and Yeoncheon schist were 3.5%, 4.6%, and 8.9%, respectively. The MPEs of thermal conductivity for Asan gneiss, Boryeong shale, and Yeoncheon schist were 6.1%, 9.3%, and 8.6%, respectively. These low MPEs imply that seismic properties can be modeled effectively by the approximated equations for the transversely isotropic model and thermal conductivities follows the transformation rule of a second-order tensor for the rocks included in this study. This MPE can be useful parameter as criterion to determine whether the selected rock follows the transversely isotropy model.

3. The effect of anisotropy ratio (E/E'), Poisson's ratio (ν/ν′) and shear modulus ratio (G/G′) for the stress distribution around the borehole were examined. The shear modulus ratio (G/G′) had big influence on the stress distribution and Poisson's ratio (ν/ν') did not have a great effect on it.

4. The borehole stresses computed from the numerical model and the analytical solution matched well for different borehole orientations in transversely isotropic rock as well as isotropic rock. The analytical solution for transversely isotropic rock is valid with no restrictions on the borehole orientation.

5. The anisotropic Mohr-Coulomb criterion associated with critical plane approach was applied to predict the borehole failure in transversely isotropic rock. The size and shape of breakout zone in transversely isotropic rock depends on the failure criterion and boundary condition.

Bibliography

Amadei, B., 1982. The influence of rock anisotropy on measurement of stresses in situ. Ph.D.Thesis, University of California Berkeley.

Amadei, B., 1996. Importance of anisotropy when estimating and measuring in situ stresses in rock. Int. J. Rock Mech. Sci. Geomech. Abst. 33**,** 293-325.

Amadei, B., Stephansson, O., 1997. Rock stress and its measurement, Springer.

Bachman, R.T., 1983. Elastic anisotropy in marine sedimentary rocks. J. Geophys. Res. 88**,** 539-545.

Barla, G., 1974. Rock anisotropy: Theory and laboratory testing. Springer-Verlag, New York, pp. 131-169.

Batugin, S., Nirenburg, R., 1972. Approximate relation between the elastic constants of anisotropic rocks and the anisotropy parameters. Journal of Mining Science. 8**,** 5-9.

Beardsmore, G.R., Cull, J.P., 2001. Crustal heat flow: A guide to measurement and modelling, Cambridge University Press.

Birch, A.F., Clark, H., 1940. The thermal conductivity of rocks and its dependence upon temperature and composition. Am. J. Sci. 238**,** 529.

Birch, F., 1960. The velocity of compressional waves in rocks to 10-kilobars .1. J. Geophys. Res. 65**,** 1083-1102.

Blackman, D.K., Wenk, H.R., Kendall, J.M., 2002. Seismic anisotropy of the upper mantle: 1. Factors that affect mineral texture and effective elastic properties. Geochem. Geophys. Geosyst. 3, 8601.

Brady, B.H.G., Brown, E.T., 2004. Rock mechanics: For underground mining, Springer.

Brigaud, F., Vasseur, G., 1989. Mineralogy, porosity and fluid control on thermal conductivity of sedimentary rocks. Geophysical Journal International. 98, 525-542.

Carslaw, H.S., Jaeger, J.C., 1959. Conduction of heat in solids, Clarendon Press, Oxford.

Chang, C., Lee, J.B., Kang, T.-S., 2010. Interaction between regional stress state and faults: Complementary analysis of borehole in situ stress and earthquake focal mechanism in southeastern korea. Tectonophysics. 485, 164-177.

Chen, C.S., Pan, E., Amadei, B., 1996. Evaluation of properties of anisotropic rocks using brazilian tests. In: 2nd North American Rock Mechanics Symposium.

Chen, C.S., Pan, E., Amadei, B., 1998. Determination of deformability and tensile strength of anisotropic rock using brazilian tests. Int. J. Rock Mech. Min. Sci. 35, 43-61.

Cho, J.-W., Kim, H., Jeon, S., Min, K.-B., 2012. Deformation and strength anisotropy of asan gneiss, boryeong shale, and yeoncheon schist. Int. J. Rock Mech. Min. Sci. 50, 158-169.

Crampin, S., 1989. Suggestions for a consistent terminology for seismic anisotropy1. Geophys. Prospect. 37, 753-770.

Daley, P.F., Hron, F., 1977. Reflection and transmission coefficients for transversely isotropic media. Bull. Seismol. Soc. Am. 67**,** 661.

Davis, M.G., Chapman, D.S., Van Wagoner, T.M., Armstrong, P.A., 2007. Thermal conductivity anisotropy of metasedimentary and igneous rocks. J. Geophys. Res. 112**,** B05216.

Donath, F.A., 1961. Experimental study of shear failure in anisotropic rocks. Geological Society of America Bulletin. 72**,** 985-989.

Gaede, O., Karpfinger, F., Jocker, J., Prioul, R., 2012. Comparison between analytical and 3d finite element solutions for borehole stresses in anisotropic elastic rock. Int. J. Rock Mech. Min. Sci. 51**,** 53-63.

Gupta, D., Zaman, M., 1999. Stability of boreholes in a geologic medium including the effects of anisotropy. Applied Mathematics and Mechanics. 20**,** 837-866.

Haimson, B.C., Chang, C., 2002. True triaxial strength of the ktb amphibolite under borehole wall conditions and its use to estimate the maximum horizontal in situ stress. Journal of geophysical research. 107**,** 2257.

Hoek, E., Brown, E.T., 1990. Underground excavations in rock, Taylor & Francis.

Horai, K., 1971. Thermal conductivity of rock-forming minerals. J. Geophys. Res. 76**,** 1278-1308.

ISRM (Ed.) 2007. The complete isrm suggested methods for rock characterization testing and monitoring.

Jaeger, J.C., Cook, N.G.W., Zimmerman, R.W., 2007. Fundamentals of rock mechanics, Wiley-Blackwell.

Johnson, L., Wenk, H.R., 1974. Anisotropy of physical properties in metamorphic rocks. Tectonophysics. 23, 79-98.

Johnston, J.E., Christensen, N.I., 1995. Seismic anisotropy of shales. J. Geophys. Res. 100, 5991-6003.

Kwasniewski, M.A., 1993. Mechanical behavior of anisotropic rocks. Comprehensive rock engineering. Vol. 1. 285-312.

Lee, S.-K., Lee, T.J., Sung, N.H., 2010. Characteristics of rock samples from seokmo island using an automated-continuous seismic velocity measuring system. J. Korean Soc. Geosys. Eng. 47, 756-770.

Lee, Y.-K., Choi, B.-H., 2011. Anisotropic version of mohr-coulomb failure criterion for transversely isotropic rock) Journal of Korean Society for Rock Mechanics. 21, 174-180.

Lee, Y.K., Pietruszczak, S., 2008. Application of critical plane approach to the prediction of strength anisotropy in transversely isotropic rock masses. Int. J. Rock Mech. Min. Sci. 45, 513-523.

Lekhnitskii, S.G., 1963. Theory of elasticity of an anisotropic elastic body.

Lo, T., Coyner, K.B., Toksoz, M.N., 1986. Experimental determination of elastic anisotropy of berea sandstone, chicopee shale, and chelmsford granite. Geophysics. 51, 164.

McLamore, R., Gray, K.E., 1967. The mechanical behavior of anisotropic sedimentary rocks. Journal of Engineering for Industry. 89, 62-73.

Ong, S.H., Roegiers, J.C., 1993. Influence of anisotropies in borehole stability. International Journal of Rock Mechanics and Mining Sciences & Geomechanics Abstracts. 30**,** 1069-1075.

Ong, S.H., 1994. Borehole stability. Ph.D.Thesis. The University of Oklahoma, Oklahoma.

Owens, W., Bamford, D., 1976. Magnetic, seismic, and other anisotropic properties of rock fabrics. Philosophical Transactions of the Royal Society of London. Series A, Mathematical and Physical Sciences. 283**,** 55.

Pietruszczak, S., Mroz, Z., 2001. On failure criteria for anisotropic cohesive-frictional materials. International journal for numerical and analytical methods in geomechanics. 25**,** 509-524.

Pietruszczak, S., Lydzba, D., Shao, J.F., 2002. Modelling of inherent anisotropy in sedimentary rocks. International Journal of Solids and Structures. 39**,** 637-648.

Pribnow, D.F.C., Sass, J.H., 1995. Determination of thermal conductivity for deep boreholes. J. Geophys. Res. 100**,** 9981-9994.

Ramamurthy, T., 1993. Strength and modulus responses of anisotropic rocks. Comprehensive rock engineering. Vol. 1. 313-329.

Song, I., Suh, M., Woo, Y.K., Hao, T., 2004. Determination of the elastic modulus set of foliated rocks from ultrasonic velocity measurements. Eng. Geol. 72**,** 293-308.

Ushaksaraei, R., Pietruszczak, S., 2002. Failure criterion for structural masonry based on critical plane approach. Journal of Engineering Mechanics. 128**,** 769-778.

Zoback, M.D., Moos, D., Mastin, L., Anderson, R.N., 1985. Well bore breakouts and in situ stress. J. Geophys. Res. 90**,** 5523-5530.

Zoback, M.D., 2007. Reservoir geomechanics, Cambridge Univ Pr.

초 록

암반은 층리면, 편리면 등의 영향으로 이방성을 띠는 경우가 많으며 이를 고려하는 것은 암반 공학의 여러 응용 분야에서 중요하다. 예를 들어 이산화탄소 지중 저장의 덮개암이자 셰일 가스 생산 등으로 중요한 셰일은 횡등방성을 띠는 대표적인 이방성 암석이다. EGS 지열 발전, 석유 시추, 이산화탄소 지중 저장 등을 위한 시추 시, 시추공 주변 응력의 크기와 방향이 변화되므로 이로 인한 시추공 안정성 해석이 필요하다. 일반적으로 시추공 안정성 해석을 위해서 등방성을 가정한 수치적 연구가 진행되어 왔으나, 이방성 암반 내 시추공 안정성 해석에 대한 연구는 소수에 불과하다. 암석의 이방성은 시추공 주변의 응력 집중뿐만 아니라 시추공벽 붕괴(borehole breakout)의 방향에도 영향을 주어, 이로 인한 간접적인 응력 측정에도 중요한 요소이다.

본 연구에서는 국내 횡등방성 암석의 탄성 계수, 탄성파 속도, 열전도도 이방성에 대한 실험을 수행하고, 이를 이용하여 횡등방성 암반 내 시추공의 역학적 안정성 해석을 위한 이론해 연구와 수치해석적 연구를 함께 수행하였다. 방향성 시추를 통해 등방평면에 15도 간격으로 채취한 암석시료에 대한 실험결과 탄성계수의

이방성비는 아산편마암, 보령셰일, 연천편암에 대하여 각각 1.3, 2.1, 3.4 였으며, P파 속도의 이방성비는 각각 1.2, 1.5, 2.3 그리고 열전도도 이방성비는 각각 1.4, 2.1, 2.5로 측정되었다. 등방평면과의 각도에 따라 결정된 물성값과 텐서변환에 의한 이론해와 비교한 결과 평균예측오차 (Mean Prediction Error)가 P파 속도의 경우 아산편마암, 보령셰일, 연천편마암에 대하여 각각 3.5 %, 4.6%, 8.9% 였으며, 열전도도의 경우 각각 6.1%, 9.3%, 8.6%로 나타나 횡등방성 모델이 본 실험에서 사용한 암석의 구성방정식으로 적합한 것으로 나타났다.

이방성 암반에 대한 시추공 안정성 해석을 위해 Amadei(1982)가 제안한 횡등방성 암반 내 시추공 주변의 응력 분포에 대한 기존 연구를 검토하고, 수치해석을 통한 탄성해 분석 결과를 수리해와 비교하였다. 입력 물성 자료로는 국내 이방성 암석의 역학적 물성을 조사한 실내 시험 결과를 이용하였다. 또한 강도 이방성을 고려한 이방성 Mohr-Coulomb 파괴 모델에서의 시추공벽 붕괴 범위를 추측해보고 이를 등방성 모델의 경우와 비교해 보았다. 암반의 이방성 정도에 따른 다양한 분석 결과를 통해, 시추공의 안정성 해석 수행 시, 암석의 이방적 특성을 고려하는 것이 필수적이라 판단된다.

주요어: 횡등방성, 탄성계수 이방성, 탄성파 속도 이방성, 열전도도 이방성, 시추공벽 붕괴, 시추공 안정성, 강도이방성

학 번: 2010-23337